

RECLAMATION

Managing Water in the West

**Desalination & Water Purification Research
and Development Program Report No. NMSU007**

**New Mexico Water Resources Research Institute
Technical Completion Report No. 386**

In-situ Synthesis of Antibacterial Ultrafiltration and Microfiltration Membranes with Controllable Pore Size



**U.S. Department of the Interior
Bureau of Reclamation
Technical Service Center
Denver, Colorado**

August 2020

REPORT DOCUMENTATION PAGE

*Form Approved
OMB No. 0704-0188*

The public reporting burden for this collection of information is estimated to average 1 hour per response, including the time for reviewing instructions, searching existing data sources, gathering and maintaining the data needed, and completing and reviewing the collection of information. Send comments regarding this burden estimate or any other aspect of this collection of information, including suggestions for reducing the burden, to Department of Defense, Washington Headquarters Services, Directorate for Information Operations and Reports (0704-0188), 1215 Jefferson Davis Highway, Suite 1204, Arlington, VA 22202-4302. Respondents should be aware that notwithstanding any other provision of law, no person shall be subject to any penalty for failing to comply with a collection of information if it does not display a currently valid OMB control number.

1. REPORT DATE (DD-MM-YYYY) 08/07/2020		2. REPORT TYPE Final		3. DATES COVERED (From - To) April 2016 to December 2019	
4. TITLE AND SUBTITLE In-situ Synthesis of Antibacterial Ultrafiltration and Microfiltration Membranes with Controllable Pore Size			5a. CONTRACT NUMBER Agreement No. R16AC00002		
			5b. GRANT NUMBER		
			5c. PROGRAM ELEMENT NUMBER		
6. AUTHOR(S) Sahar Qavi, Reza Foudazi			5d. PROJECT NUMBER		
			5e. TASK NUMBER		
			5f. WORK UNIT NUMBER		
7. PERFORMING ORGANIZATION NAME(S) AND ADDRESS(ES) Department of Chemical Engineering New Mexico State University Jett Hall, Room 268 Las Cruces, NM 88003-8001			8. PERFORMING ORGANIZATION REPORT NUMBER		
9. SPONSORING/MONITORING AGENCY NAME(S) AND ADDRESS(ES) Bureau of Reclamation U.S. Department of the Interior Denver Federal Center PO Box 25007, Denver, CO 80225-0007			10. SPONSOR/MONITOR'S ACRONYM(S) Reclamation		
			11. SPONSOR/MONITOR'S REPORT NUMBER(S) DWPR Report No. NMSU007		
12. DISTRIBUTION/AVAILABILITY STATEMENT Available from the National Technical Information Service, Operations Division, 5285 Port Royal Road, Springfield VA 22161					
13. SUPPLEMENTARY NOTES Online at https://www.usbr.gov/research/dwpr/DWPR_Reports.html					
14. ABSTRACT Self-assembly of amphiphilic block copolymers at an oil/water interface provides a flexible system for designing different types of mesomorphic structures (mesophases), such as lamellar, hexagonal, bicontinuous cubic, and micellar cubic. In this work, we use direct templating of preformed mesophases by polymerizing one of the phases (containing monomers) to obtain a nanoporous membrane. In such cases, we deal with polymerization in nanoconfinement, which has been studied in this work. Additionally, since processing of mesophases in the form of membranes involves deformation and flow, we investigated the viscoelastic behavior of mesophases and effect of flow on their nanostructure and orientation. Finally, selected mesophases are used to make UF membranes using this templating method. The fabricated UF membranes are found to have a molecular weight cutoff of 1500 g/mol, pore sizes in the range of 3-4 nm, and exhibit both excellent fouling resistance and high permeance of water, vastly outperforming a conventional UF membrane.					
15. SUBJECT TERMS Mesophases, Lyotropic Liquid Crystals, Self-Assembly, Nanoconfinement, Shear-Induced Alignment, Relaxation, Templating, Ultrafiltration, Membrane					
16. SECURITY CLASSIFICATION OF:			17. LIMITATION OF ABSTRACT	18. NUMBER OF PAGES	19a. NAME OF RESPONSIBLE PERSON Katherine (Katie) Guerra
a. EPORT U	b. ABSTRACT U	THIS PAGE U			19b. TELEPHONE NUMBER (Include area code) 303-445-2013

**Desalination and Water Purification Research
and Development Program Report No. NMSU007**

**New Mexico Water Resources Research Institute
Technical Completion Report No. 386**

In-situ Synthesis of Antibacterial Ultrafiltration and Microfiltration Membranes with Controllable Pore Size

**Prepared for the Bureau of Reclamation Under
Agreement No. R16AC00002**

by

**Sahar Qavi, Reza Foudazi
New Mexico State University
Department of Chemical Engineering**



**U.S Department of the Interior
Bureau of Reclamation
Technical Service Center
Denver, Colorado**

August 2020

Mission Statements

The U.S. Department of the Interior protects America's natural resources and heritage, honors our cultures and tribal communities, and supplies the energy to power our future.

The mission of the Bureau of Reclamation is to manage, develop, and protect water and related resources in an environmentally and economically sound manner in the interest of the American public.

Disclaimer

The views, analysis, recommendations, and conclusions in this report are those of the authors and do not represent official or unofficial policies or opinions of the United States Government, and the United States takes no position with regard to any findings, conclusions, or recommendations made. As such, mention of trade names or commercial products does not constitute their endorsement by the United States Government.

Acknowledgments

Work on this project was made possible by funding from a cooperative agreement between the U.S. Bureau of Reclamation (BOR) and New Mexico State University (#R16AC00002, Center for the Development and Use of Alternative Water Supplies). We thank Dr. Millicent Firestone at the Center for Integrated Nanotechnologies (CINT) at the Los Alamos National Laboratory for help by providing in small-angle X-ray scattering measurements.

Acronyms and Abbreviations

1D	One-dimensional
2D	Two-dimensional
AEAC	[2-(acryloyloxy) Ethyl]trimethyl Ammonium Chloride
APAC	(3-Acrylamidopropyl)trimethyl Ammonium Chloride
BA	Butyl Acrylate
BCC	Body Centered Cubic
BSA	Bovine Serum Albumin
CTAB	Cetrimonium bromide
DHR	Discovery Hybrid Rheometer
DI	Deionized
DMA	Diallylamine
DMF	N,N-Dimethylmethanamide
DPD	Dissipative particle dynamics
DR23	Direct Red 23
DSC	Differential Scanning Calorimetry
EGDMA	Ethylene Glycol Dimethacrylate
FCC	Face Centered Cubic
FWHM	Full Width at Half Maximum
LAOS	Large Amplitude Oscillatory Shear
LLC	Lyotropic Liquid Crystal
LVE	Linear viscoelastic
MBA	N,N'-methylenebis(acrylamide)
MF	Microfiltration

MWCO	Molecular Weight Cut Off
NF	Nanofiltration
NIPS	Non-solvent Induced Phase Separation
NMP	N-methyl-2-pyrrolidone
NMR	Nuclear Magnetic Resonance
ODT	Order-disorder transition Temperature
PEG	Poly(Ethylene Glycol)
PEGDA	Poly(Ethylene Glycol DiAcrylate)
PEO	Poly(ethylene oxide)
PEP-PEE	Poly(ethylenepropylene)–poly(ethylethylene)
PIV	Particle image velocimetry
PPO	Poly(propylene oxide)
PTC	Particle tracking velocimetry
RAFT	Reversible Addition Fragmentation chain Transfer
Rheo-SANS	Rheology-small angle neutron scattering
RO	Reverse Osmosis
SAXS	Small Angle X-ray Scattering
SNIPS	Self-assembly Non-solvent Induced Phase Separation
TGA	Thermal gravimetric analysis
TOC	Total Organic Carbon
TFE	Trifluoroethanol
UF	Ultrafiltration
UNICEF	United Nations Children's Fund
UV	Ultraviolet

Measurements

Å	angstrom
a.u.	arbitrary unit
°C	degree centigrade
g/L	gram per liter
g/mL	gram per milliliter
g/mol	gram per mole
hr	hour
Hz	Hertz
kJ/mol	kilo Joules per mole
L/hr	liter per hour
L/m ²	liter per square meter
L/m ² h	liter per square meter per hour
m	meter
min	minute
mm	millimeter
µm	micrometer
µs/cm	micro Siemens per centimeter
nm	nanometer
Pa	Pascal
Pa.s	Pascal second
Rad/s	radian per second
rpm	round per minute
s	second
wt%	weight percentage

Contents

Mission Statements	i
Disclaimer	i
Acknowledgments.....	i
Acronyms and Abbreviations	ii
Measurements	iv
List of Figures	x
List of Tables	xiii
Executive Summary	xiv
Chapter 1: Introduction.....	1
1.1 A background on water crises and remedies.....	1
1.1.1 Introduction	1
1.1.2 Non-solvent induced phase separation (NIPS).....	2
1.1.3 Alternative methods for making membranes.....	3
1.2 Block copolymers self-assembly	5
1.2.1 Introduction.....	5
1.2.2 Limitations of block copolymers self-assembly.....	6
1.2.3 Block copolymers self-assembly in solvents.....	6
1.2.4 Pluronic block copolymers	8
1.3 Rheological properties of mesophases	9
1.3.1 Mesophases flow behavior	9
1.3.2 Oscillation behavior of mesophases	9
1.3.3 Shear-induced orientation in mesophases.....	10
1.4 Overview of current work	12
Chapter 2: Materials and Methods.....	13

2.1. Materials.....	13
2.2 Mesophase preparation.....	13
2.3 SAXS analysis.....	14
2.3.1 Methodology.....	14
2.3.2 Determining different mesophase structures using SAXS	14
Chapter 3: Rheological Characteristics of Mesophases of Block Copolymer Solutions.....	15
3.1. Introduction	15
3.2 Experimental Methodologies	16
3.2.1 Formulation design.....	16
3.2.2 Small angle X-ray scattering (SAXS) measurements.....	17
3.2.3 Rheological measurements.....	17
3.3 Results and discussion.....	18
3.3.1 SAXS analyses	18
3.3.2 Rheological characteristics	19
Chapter 4: Studying the Polymerization in Soft Nanoconfinements of Lamellar and Reverse Hexagonal Mesophases Using Chemorheology	20
4.1. Introduction	20
4.2 Experimental Methodologies	21
4.3 Results and discussion.....	21
4.3.1 SAXS analyses	21
4.3.2. Rheological measurements.....	21
4.3.3 DSC measurements.....	28
4.4 Conclusion.....	28
Chapter 5: Ultrafiltration Membranes from Polymerization of Self-Assembled Pluronic Block Copolymer Mesophases	29
5.1 Introduction	29
5.2 Experimental Procedures.....	30

5.2.1 Preparation of lamellar and hexagonal mesophases	30
5.2.2 Cross-polarized light microscopy	30
5.2.3 SAXS measurements	31
5.2.4. Preparation of the membranes	31
5.2.5 Membrane performance measurements	31
5.3 Results and discussion.....	32
5.3.1 Mesophase characterization.....	32
5.3.2 Membrane performance.....	37
5.4 Using functional monomers for making antibacterial membranes	41
5.4.1 Materials and formulation design	42
5.4.2 SAXS analysis	43
5.4.3 Membrane performance.....	44
5.4.4 Antibacterial properties of the membranes.....	44
5.5 Conclusion.....	46
Chapter 6: Conclusions and Future Work	48
6.1 Summary	48
6.2 Future work	49
References.....	50
Appendix A: Properties of Pluronic Block Copolymers.....	67
Appendix B: General Concepts in Rheology.....	70
Appendix C: Physical Properties of Pluronic Block Used in This Study.....	75
Appendix D: Calculating lattice parameters from SAXS data	76
Appendix E: Rheological Measurements Performed on Mesophases for Chapter 3 Data	80
E.1 Rheological measurements	80
E.2 Rheo-small angle neutron scattering (Rheo-SANS) measurements	80
Appendix F: SAXS Graphs for Mesophase Samples in Chapter 3.....	81

Appendix G: Rheological Characteristics of Mesophases.....	82
G.1 Wall-slip.....	82
G.2 Flow behavior.....	83
G.3 Amplitude sweep.....	84
G.4 Frequency sweep.....	86
G.5 Stress relaxation.....	87
G.6 Shear induced alignment and relaxation behavior.....	88
Appendix H: Experimental Methodology and Results for Chapter 4 Data.....	92
H.1 Experimental Procedures.....	92
H.1.1 Materials.....	92
H.1.2 Formulation design.....	92
H.1.3 Rheological measurements.....	92
H.1.4 DSC measurements.....	93
H.1.5 Monomer conversion.....	93
H.2 Results.....	94
H.2.1 SAXS.....	94
H.2.2 Rheological measurements.....	96
H.2.3 DSC measurements.....	98
Appendix I: Experimental Methodology and Results for Chapter 5 Data.....	101
I.1 Experimental Methodology.....	101
I.1.1 Membrane fabrication.....	101
I.2 Results.....	102
I.2.1 SAXS data.....	102
I.2.2 Membrane performance.....	103
I.2.3 Antibacterial membranes SAXS results.....	104
I.2.4 Antibacterial membrane performance measurements.....	106

Appendix J: Future Work.....	107
J.1 Studying the flow-induced behavior of mesophases using rheo-SANS.....	107
J.2 Studying the shear banding behavior of mesophases using velocimetry technique.....	107
J.3 RAFT polymerization in nanoconfined mesophases.....	107

List of Figures

Figure 1-1. Different types of membranes used for water treatment. Specific pore size and the pressure range needed for each membrane type are shown.	2
Figure 1-2. Schematic illustration of NIPS membranes drawback, including low surface porosity, external and internal fouling.	3
Figure 1-3. Typical phase diagram of a diblock copolymer. f : Volume fraction of one block (i.e. A). χ : Flory-Huggins interaction parameter. N : degree of polymerization. L: lamellae, H: hexagonally packed cylinders, Q230: double-gyroid phase, Q229: body-centered spheres, CPS: closed-packed spheres. DIS: disordered, retrieved from [40]. Top row schematically illustrates different morphologies that may exist in a phase diagram of a block copolymer.	6
Figure 1-4. Phase diagram for Brij 97–water systems. L_1 , L_2 , H_1 , V_1 , L_{\square} and L_c denote micellar phase, inverse micellar phase, hexagonal phase, cubic phase, lamellar phase and surfactant lamellar crystals, respectively, retrieved from [41].	7
Figure 1-5. Phase diagram of Pluronic P84 block copolymer in the presence of water and p-xylene as selective solvents, retrieved from [43]. Nine different morphologies including normal micellar (L_1), normal micellar cubic (I_1), normal hexagonal (H_1), normal bicontinuous gyroid (V_1), lamellar (L_{α}), reverse micellar (L_2), reverse micellar cubic (I_2), reverse hexagonal (H_2), and reverse bicontinuous gyroid (V_2) are present. The concentrations are expressed in wt%. Schematics of the different modes of self-organization of the amphiphilic block copolymers in the presence of solvents (“water” and “oil”) are shown adjacent to the respective phases in the phase diagram.	8
Figure 1-6. Schematic illustration of the dominating layer orientation in a lamellar structure. Shear rate increases from left to right, retrieved from [99].	11
Figure 2-1. Typical SAXS patterns for different mesophase structures. (a) lamellar mesophases show 1:2:3:4... relative peak positions, (b) hexagonal mesophases show 1: $\sqrt{3}$:2: $\sqrt{7}$: relative peak positions, (c) BCC mesophases show 1: $\sqrt{2}$:2: $\sqrt{6}$... relative peak positions.	14
Figure 3-1. Cross section of a typical polycrystalline hexagonal mesophase shows three types of defect, vacancy, dislocation, and grain boundaries.	16
Figure 3-2. Typical SAXS graphs for lamellar and hexagonal mesophases: (a) P84_60/15/25_H ₂ , (b) P123_50/45/5_H ₁ , (c) P123_60/35/5_L, and (d) P84_70/25/5_L.	18

Figure 4-1. Schematic illustration of: (a) the effect of confinement on the probability of termination reactions, (b) the increase in domain size upon polymerization due to the tendency of polymer chains to form random coils, and (c) the expected dependence of change in domain size upon polymerization to the template modulus (see Equation (4-1)).	20
Figure 4-2. Variation of dynamic moduli with time at three different temperatures (60, 65, and 70 °C) for (a) P84-L α , (b) L121-L α , (c) P84-H $_2$, and (d) L64-H $_2$ samples.	22
Figure 4-3. Evolution of complex viscosity at different curing temperatures for (a) P84-L α , (b) L121-L α , (c) P84-H $_2$, and (d) L64-H $_2$ samples. The dashed lines show the fitted slope in the propagation step.	24
Figure 4-4. Schematic illustration of the parameters obtained from SAXS and confinement size in (a) lamellar and (b) reverse hexagonal mesophases.	25
Figure 4-5. (a) Effect of curing temperature on conversion of each mesophase system. (b) Effect of conversion on the final mechanical properties of each sample.	27
Figure 4-6. Temperature sweep of dynamic moduli of polymerized mesophases: (a) P84-L α (60/15/25), (b) L121-L α (57/18/25), (c) P84-H $_2$ (40/35/25), and (d) L64-H $_2$ (55/20/25) samples, cured at different temperatures (shown in the legend).	27
Figure 5-1. Schematic representation of templating method for making mesoporous polymers using (a) lamellar and (b) hexagonal mesophases. Oil phase consists of monomer, crosslinker, and initiators.	30
Figure 5-2. Cross-polarized light micrographs obtained for mesophases before and after polymerization with compositions I, II, III, and IV, as listed in Table 5-1. Scale bar: 50 μ m.	33
Figure 5-3. 1D and 2D scattering profiles for mesophases before (left column, BP) and after (right column, AP) polymerization for compositions I, II, III, and IV, listed in Table 5-1.	34
Figure 5-4. Schematic representation of grain boundaries that can lead to open or dead-end pores.	39
Figure 5-5. Filtration of (a) 1 mg/mL BSA and (b) 1 mg/mL PEG300 solutions through lamellar (I), hexagonal (III), and commercial membranes. Error bars indicate the standard deviation of three measurements.	40
Figure 5-6. MWCO curve for as-synthesized membranes using TOC method, (a) lamellar membrane (sample I), (b) hexagonal membrane (sample III).	41

Figure 5-7. Schematic illustration of antibacterial membranes made through self-assembly using a functional monomer..... 42

Figure 5-8. Typical digital images of the Petrifilms after 48 hr of incubation. (a) 1:1 dilution and in contact with membrane, (b) 1:10 dilution and in contact with membrane, (c) 1:1 dilution of control sample, (d) 1:10 dilution of control sample. 46

List of Tables

Table 3-1. Composition and lattice size parameters for the samples used in this study.....	17
Table 4-1. Model parameters for the initiation and propagation steps of polymerization in the bulk, lamellar and reverse hexagonal samples.....	23
Table 4-2. Values of the necessary parameters for calculating Rh, max in the reverse hexagonal samples.	26
Table 5-1. Formulation design of the synthesized membranes.....	31
Table 5-2. Calculated parameters for lamellar and hexagonal mesophases before polymerization (BP) and after polymerization (AP).....	35
Table 5-3. Flow rate, normalized permeability, BSA rejection, and tortuosity of as-synthesized lamellar and hexagonal membranes compared to a commercial one.	37
Table 5-4. Composition of the samples used for the synthesis of antibacterial membranes.	43
Table 5-5. Calculated parameters for lamellar and hexagonal mesophases before polymerization (BP) and after polymerization (AP).....	44
Table 5-6. Flow rate, normalized permeability, and BSA rejection of as-synthesized lamellar membranes compared to commercial one.....	44
Table 5-7. Number of the colonies in each sample after 48 h of incubation.	45

Executive Summary

The aim of this study was to produce antibacterial ultrafiltration (UF) and microfiltration (MF) membranes for water and wastewater treatment without the need for costly, post-synthesis functionalization or hazardous solvents. In order to accomplish this aim, mesophases were made using Pluronic block copolymers with different block ratios in the presence of anti-bacterial monomers with trimethylammonium chloride functional groups. Through the polymerization of monomers and subsequent removal of the block copolymers, mesoporous polymers were produced that can serve as UF or MF membranes, depending on the pore size, which can be manipulated through the block ratio of the block copolymer. We confirmed that the ratio of poly(ethylene oxide) (PEO) to poly(propylene oxide) (PPO) blocks (PEO/PPO) in Pluronic block copolymers can affect the pore size of final membranes.

Antibacterial MF or UF membranes can be used in the pretreatment stage to not only remove suspended particles and macromolecules, but also to disinfect the water. Self-assembly of Pluronic block copolymers with different block ratios in the presence of [2-(acryloyloxy) ethyl] trimethylammonium chloride (AEAC) or (3-acrylamidopropyl) trimethylammonium chloride (APAC) and N,N'-methylenebis(acrylamide) (MBA) yield different mesostructures with different channel sizes, which can then be cast as thin films on a support and polymerized to produce antibacterial membranes. Final membranes have been studied in terms of antibacterial performance, permeability, and biofouling.

Since mesophases are viscoelastic materials, understanding their flow behavior at different flow fields is essential for optimizing their processability. Therefore, a comprehensive rheological study has been done on mesophases of block copolymers with different length scales.

In the process of membrane fabrication, polymerization reaction occurs in nanoconfined spaces of lamellar and hexagonal mesophases. Chemorheology and dynamic scanning calorimetry were used to study the kinetics of polymerization in nanoconfined structures of lamellar and reverse hexagonal mesophases.

Chapter 1: Introduction

1.1 A background on water crises and remedies

1.1.1 Introduction

Water resources become scarcer as the world population continues to grow. Water scarcity today affects one-third of the world's population, and according to the World Health Organization and UNICEF Joint Monitoring Program, "every two minutes a child dies from a water-related disease, and 160 million children suffer from stunting and chronic malnutrition linked to water and sanitation" [1]. Increases in water usage will also raise the amount of wastewater that should be treated sufficiently to meet environmental regulations.

Thermal distillation is one of the main methods employed for water desalination [2]. In this process, water (usually seawater) is vaporized using heat, and water vapor is condensed to provide purified water. Although thermal desalination produces purified water at a high rate, it is highly energy intensive due to the heating requirement to vaporize water [2, 3].

Membrane technology is an effective, efficient, and green method to produce safe drinking water. Such technologies are also essential for wastewater treatment, so as to eliminate the contamination of our limited water resources. Membranes are a cost-effective method; they are 80% less expensive than distillation [4] as shown by industrial separations, where separation accounts for more than 45% of the process energy consumed by the chemical and oil industries [5].

Water treatment processes employ several types of membranes, including microfiltration (MF), ultrafiltration (UF), nanofiltration (NF), and reverse osmosis (RO) [6]. All of these processes are pressure-driven and their main difference is the pore size, as depicted in Figure 1-1.

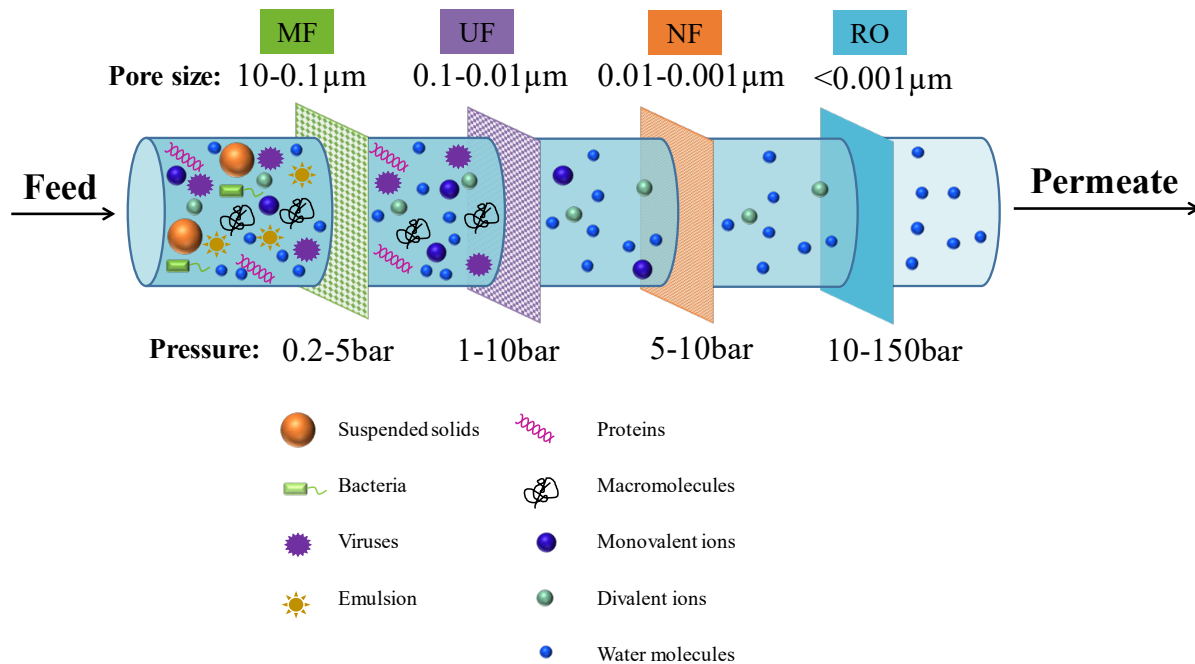


Figure 1-1. Different types of membranes used for water treatment. Specific pore size and the pressure range needed for each membrane type are shown.

The membrane market value exceeds \$32 billion [7] and continuously advances in terms of membrane fabrication and processing technology. The market share for ultrafiltration and nanofiltration is almost 50% of the total membrane market [8], where they are mostly used in water and wastewater treatment to remove proteins, macromolecules, viruses, and monovalent ions from the feed water. Additionally, UF and NF membranes have applications in food and dairy industries, hemodialysis, textile industries, pharmaceutical industries, and membrane bioreactors. Conventional UF/NF membranes are produced through the non-solvent induced phase separation (NIPS) method [9, 10].

1.1.2 Non-solvent induced phase separation (NIPS)

The NIPS method includes three main components (polymer, solvent, and non-solvent), and it involves casting the polymer solution on a surface and then, immersing the cast polymer film in a non-solvent (usually water) to induce precipitation and coagulation. This results in a solid polymer film with a porous structure determined by the polymer concentration, film thickness, and the interaction of the polymer and solvent(s) of interest. While this approach is simple and

scalable, membranes produced by NIPS have low-surface porosity, low-pore interconnectivity (Figure 1-2), and an anisotropic pore structure [11–13]. This results in lower fluxes, poorer separations, and increased fouling relative to a membrane with an ideal, highly interconnected pore structure.

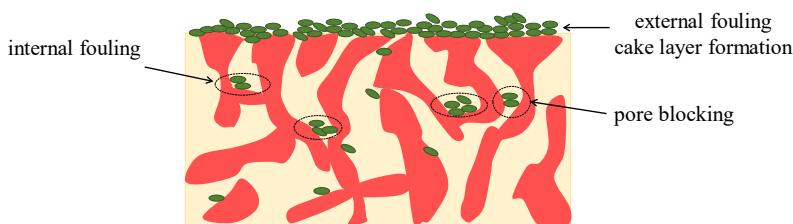


Figure 1-2. Schematic illustration of NIPS membranes drawback, including low surface porosity, external and internal fouling.

Fouling occurs when suspended solids and particles accumulate on the external membrane surface and generate a cake layer, and/or on/within the pores of the membrane, see Figure 1-2. Fouling results in a higher cleaning frequency, lower flux over time, higher energy usage, and shorter lifespan of the membrane. It has been shown that membranes with highly interconnected asymmetric pores allow fluid flow around and under pore blockage on the membrane surface, and reduces the flux decline significantly [14]. Additionally, hydrophilic pores result in less fouling as they provide a repulsion force for biofoulants, such as proteins [11].

1.1.3 Alternative methods for making membranes

One of the main challenges in using the NIPS method is the high toxicity of the solvent used during membrane fabrication. For example, N,N-dimethylformamide (DMF) and N-methyl-2-pyrrolidone (NMP) are the common solvents used in large quantities, approximately 70% by volume, in the NIPS process [15], and have encountered increasing regulations due to their potential health issues [16]. As a result of environmental concerns, considerable research efforts have been devoted to replacing toxic hazardous solvents with environmentally friendly alternatives [17, 18]. Additionally, the drawbacks of NIPS membranes motivate researchers to look for post-treatment modification or alternative methods to improve the properties of the membranes.

1.1.3.1 Surface functionalization of membranes

Surface characteristics such as hydrophilicity, roughness, and charge have been reported to influence fouling in membranes. Increased membrane hydrophilicity is reported to help increase membrane fouling resistance [19, 20]. Additionally, smooth membranes are less susceptible to

fouling than rough membranes [21]. For charged foulants, functionalization of the membrane surface with a charge opposite to that of the foulant enhances electrostatic repulsion and fouling resistance [22, 23].

Different methods are usually used to modify the surface properties of the membranes including adsorption [24], coating [25], surface chemical reactions [26, 27], surface grafting [28], and incorporation of nanoparticles [29]. Each surface modification method has its own advantages and disadvantages. For example, although adsorption and coatings can be easily employed, the surface layer may be removed after long usage of the membrane. Surface chemical reactions and surface grafting are sometimes carried out under very hazardous conditions. Grafted surfaces are stable, but the chemicals used for grafting are sometimes environmentally unfriendly. Additionally, grafting by gamma ray and UV irradiation, or in the plasma chamber, is not easy to apply on a large industrial scale [22]. Nanoparticle synthesis requires complex and controlled reactions, which are usually hard to scale up.

1.1.3.2 Self-assembly and non-solvent induced phase separation (SNIPS) procedure

In the SNIPS method, a combination of self-assembly and NIPS is employed to make membranes with a relatively narrow pore size distribution [30, 31]. First, functional polymers or block copolymers are dissolved in an organic solvent. Then the solution is held at a constant condition (temperature, pressure) so the polymers self-assemble and make ordered structures. Finally, the solution is cast on a support and immersed in a non-solvent bath for pore phase separation and pore formation. Membranes made through SNIPS have shown a better selectivity compared to NIPS membranes.

Bengani and others [30] employed self-assembly of a random block copolymer with zwitterionic functional groups to make UF/NF membranes with a narrow size distribution and high selectivity. They first synthesized a random block copolymer using sulfobetaine methacrylate and 2,2,2-trifluoroethyl methacrylate monomers. Next, the block copolymer was dissolved in trifluoroethanol (TFE), where self-assembly of zwitterionic copolymers occurred leading to the formation of effective “nanochannels” permeable to water and solutes [30]. Although the SNIPS method seems promising in tackling some of the NIPS process drawbacks, it is not eco-friendly and the organic solvent used (TFE) is more hazardous than DMF and NMP.

1.1.3.3 Polymerizable lyotropic liquid crystals as UF/NF membranes

Recently, polymerizable/crosslinkable lyotropic liquid crystal (LLC) mesogens have been used to make UF/NF membranes using a self-assembly technique [32–35]. In this method, a polymerizable LLC mesogen is synthesized first. Then, self-assembly of the LLC mesogen in a selective solvent is used to form the desired structure. Processing the self-assembled materials into a flat sheet with subsequent polymerization then results in membranes with a narrow pore

size distribution ($\sim 1\text{nm}$) [32, 33, 36]. This method provides a robust membrane with high selectivity. However, it is difficult and expensive to manufacture at large scale due to the complex chemistry involved in making polymerizable LLC mesogens. Additionally, membrane functionality cannot be tuned using this method and post-modification techniques are required.

In this work, the self-assembled mesostructures of a commercially available Pluronic block copolymer (Pluronic L64) in water and an oil phase consisting of monomers are employed as templates for the preparation of UF membranes without the need for organic solvents. Hexagonal and lamellar mesophases are prepared by changing the concentration of Pluronic L64 and the water/monomer ratio. Polymerization of the monomer phase via a thermal/photo-initiation system followed by extraction of the aqueous phase generally retains the template structure, generating pores in the resultant membrane.

1.2 Block copolymers self-assembly

1.2.1 Introduction

A polymer molecule has many hundreds of monomers and its molecular weight can reach beyond ten thousand grams per mole, g/mol [37]. Polymers are used to solve some of the major environmental issues such as water scarcity. Most of the filtration membranes used for water and wastewater treatment are made of synthetic polymers such as polysulfone, poly(ether sulfone), and poly(vinylidene fluoride). Homopolymers are polymers that consist of only one type of monomer. If more than one type monomer is in the structure of a polymer, it is called a copolymer.

Block copolymers contain at least two distinct monomers, A and B, and have various architectures, such as linear diblock (AB), triblock (ABA), multiblock $(AB)_n$, and star diblocks $(AB)_nX$. Phase behavior of block copolymers is determined by three parameters: (1) the overall degree of polymerization N that is proportional to molecular weight, (2) the magnitude of the Flory-Huggins interaction parameter χ , which is inversely proportional to temperature, and (3) the composition of the copolymer f , which is expressed in terms of volume fraction of each block [38, 39]. Amphiphilic block copolymers self-assemble in bulk and/or in solution and form various structures with different properties. Self-assembly is a thermodynamically driven phenomenon, where each block of copolymer minimizes energetically unfavorable interactions with its poor solvent. Figure 1-3 schematically shows the self-assembly of block copolymers and the phase diagram of a diblock copolymer. As mentioned above, N , χ , and f are the three parameters that determine the type of structure in a block copolymer.

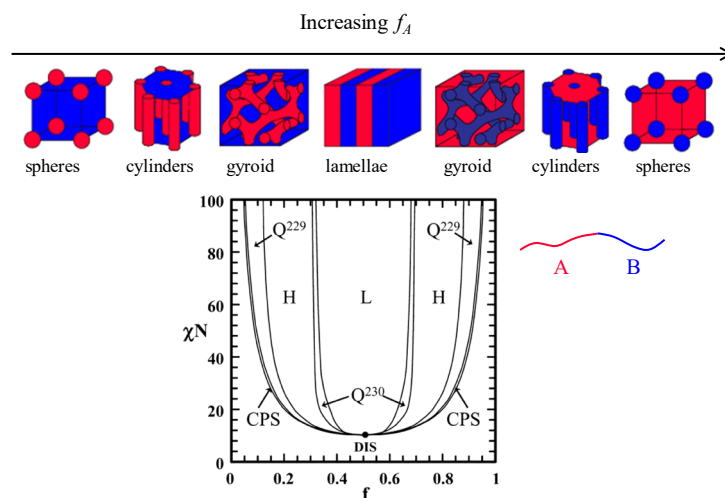


Figure 1-3. Typical phase diagram of a diblock copolymer. f : Volume fraction of one block (i.e., A). χ : Flory-Huggins interaction parameter. N : degree of polymerization. L: lamellae, H: hexagonally packed cylinders, Q230: double-gyroid phase, Q229: body-centered spheres, CPS: closed-packed spheres. DIS: disordered, retrieved from [40]. Top row schematically illustrates different morphologies that may exist in a phase diagram of a block copolymer.

1.2.2 Limitations of block copolymers self-assembly

Although solvent-free block copolymers provide some extent of flexibility in design of different morphologies and properties, they introduce some limitations in design. For example, based on Figure 1-3, if we want to have different morphologies, we need to either change the temperature (or χ) or change the block ratios. For changing the block ratios (increasing or decreasing f), we have to synthesize a new block copolymer; that is not a trivial task and involves using complex chemistries. Two remedies can be used to overcome this problem: (1) self-assembly of block copolymers in a single solvent, and (2) self-assembly of block copolymers in two selective solvents.

1.2.3 Block copolymers self-assembly in solvents

Figure 1-4 shows the phase diagram of the poly(oxyethylene (10) oleyl ether) (Brij97) block copolymer in water. Different types of morphologies are obtained depending on the concentration of the block copolymer in water and/or the temperature. Although this approach gives us more flexibility in design, we still need to use different concentrations or temperatures to achieve different morphologies.

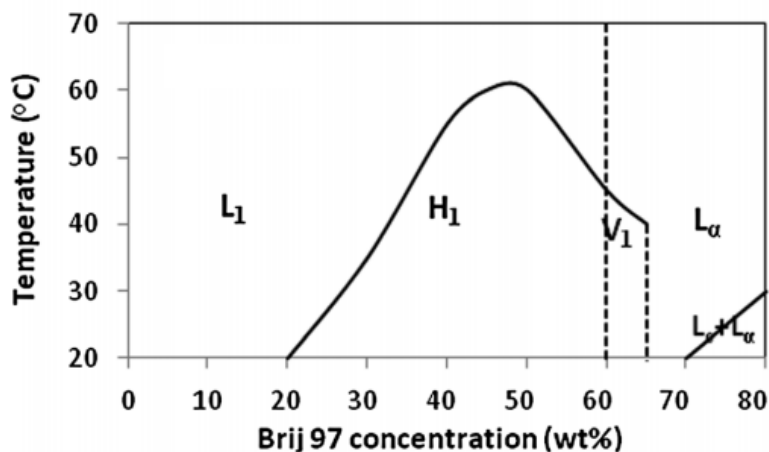


Figure 1-4. Phase diagram for Brij 97–water systems. L₁, L₂, H₁, V₁, L_α and L_c denote micellar phase, inverse micellar phase, hexagonal phase, cubic phase, lamellar phase and surfactant lamellar crystals, respectively, retrieved from [41].

Adding two solvents offers even more flexibility to have a wide range of structures and domain sizes with the same block copolymer and at a constant temperature [42, 43]. Self-assembly of block copolymers in the presence of solvents forms ordered mesophase structures, also known as LLCs [42]. In ternary systems, where there are two selective solvents, a rich phase diagram can be obtained at a constant temperature, as shown in Figure 1-5 [42, 44, 45]. Mesophases are used in templating methods for making mesoporous materials [46–51] with different applications in the separation and adsorption processes [36, 42, 52–55], and also in the biomedical and pharmaceutical industries [56–59].

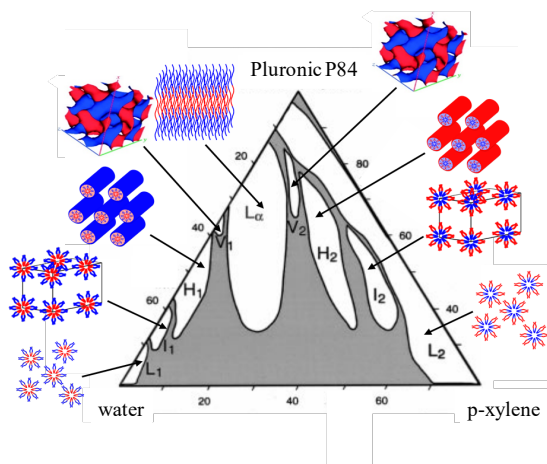


Figure 1-5. Phase diagram of Pluronic P84 block copolymer in the presence of water and p-xylene as selective solvents, retrieved from [43]. Nine different morphologies including normal micellar (L_1), normal micellar cubic (I_1), normal hexagonal (H_1), normal bicontinuous gyroid (V_1), lamellar (L_α), reverse micellar (L_2), reverse micellar cubic (I_2), reverse hexagonal (H_2), and reverse bicontinuous gyroid (V_2) are present. The concentrations are expressed in wt%. Schematics of the different modes of self-organization of the amphiphilic block copolymers in the presence of solvents (“water” and “oil”) are shown adjacent to the respective phases in the phase diagram.

1.2.4 Pluronic block copolymers

Pluronic block copolymers are triblock copolymers of poly(ethylene oxide) or PEO, and poly(propylene oxide) or PPO, and are often denoted as PEO-PPO-PEO or $(EO)_X-(PO)_Y-(EO)_X$. The PEO block is hydrophilic and the PPO block is hydrophobic; therefore Pluronics are amphiphilic and act as nonionic polymeric surface active agents [60]. More details on Pluronic block copolymers are given in Appendix A.

Progression of the structure in the block copolymer/water/oil phase diagram can be discussed at two levels: (1) varying water/oil ratio at constant total copolymer content, and (2) changing total copolymer content at constant copolymer/oil [copolymer/water] ratio [42]. The type of structure obtained does not only depend on the ternary copolymer-water-oil composition, but also depends on the PEO/PPO ratio and the molecular weight of block copolymer. The ability of the blocks to swell to different extents (based on the amount of solvent available) modulates the interfacial “curvature,” and thus, the resulting structure. An increase in the copolymer molecular weight for a given block composition increases the block segregation (for the same solvent conditions) and results in an increase of the temperature and composition stability range of the different structures. Higher polymer molecular weight may also lead to the formation of additional structures because of the increase in the range of inter-assembly interactions [45].

1.3 Rheological properties of mesophases

General concepts in rheology are summarized in Appendix B.

1.3.1 Mesophases flow behavior

Rheological properties of self-assembled block copolymer melts and [39, 61, 70, 62–69] block copolymers in a single solvent have been widely studied [62, 71–77]. Solutions containing unimers or individual micelles of Pluronics show Newtonian behavior. As surfactant concentration increases, the resultant fluid becomes more complex. If micelles form a crystalline structure, the system gels with non-Newtonian characteristics [78]. At intermediate concentrations of Pluronics, wormlike micelles will form because of the aggregation and entanglement of the chains. These structures are like polymer solutions and their rheological properties have been studied widely.

Montalvo and others [79] studied the rheological properties of lamellar and hexagonal liquid crystals of a small molecule surfactant, cetrimonium bromide (CTAB) in the presence of benzyl alcohol and water. They have observed shear thinning behavior for hexagonal mesophases with a zero-shear rate, while for lamellar mesophases, a yield stress has been observed at low values of shear rate. The observed values of yield stress for lamellar samples are in the range of 1.5 Pa < σ_y < 15 Pa [79]. Rodriguez-Abreu and others [80] studied the rheological properties of normal (H_1) and reverse (H_2) hexagonal mesophases where a yield stress is observed in both phases.

1.3.2 Oscillation behavior of mesophases

Small amplitude oscillatory shear tests have been used to study the viscoelasticity of mesophases. In the amplitude sweep experiments, mesophases show type III non-Newtonian behavior, like many other colloidal systems such as highly concentrated emulsions [81] and polymer solutions [82]. A weak strain overshoot is observed in type III non-Newtonian behavior and both storage modulus (G') and loss modulus (G'') decrease at relatively high strains, where non-linear viscoelastic behavior is observed [82].

The value of storage moduli in different mesophases are different and usually are associated with the type of structure. For example, it has been observed that the values of storage modulus for both H_1 and H_2 are in the same order of magnitude, but slightly higher for normal phases [80]. Additionally, the value of storage modulus for lamellar mesophases is at least one order of magnitude lower, when compared to hexagonal mesophases [79].

In frequency sweep experiments, the linear viscoelastic response of mesophases is consistent with that of a viscoelastic liquid and can be described by a generalized Maxwell model. Mesophases show a viscoelastic behavior with a solid-like behavior in a relatively broad range of frequencies, where G' is higher than G'' . Both microscopic and mesoscopic domains contribute to the viscoelasticity of mesophases. The bicontinuous cubic (gyroid) structures of a phytantrio in water shows a viscoelastic behavior with a crossover between G' and G'' , while the reverse hexagonal structure of the same samples show no crossover point and the material behaves like a solid in the whole range of frequencies (0.01-100 Hz) [83]. Mesophases response in the frequency sweep experiment is usually in the rubbery plateau region, due to a high level of ordering that makes the material solid-like.

Although several experimental tests can be employed to study the rheological properties and viscoelastic behavior of mesophases, having a model to estimate their elastic modulus is very helpful in designing new materials for different types of applications. Studies show that the crystalline structure of mesophases plays an important role in their viscoelastic behavior. For example, the elastic modulus of lamellar mesophases is at least one order of magnitude lower when compared to hexagonal systems [79, 84–86].

The dissipative particle dynamics (DPD) simulation method [87] is used to model the viscoelastic properties of a gel system based on self-assembly of an amphiphilic ABA triblock copolymer in midblock-selective solvent. It has been found that the elastic response of a low molecular weight ABA triblock copolymer gel is comparable with the Rouse modulus [87]. In another study, the stress fluctuation simulation technique has been used to model the elastic constants of a face-centered cubic (FCC) crystalline polymer at different temperatures [88, 89].

Although simulation techniques are helpful in estimating the mechanical properties of self-assembled materials, no analytical model, to the best of our knowledge, exists to estimate the average elastic modulus of a self-assembled mesophase based on its structure.

1.3.3 Shear-induced orientation in mesophases

Orientation and ordering of soft materials, such as block copolymers [90], colloidal suspensions [91], thermotropic [92] and lyotropic liquid crystals [93], can be affected by flow and deformation as a result of shear. For example, in symmetric diblock copolymer melts, steady state shear can induce disorder-to-order transitions, when sheared above their order-disorder transition (ODT) temperature [94]. In asymmetric diblock copolymers of poly(ethylenepropylene)–poly(ethylethylene) (PEP-PEE), a cubic phase transition to the hexagonal phase has been observed as a result of shear [95]. Shear-induced orientation is a

response of the material to minimizing flow stress by orienting microstructures to reduce the interfaces between self-assembled molecules [96].

Different methods such as scattering techniques [97], nuclear magnetic resonance (NMR) [98], and flow birefringence [99] are used to study the shear-induced orientations in LLCs. In a lamellar system of sodium dodecyl sulphate/decanol/D₂O, steady flow leads to the reorientation of lamellae from perpendicular, with the layer normal in vorticity direction, to parallel, with the layer normal in velocity gradient direction (see Figure 1-6). Reduction in the viscosity of the system as a result of such reorientation is reported [99].

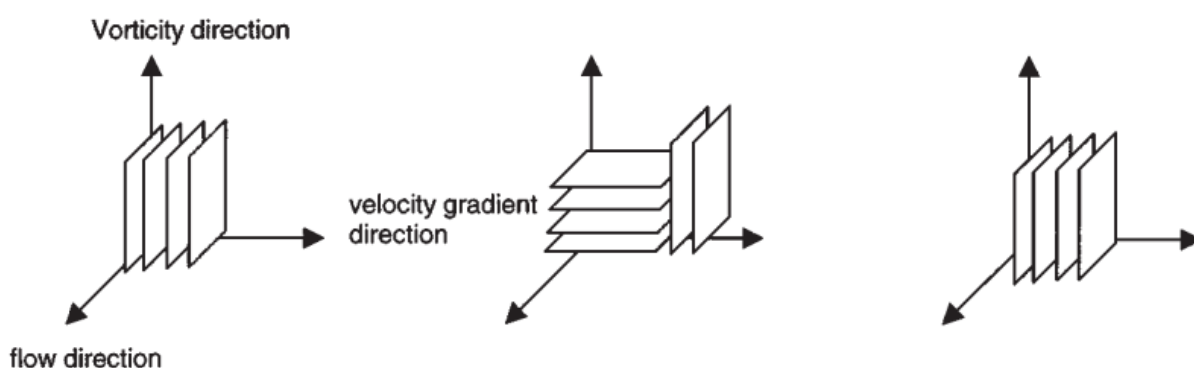


Figure 1-6. Schematic illustration of the dominating layer orientation in a lamellar structure. Shear rate increases from left to right, retrieved from [99].

Oscillatory shear can also be used to align the mesophase structures. For instance, in a block copolymer solution of Pluronic P123, applying oscillatory shear leads to the formation of a single crystal, verified via the rheology-small angle neutron scattering (rheo-SANS) technique [97].

Mesophases are not a single liquid crystal structure, but consist of different types of defects, such as vacancies, dislocations, and grain boundaries that will be discussed in the following chapters. Studies show that appropriate shear flow can remove the defects present in the ordered structures of block copolymers; therefore, domains orient themselves in the direction of flow and the storage modulus of the system decreases [76, 100, 101]. Defects have a very long relaxation time and are usually present in the ordered structures such as LLCs. As mentioned, shear flow can remove the defects, but it has been shown that defects might re-form at rest [100]. Re-formation of defects may lead to an increase in the storage modulus of the system that complicates the interpretation of the results.

1.4 Overview of current work

The overall objective of this research has been to design and develop new polymer membranes for water filtration applications using self-assembled Pluronic block copolymers, known as mesophases. The new proposed method is eco-friendly and does not require the use of any organic solvent for preparation of membranes. As mentioned in Section 1.3, mesophases are viscoelastic materials and their rheological properties affect their processability in different applications including membrane fabrication. Thus, a comprehensive study has been done on the rheological properties of mesophases in different flow fields (simple shear and oscillation). Additionally, the proposed templating method involved polymerization in nanoconfinement that required us to study the kinetics of polymerization in nanoconfinement that would be beneficial for scaling up the method. The remainder of this report is organized as follows. The materials and general methods used for characterization of the experimental samples are presented in Chapter 2. In Chapter 3, we provide a comprehensive experimental study on the rheological behavior of mesophases. In Chapter 4, we shed light on the effect of confinement on the kinetics of polymerization using chemorheology and differential scattering calorimetry (DSC) methods. The proposed templating method for making UF membranes is presented in Chapter 5. We summarize our findings in Chapter 6 and provide some outlook for future work.

Chapter 2: Materials and Methods

This chapter presents detailed information on the materials and experimental procedures described in this work. The calculation of the lattice parameters in different mesophase systems from small angle X-ray scattering (SAXS) data will be introduced. The procedures in this chapter have been published in references [42, 102–104].

2.1. Materials

The mesophases examined in this work are composed of three main phases: (1) aqueous phase, (2) oil phase, and (3) Pluronic block copolymer. In all samples, deionized (DI) water (0.055 $\mu\text{s}/\text{cm}$, EMD Millipore Direct-Q3) is used as the aqueous phase. The density of DI water at 25 °C is 1 g/mL.

Pluronics L64, P84, L121, and P123 are kindly provided by BASF. The physical data provided by the manufacturer are summarized in Appendix C.

For P84 and L121, p-xylene (Sigma-Aldrich) is used as the oil phase. The density of p-xylene at 25 °C is 0.861 g/mL. For P123, 1-butanol (Millipore) is used as the oil phase. The density of 1-butanol at 25 °C is 0.810 g/mL.

For membrane preparation, butyl acrylate ($\geq 99\%$, Sigma-Aldrich) and ethylene glycol dimethacrylate (purified, Electron Microscopy Sciences) are used as the monomer and crosslinker, respectively. Azobisisobutyronitrile (AIBN, 98%, Sigma-Aldrich) and 1-hydroxycyclohexyl phenyl ketone (HCPK, 99%, Sigma-Aldrich) are used as thermal and UV initiators, respectively.

To characterize the membrane performance, bovine serum albumin (BSA), from Sigma-Aldrich, is used as a solute for rejection tests. Poly(ethylene glycol), PEG, with molecular weight of 300 g/mol (PEG300, Sigma-Aldrich) is used as a model foulant. For molecular weight cut-off (MWCO) experiments, PEG with different molecular weights: 200, 400, 600, 1000, 1500, 4000, and 6000 g/mol are purchased from Alfa Aesar. All chemicals are used as received without further purification unless otherwise mentioned.

2.2 Mesophase preparation

Pluronic block copolymer, water, and the oil phase are mixed in a glass vial via centrifugation. In this process, samples are repeatedly centrifuged (2000 rpm) and rotated until a transparent mesophase is obtained. It should be noted that this centrifugation method is an effective mixing

procedure and does not lead to phase stratification for mixtures wherein the components have similar densities, as is the case for our system [43, 44, 105].

2.3 SAXS analysis

2.3.1 Methodology

SAXS measurements are performed utilizing a Bruker Nanostar System with a monochromated Cu K α radiation source at Los Alamos National Laboratory. SAXS samples are loaded into quartz capillaries with a nominal diameter of 1.5 mm (Charles Supper Company, Natick, MA) by centrifugation. Capillary tubes are then sealed using Critoseal and epoxy glue (JB Weld). The beam center and sample to detector distance are determined using silver behenate. One-dimensional (1D) scattering profiles are produced through azimuthal integration of the two-dimensional (2D) scattering patterns.

2.3.2 Determining different mesophase structures using SAXS

Lamellar, hexagonal, and micellar cubic mesophases can be identified using SAXS. Relative peak positions (q/q^*) is used to determine the structure of each sample, where q is the scattering vector and q^* is the principal peak in each 1D SAXS profile. Lamellar structures show 1:2:3:4... relative peak positions, hexagonal structures have 1: $\sqrt{3}$:2: $\sqrt{7}$:3... relative peak positions, and micellar cubic (body centered cubic, BCC) structures have relative peak positions of 1: $\sqrt{2}$:2: $\sqrt{6}$ Figure 2-1 shows the typical SAXS patterns for different mesophase structures.

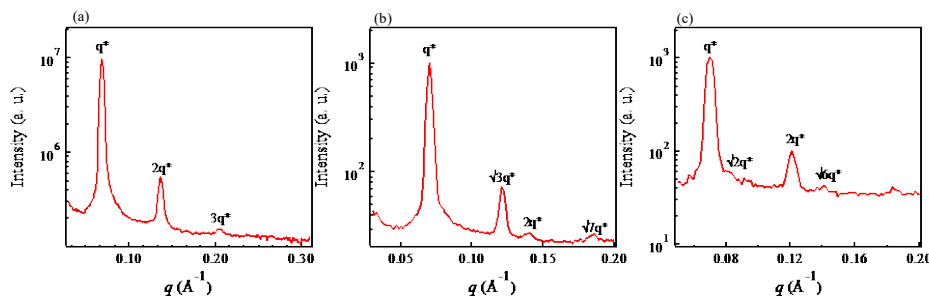


Figure 2-1. Typical SAXS patterns for different mesophase structures. (a) lamellar mesophases show 1:2:3:4... relative peak positions, (b) hexagonal mesophases show 1: $\sqrt{3}$:2: $\sqrt{7}$: relative peak positions, (c) BCC mesophases show 1: $\sqrt{2}$:2: $\sqrt{6}$... relative peak positions.

Details on the calculation of lattice parameter from SAXS data are presented in Appendix D.

Chapter 3: Rheological Characteristics of Mesophases of Block Copolymer Solutions

3.1. Introduction

Rheological properties of mesophases play an important role in their processability and final applications including the design of unit operations such as mixing, quality control, and formulation optimization. Extensive studies have been done on the rheological behavior of self-assembled block copolymer melts [39, 61, 70, 62–69]. Shear-induced orientation has been observed in lamellar and hexagonal mesophases, where the elastic modulus decreases by strain [71, 97, 106–108]. Shear deformation can affect both the macroscopic texture and also the mesoscopic orientation of the micelles; therefore, different methods such as small angle scattering techniques, nuclear magnetic resonance (NMR), and flow birefringence in conjunction with shear flow have been used to monitor the shear-induced orientation in mesophases in different length scales [98, 109–111]. It has been shown that both simple shear flow and large amplitude oscillatory shear (LAOS) flow can result in the alignment of mesophase systems [106]. The more the system is aligned, the lower is its elastic modulus [97, 100, 112, 113]. This phenomenon can be used to prove the shear-induced alignment in an indirect way. It should be noted that in LLC systems, different factors including the presence of defects, such as vacancies, dislocations, and grain boundaries [114], their elimination as a result of shear flow, and their re-formation at rest (over a long period), contribute to the behavior of the system under shear-induced alignment. In other words, if the system is free of defects, the reduction in elastic modulus does not relax back to its original state. However, the presence of defects with very long relaxation times can be misleading in interpretation of the decrease in elastic modulus of the system with alignment [100, 115]. Hahn and others [100] observed that the elastic modulus of a lamellar mesophase decreases monotonically during shear deformation due to the elimination of defects and the alignment of mesophases, but it increases during relaxation to a stable state as defects are spontaneously recreated in the system toward an unaligned state [100]. Figure 3-1 schematically shows three types of defects in LLC systems.

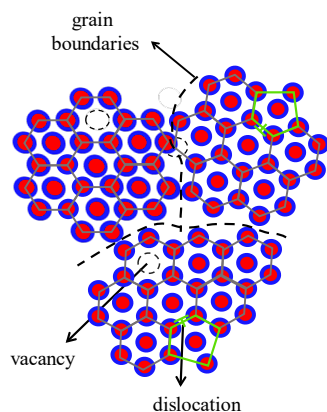


Figure 3-1. Cross section of a typical polycrystalline hexagonal mesophase shows three types of defect, namely vacancy, dislocation, and grain boundaries.

Mesophases show a viscoelastic behavior with a solid-like behavior in a relatively broad range of frequencies, which could be due to a combination of microscopic and mesoscopic domains. In the microscopic domain, the entanglement of block copolymer chains, microphase separated domains, and dynamic interfacial properties affect the rheology, while the domain size and intermicellar interactions are responsible for the observed rheological behavior in the mesoscopic scale [115].

Despite the versatile applications of ternary LLCs of amphiphilic block copolymers in two selective solvents, which have different mesostructures at a constant temperature, no comprehensive study has been reported on their rheology. In this chapter, we study the rheological characteristics of a series of LLCs with lamellar, normal hexagonal, and reverse hexagonal structures. Flow behavior, the possibility of shear banding, and stress relaxation mechanisms are discussed. Additionally, oscillatory shear experiments are performed to shed light on the viscoelasticity of mesophases.

3.2 Experimental Methodologies

3.2.1 Formulation design

Pluronic block copolymer, DI water, and *p*-xylene (in the case of Pluronic P84 and L121) or 1-butanol (in the case of Pluronic P123) are mixed in a glass vial through centrifugation. Different compositions for mesophases are determined based on their corresponding ternary phase diagram [43, 44, 105] as listed in Table 3-1. The PPO vol. fraction shows the volume fraction of PPO block in each Pluronic block copolymer. Oil and Pluronic vol. fractions are the volume fractions

of oil phase and Pluronic block copolymer is each sample, respectively. Water vol. fraction can be calculated from volume fractions of oil and Pluronic. Other parameters in Table 3-1 are explained in Appendix D. We have chosen a variety of compositions with a relatively wide range of lattice parameter and different types of mesophases for a comprehensive comparison between their rheological properties. The samples are coded with Pluronic/water/oil weight ratio, prefixed by Pluronic type. The type of structures is identified at the end of the sample name (L for lamellar, H₁ for normal hexagonal, and H₂ for reverse hexagonal).

Table 3-1. Composition and lattice size parameters for the samples used in this study.

sample	PPO vol. fraction	oil vol. fraction	Pluronic vol. fraction	ϕ	d or a (nm)	δ or α (nm)	polar domain size (nm)	grain size (nm)	D _H or D _L (nm)	M _H or M _L (nm)
P84_60/35/5_L	0.61	0.059	0.588	0.418	7.6	3.2	4.4	69.5	0.5	2.2
P84_40/35/25_L	0.61	0.074	0.487	0.371	9.8	3.6	6.2	70.0	0.7	2.4
P84_70/25/5_L	0.61	0.059	0.688	0.479	7.0	3.3	3.6	69.5	0.6	2.4
P84_50/45/5_H ₁	0.61	0.390	0.466	0.674	8.9	2.7	6.2	67.0	0.5	4.4
P84_60/15/25_H ₂	0.61	0.347	0.519	0.664	8.4	2.6	5.9	66.7	1.3	3.6
P84_40/15/45_H ₂	0.61	0.493	0.366	0.716	10.4	2.9	7.5	69.4	2.6	3.9
P123_50/45/5_H ₁	0.67	0.057	0.493	0.387	10.7	3.5	7.2	85.5	2.4	4.2
P123_60/35/5_L	0.67	0.060	0.590	0.455	8.7	4.0	4.8	72.2	1.2	2.6
L121_60/25/15_H ₂	0.91	0.171	0.583	0.701	14.0	4.0	9.9	69.3	0.6	6.7

3.2.2 Small angle X-ray scattering (SAXS) measurements

In order to confirm the mesostructure of samples, SAXS measurements are performed on all samples as described in Chapter 2.

3.2.3 Rheological measurements

Details on the rheological tests are presented in Appendix E.

3.3 Results and discussion

3.3.1 SAXS analyses

SAXS analysis, as typically shown in Figure 3-2, confirms the mesostructure of samples according to the phase diagrams reported in the literature. Relative peak positions (q/q^*) is used to determine the structure of each sample. SAXS graphs of other samples are shown in Appendix F.

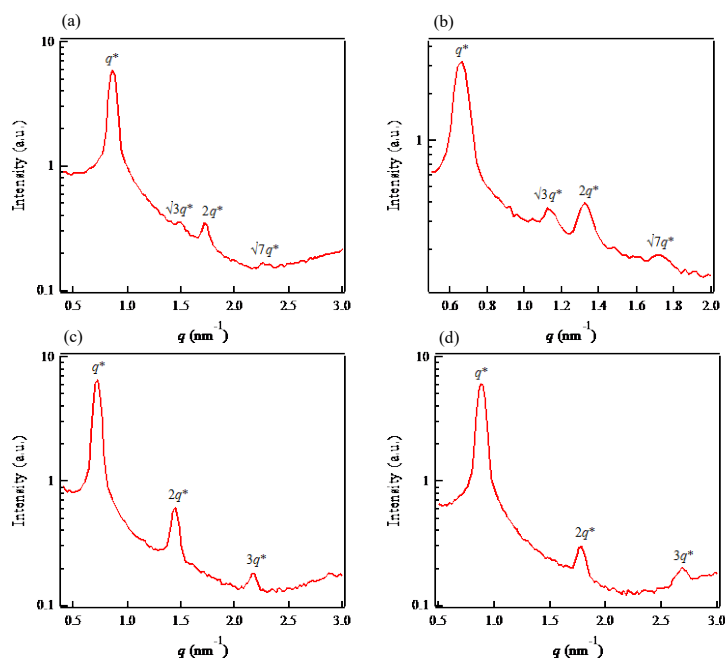


Figure 3-2. Typical SAXS graphs for lamellar and hexagonal mesophases: (a) P84_60/15/25_H₂, (b) P123_50/45/5_H₁, (c) P123_60/35/5_L, and (d) P84_70/25/5_L.

From the SAXS scattering profiles and using Bragg's law, lattice parameter, apolar domain size, and polar domain size for each mesophase is calculated. Calculated parameters from SAXS for all samples are listed in Table 3-1.

It should be noted that both 1-butanol and *p*-xylene can dissolve PEO with relatively small molecular weights. However, the selective solubility of aqueous copolymer solutions is only 4 wt% in *p*-xylene [116]. Pluronic P123 is insoluble in 1-butanol in the absence of water [44] and has a very low selective solubility, only up to 8 wt%, in the presence of water [44]. All the calculations assume that the water, PEO, PPO, and oil phases are completely segregated and that each component is characterized by its bulk density [116].

3.3.2 Rheological characteristics

Detailed experimental results on rheological characteristics of mesophases are reported in Appendix G. The results suggested that the shear banding may be present in the flow of the mesophases, but needs to be confirmed using velocimetry techniques. A typical rheo-SANS data on a lamellar sample suggested that there is no shear-induced structural transition in the sample, but shear-induced alignment takes place at high deformations (above the yield strain), intermicellar slippage happens, and a very slow relaxation time appears in the subsequent stress relaxation. Under high strains, shear-induced alignment occurs as a result of defect elimination, which leads to a decrease in the elastic modulus of mesophases. However, since the defects reform spontaneously, the mesophases relax back to their original viscoelastic properties with enough rest time.

Chapter 4: Studying the Polymerization in Soft Nanoconfinements of Lamellar and Reverse Hexagonal Mesophases Using Chemorheology

4.1. Introduction

Direct templating by preformed LLC phases has widely been used for producing organic and inorganic mesoporous materials [117–122]. As discussed in Chapter 1, in such cases, we deal with polymerization in nanoconfinement. It has been found that confinement is one of the main factors contributing to the polymerization rate. As the system is more confined, the local monomer concentration increases, which leads to a higher termination rate and a lower polymerization rate [123]. Figure 4-1 schematically shows the effect of confinement.

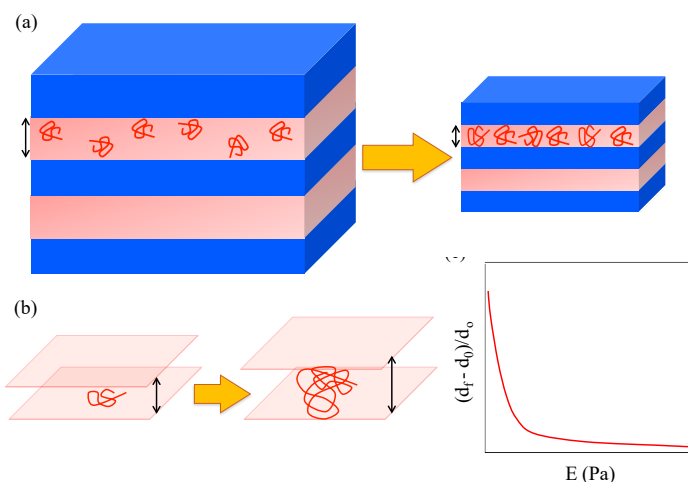


Figure 4-1. Schematic illustration of: (a) the effect of confinement on the probability of termination reactions, (b) the increase in domain size upon polymerization due to the tendency of polymer chains to form random coils, and (c) the expected dependence of a change in domain size upon polymerization to the template modulus (see Equation (4-1)).

In soft nanoconfinements, the template stiffness also plays a role in the polymerization kinetics. In other words, as the degree of polymerization increases, polymer chains tend toward random coil conformations to minimize their free energy (Figure 4-1b). If the template stiffness cannot suppress the tendency of the random coil conformation, the domain size will increase. In an ideal case, the higher the elastic modulus of a soft template, the lower is the change in the domain size upon polymerization; thus, the higher is the effect of confinement at a fixed initial domain size (Figure 4-1c). Hard templates can be considered to have infinite moduli with no change in the

domain size, whereas a template with zero modulus will be destroyed upon polymerization (maximum change in domain size). Therefore, we can suggest the following scaling relationship:

$$\frac{d_f - d_0}{d_0} \propto \frac{1}{E^n} \quad (4-1)$$

where d_f and d_0 are the final and initial domain sizes, E is the elastic modulus, and n has a value equal to or higher than unity. A deviation from this scaling suggests that properties of the template change during polymerization. As discussed, the degree of confinement is the prominent factor affecting the polymerization kinetics in nanoconfinement. The degree of confinement in turn is influenced by three factors, including the size of the confinement, the elastic modulus of the template, and the interfacial properties of the template.

In this chapter, we use chemorheology to study the kinetics of polymerization in soft nanoconfinement. Mesophases with the same amount of monomer phase but different structures are used to cancel the effect of monomer and initiator concentration on the polymerization rate. Differential scanning calorimetry (DSC) is used to confirm the kinetics of polymerization derived from chemorheology.

4.2 Experimental Methodologies

Detailed experimental methodologies are presented in Appendix H. We have used different Pluronic block copolymers while keeping the concentration of the polymerizing phase at 25 wt%. Two lamellar, L_α , mesophases were prepared with P84/water/monomers 60/15/25 wt% and L121/water/monomers 57/18/25 wt%, and two inverse hexagonal, H_2 , mesophases with P84/water/monomers 40/35/25 wt% and L64/water/monomers 55/20/25 wt%.

4.3 Results and discussion

4.3.1 SAXS analyses

To confirm the retention of mesostructures upon thermal polymerization, SAXS studies are done on the mesophases before and after polymerization and the relative positions of Bragg peaks (q/q^*) are used to determine the structure of each sample. Detailed SAXS results are presented in Appendix H.

4.3.2. Rheological measurements

Frequency sweep results for lamellar and reverse hexagonal mesophases are discussed in Appendix H. Variations of the dynamic moduli with time at three different temperatures for the lamellar and reverse hexagonal samples are shown in Figure 4-2. Three stages of polymerization can be found: (1) induction, where G' is relatively constant in the beginning of the experiment for

a period indicated as t_{in} ; (2) propagation, where G' sharply increases by time; and (3) final curing and termination, where G' reaches a plateau.

Gel point terminology in the conventional chemorheology literature cannot be applied here because of the solid-like behavior of the samples [124]. Additionally, the $G'=G''$ or $\tan \delta=1$ criterion [125] cannot be used as no crossover between dynamic moduli is observed. Considering the gel point as the time when G'' is maximal does not work either since G'' does not show a maximum in the samples under study [125–127]. Therefore, the evolution of dynamic moduli and complex viscosity are fitted using Arrhenius-type models to determine the kinetic constants [128].

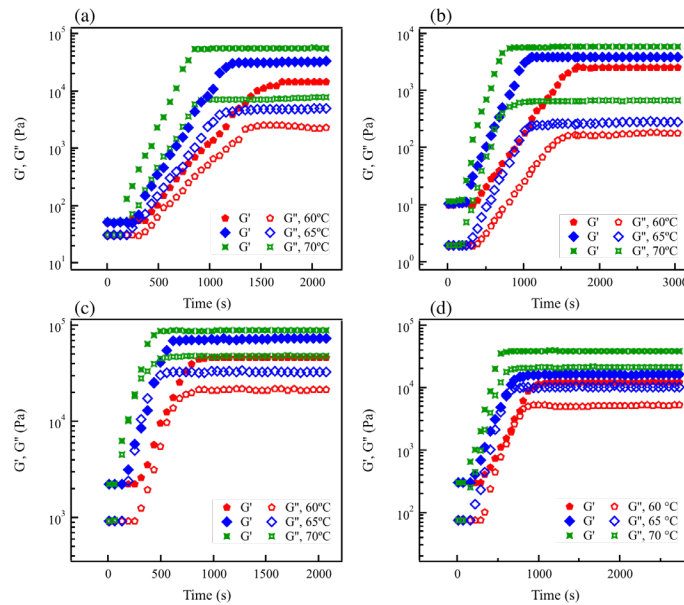


Figure 4-2. Variation of dynamic moduli with time at three different temperatures (60, 65, and 70 °C) for (a) P84- L_{α} , (b) L121- L_{α} , (c) P84- H_2 , and (d) L64- H_2 samples.

Activation energy in the induction step can be modeled using an Arrhenius model as follows for the induction time, t_{in} :

$$t_{in} = A_{in} e^{\left(\frac{E_{in}}{RT}\right)} \quad (4-2)$$

where E_{in} , R , T , and A_{in} are the induction activation energy, gas constant, absolute temperature, and the pre-exponential factor, respectively. See Appendix H for details on induction activation energy of each sample.

The values of the induction activation energy for different samples are shown in Table 4-1.

Table 4-1. Model parameters for the initiation and propagation steps of polymerization in the bulk, lamellar and reverse hexagonal samples. $\eta_{\omega=1rad/s}^*$ is the complex viscosity at angular frequency of 1 rad/s.

Sample	T	E_{in}	K	E_p	Confinement size	Change in apolar domain size	$\eta_{\omega=1rad/s}^*$
Unit	°C	kJ/mol	$10^{-3}/s$	kJ/mol	nm	nm	Pa.s
Bulk	60		21.6				
	65	38±11	24.1	39±2	NA	NA	NA
	70		32.4				
P84- L_α	60		4.7				
	65	104±12	6.5	65±3	0.8	0.12	9.55
	70		9.3				
L121- L_α	60		4.3				
	65	96±27	7.6	66±2	1.2	1.85	1.86
	70		9.4				
P84- H_2	60		5.4				
	65	141±13	8.5	69±4	1.3	11.02	384.86
	70		11.8				
L64- H_2	60		5.7				
	65	138±6	7.9	68±3	1.5	0.09	49.93
	70		11.0				

To calculate the polymerization rate, the evolution of the LLC complex viscosity, $|\eta^*|$, during polymerization (Figure 4-3) was used. A first order double Arrhenius model was used to describe the chemorheological data [127, 128]:

$$\ln|\eta^*| = \ln|\eta_v^*| + \frac{E_v}{RT} + tK \quad (4-3)$$

where $|\eta_v^*|$ is the initial complex viscosity before polymerization, and E_v is the viscous activation energy. K is the polymerization rate constant, which is related to the curing temperature as:

$$K = k_0 \exp\left(\frac{-E_p}{RT}\right) \quad (4-4)$$

where E_p is the activation energy of polymerization.

From Figure 4-4, the initial complex viscosity of the samples, shown by an arrow in the graphs, does not change with temperature, which can be attributed to the confined structure of LLCs that

hinders free movement. Therefore, thermal dependency of viscosity is negligible ($E_v = 0$). The polymerization region of $|\eta^*|$ versus time is fitted with Equation (4-4) and the model parameters are summarized in Table 4-1. The polymerization rate in the reverse hexagonal confinement is higher than that of the lamellar ones. We believe the degree of confinement [118, 129] contributes to the higher polymerization rate in the reverse hexagonal mesophases.

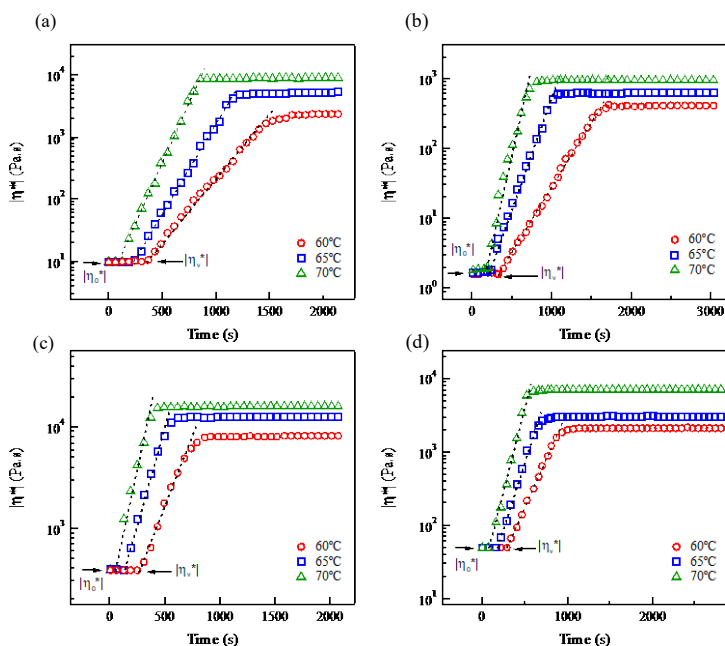


Figure 4-3. Evolution of complex viscosity at different curing temperatures for (a) P84- L_α , (b) L121- L_α , (c) P84- H_2 , and (d) L64- H_2 samples. The dashed lines show the fitted slope in the propagation step.

As discussed in the introduction, the degree of confinement can be correlated with the interfacial properties of the confinement, elastic modulus of the confinement [130, 131], and the confinement domain size [132, 133]. From the rheological data, the reverse hexagonal mesophases have higher storage moduli compared to the lamellar ones. Therefore, according to Equation (4-1), we ideally expect to see a smaller change in the domain size upon polymerization. However, SAXS results in Table 4-1 show that the P84- H_2 mesophase has a higher change in domain size upon polymerization compared to the P84- L_α sample. The deviation from Equation (4-1) is attributed to dynamic changes in the interfacial properties of the mesophases and shows that factors other than storage moduli are responsible for the change in domain size. The change in domain size results show that reverse hexagonal mesophases offer

less degree of confinement than the lamellar ones for the growing polymer chains, and that results in a higher rate of polymerization.

Additionally, as shown in Figure 4-4, the size of confinement in the reverse hexagonal and lamellar systems can be calculated from the radius of the biggest circle ($R_{h,max}$ and $R_{l,max}$) that can be contained in the apolar domain (the bigger the sphere, the bigger the confinement size). The radius of such a circle is equal to half of the monomeric domain size in the lamellar samples, as:

$$R_{l,max} = \frac{D_1}{2} \quad (4-5)$$

whereas for reverse hexagonal mesophases, $R_{h,max}$ is obtained as follows:

$$R_{h,max} = \sqrt{\frac{A_h}{\pi}} \quad (4-6.a)$$

$$A_h = \frac{a^2\sqrt{3}}{4} - \frac{\pi(M_H)^2}{2} \quad (4-6.b)$$

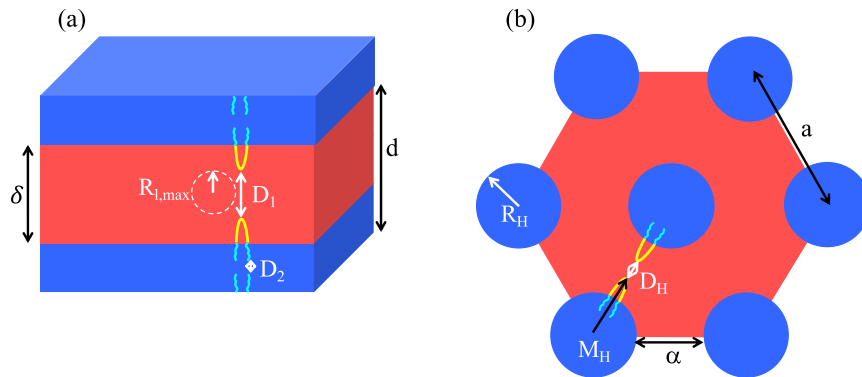


Figure 4-4. Schematic illustration of the parameters obtained from SAXS and confinement size in (a) lamellar and (b) reverse hexagonal mesophases.

Based on the geometrical analysis:

$$M_H = a \sqrt{\frac{\sqrt{3}}{2\pi} (\varphi_{water} + \varphi_{Pluronic})} \quad (4-7)$$

The lattice parameter, a , values from SAXS data are 6.6 nm and 7.4 nm for P84-H₂ and L64-H₂ samples, respectively. Also, volume fractions of water, φ_{water} , and monomer phases, $\varphi_{Monomer}$, in P84-H₂ and L64-H₂ are reported in Table 4-2.

Table 4-2. Values of the necessary parameters for calculating $R_{h,max}$ in the reverse hexagonal samples.

Sample	φ_{water}	$\varphi_{monomer}$	M_H (nm)	A_h (nm ²)	$R_{h,max}$ (nm)
P84-H ₂	0.35	0.38	3.0	5.5	1.3
L64-H ₂	0.2	0.52	3.3	7.1	1.5

Confinement sizes are calculated for all samples based on the data provided in Table 4-2 and are reported in Table 4-1. We observe that for the same polymer chain, the lamellar mesophases provide a greater degree of confinement, thus smaller confinement size compared to the hexagonal ones.

Results in Table 4-1 show that the polymerization rate decreases with increasing confinement size. In the confined structures, the probability of two macroradicals to react with each other increases, and that leads to a higher termination rate. Therefore, the rate of polymerization as well as the degree of conversion decrease [123]. In fact, we can consider the mesophase polymerization similar to the polymerizations of a dispersed phase in mini-emulsions and emulsions. In such systems, the concentration of radicals in the dispersed phase varies depending on the volume of the monomer droplets/polymer particles dispersed in the continuous phase [134, 135]. In this work, rather than being confined inside droplets of a dispersed phase, the reaction is confined within the structures of the lamellar and reverse hexagonal mesophases. Salsamendi and coworkers have considered the confinement effects experienced by propagating radicals to explain the significantly reduced rate of polymerization [136]. They developed a mathematical model to take into account the segregation effects on the polymerization rate. Their segregation model predicts that bulk free radical polymerization would proceed at a much faster rate compared to the nanoconfined structure. Our data show that the polymerization proceeds significantly faster in the bulk state compared to the reverse hexagonal samples. The lamellar systems have the slowest polymerization rates. Therefore, our results are in agreement with the segregation model, which predicts that as the degree of confinement increases, the probability of the termination increases due to the higher local radical concentration resulting in a slower rate of polymerization [136].

Chemorheology results show that the final values of dynamic moduli increase with curing temperature (Figure 4-2). Mechanical properties of the crosslinked polymer control the storage modulus of each sample that in turn is proportional to the reaction conversion. In order to confirm this hypothesis, the conversion of the samples cured at different temperatures is measured using the gravimetric technique and plotted against the curing temperature (Figure 4-5). After the polymerization is ended, we measured the rheological properties of each cured sample at different temperatures to investigate the temperature dependency of the final elastic modulus (data shown in Figure 4-6). We found that the storage modulus of polymerized samples decreases with increasing temperature from 25 to 70 °C, because the polymer network becomes

softer by increasing the temperature. In addition, according to poroelasticity theory, the decrease in elastic modulus of polymerized mesophases could be due to the decrease in the water viscosity with temperature [137, 138]. Final elastic moduli of the samples, measured at 70 °C (to remove the effect of temperature), are plotted against the conversion in Figure 4-5b. The results suggest that G'_{final} is correlated linearly with the reaction conversion within the studied range of temperature. The enhanced conversion with increasing curing temperature is attributed to the increase in polymerization rate and monomer diffusion coefficients [127].

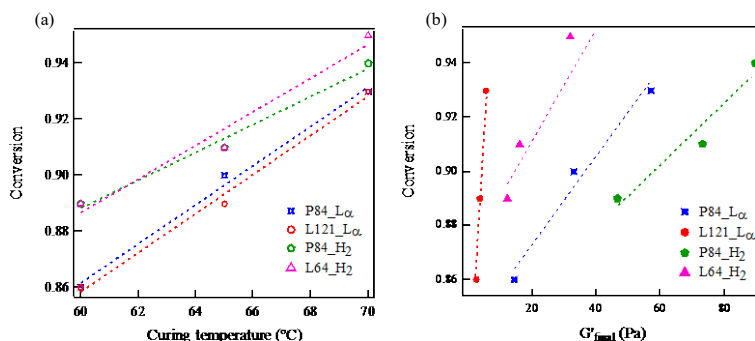


Figure 4-5. (a) Effect of curing temperature on conversion of each mesophase system. (b) Effect of conversion on the final mechanical properties of each sample.

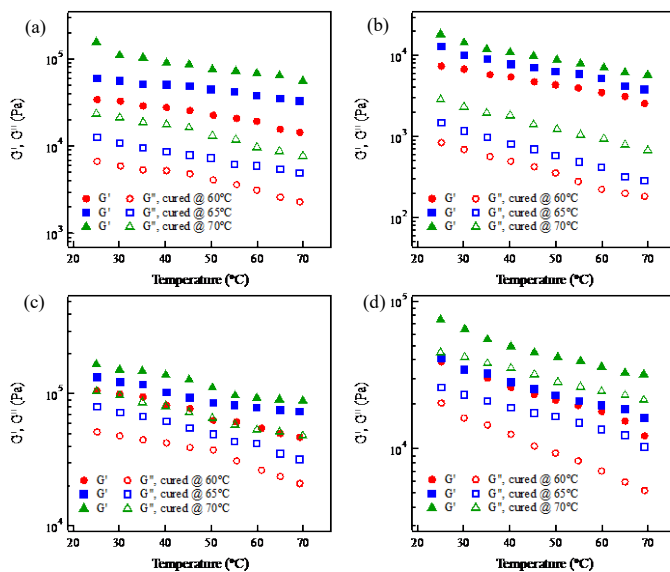


Figure 4-6. Temperature sweep of dynamic moduli of polymerized mesophases: (a) P84-L α (60/15/25), (b) L121-L α (57/18/25), (c) P84-H $_2$ (40/35/25), and (d) L64-H $_2$ (55/20/25) samples, cured at different temperatures (shown in the legend).

4.3.3 DSC measurements

To confirm the kinetic parameters obtained from chemorheological studies, DSC is performed on two typical samples with lamellar and hexagonal structures (P84- L_α and P84- H_2). Details are presented in Appendix H.

4.4 Conclusion

In this work, we describe a detailed analysis of the thermal polymerization kinetics of monomers in ternary lyotropic liquid crystal systems. By comparing the rate of polymerization in various liquid crystalline phases, the effects of nanoconfinement and template softness have been elucidated. Three stages of polymerization (i.e., initiation, propagation, and termination) are observed in the chemorheology and DSC measurements. We observe that the viscosity of the mesophases contributes to the initial and total activation energy of the polymerization. In our system, the higher viscosity of the reverse hexagonal mesophase at the early stages of the polymerization leads to the higher activation energy compared to the lamellar and bulk samples. The results from the chemorheology and DSC also show that the rate of polymerization decreases significantly in confined structures compared to the bulk polymerization. Additionally, the polymerization rate is higher in reverse hexagonal mesophases than for that of the lamellar structures. This phenomenon is attributed to the segregation effects in which as the degree of confinement increases, the probability of termination increases due to the higher local radical concentration. The degree of confinement in our system is correlated with the confinement size, elastic modulus of the template, and the interfacial properties of the template. We show that the reverse hexagonal structure offers a lesser degree of confinement for the growing polymer chains. At the final stages of the polymerization, a lower limiting conversion is observed in the lamellar systems compared to the reverse hexagonal ones. This is attributed to the higher degree of confinement in the lamellar mesophases that leads to a higher rate of termination in the late stages of polymerization.

Chapter 5: Ultrafiltration Membranes from Polymerization of Self-Assembled Pluronic Block Copolymer Mesophases

5.1 Introduction

Ultrafiltration (UF) is one of the most commonly employed separation techniques with applications in a variety of industries ranging from food processing to chemical manufacturing and protein purification [139–142]. In the treatment of water and wastewater, UF plays a key role in the removal of suspended particles, viruses, and bacteria [143–145].

The most common approach taken in the development of improved UF membranes has been surface modification. Grafting hydrophilic groups, such as poly(ethylene glycol), to the surface of membranes has been proven to reduce fouling [146, 147]. However, surface modification is costly. Another approach, a combination of polymer self-assembly and NIPS, referred to as SNIPS, affords resultant membranes with high flux and anti-fouling properties [30, 148, 149]. However, as discussed in Chapter 1, the SNIPS method still requires large quantities of organic solvent and, as such, is not eco-friendly [30]. Templating [81, 118, 150, 151] is an alternative route to porous membranes in which a structured or porous material is used as a template to impart structure to another material and subsequently removed.

In the current work, the self-assembled mesostructures of a commercially available Pluronic block copolymer (Pluronic L64) in water and an oil phase consisting of monomers are employed as templates for the preparation of UF membranes without the need for organic solvents. Hexagonal and lamellar mesophases are prepared by changing the concentration of Pluronic L64 and the water/monomer ratio. Polymerization of the monomer phase via a thermal/photo-initiation system followed by extraction of the aqueous phase and block copolymer generally retains the template structure, generating pores in the resultant membrane (Figure 5-1). Membrane performance is found to be superior to that of a commercial NIPS UF membrane (GE, PT Series, PT8040F30) in terms of permeability, flux decline, and rejection of both bovine serum albumin and Direct Red 23 dye.

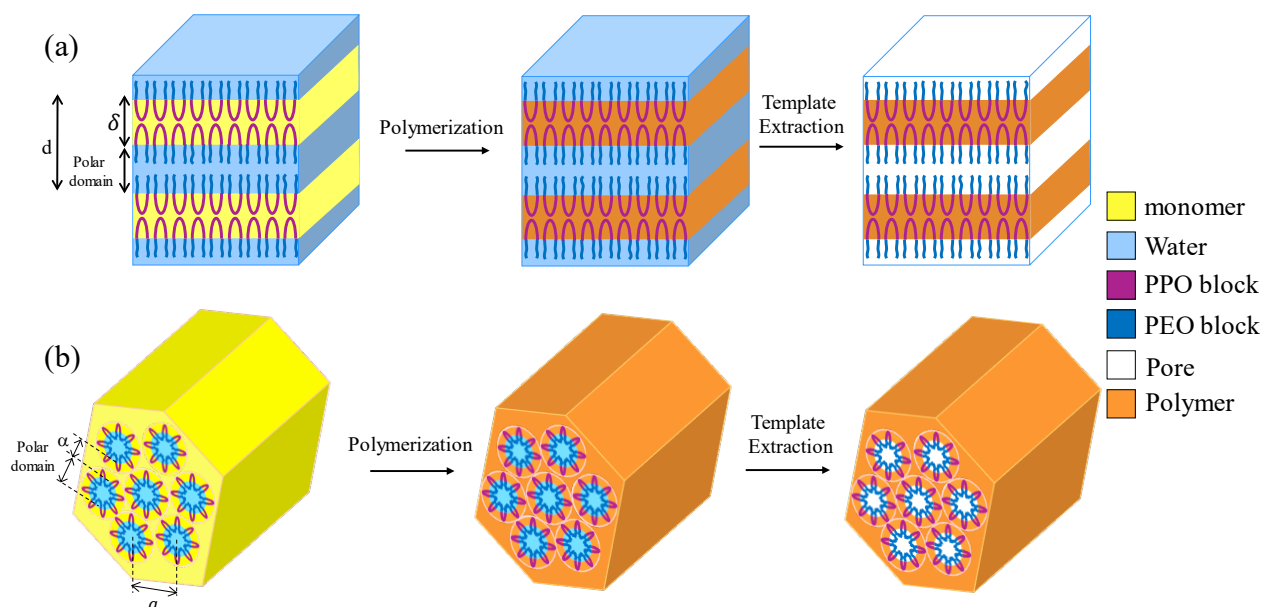


Figure 5-1. Schematic representation of templating method for making mesoporous polymers using (a) lamellar and (b) hexagonal mesophases. Oil phase consists of monomer, crosslinker, and initiators.

5.2 Experimental Procedures

5.2.1 Preparation of lamellar and hexagonal mesophases

Pluronic L64, water, and an oil phase, which consisted of monomer, crosslinker, and initiator, are mixed in a glass vial via centrifugation. Four different compositions, shown in Table 5-1, are chosen based on the lamellar and hexagonal regions of a similar phase diagram developed by Alexandridis and others. [116].

5.2.2 Cross-polarized light microscopy

A cross-polarized Olympus microscope (model BX60) is used to characterize the liquid crystalline structure of mesophases before and after the polymerization. A small amount of each mesophase (before polymerization) is placed on a glass slide and covered with a glass cover slip. Cross-polarized images of samples are recorded using a microscope-mounted digital camera.

Table 5-1. Formulation design of the synthesized membranes.

Membrane	Pluronic/water/oil ^a composition (wt.%)	Mesophase structure
I	60/30/10	Lamellar
II	50/35/15	Lamellar
III	60/15/25	Hexagonal
IV	55/15/30	Hexagonal

^aThe oil phase consisted of monomer, crosslinker, HCPK, and AIBN, where the crosslinker, HCPK, and AIBN concentrations were 33, 5, and 5 wt. % with respect to the monomer, respectively.

5.2.3 SAXS measurements

SAXS is used to determine the structure of each mesophase before and after polymerization.

5.2.4. Preparation of the membranes

To control for effects arising from the membrane support, membranes are prepared using a polyethylene nonwoven fiber support recovered from the commercial UF membrane using a Soxhlet extraction with chloroform. The detailed fabrication procedure is presented in Appendix I.

5.2.5 Membrane performance measurements

5.2.5.1 Water permeability

Membrane permeability is determined using a high pressure stirred cell (Sterlitech Corporation) in a dead-end filtration mode with the stirring rate of 750 rpm. Darcy's law is used to calculate the permeability as follows:

$$\frac{\kappa}{l} = \frac{Q_m \mu}{A_m \Delta P} \quad (5-1)$$

where Q_m , μ , A_m , ΔP , l , and κ are the flow rate, viscosity, membrane area, pressure difference along the membrane, membrane thickness, and Darcy's constant (intrinsic permeability), respectively. The ratio of κ/l is considered as an indication of operational permeability in this work due to modest thickness variation across synthesized membranes, which limit direct comparisons between different membranes. DI water is filtered through the membranes under 1.5 bar applied N₂ pressure. Membrane effective area is constant in all samples, 14.6 cm². As noted

previously, a commercial UF membrane (GE, PT Series, PT8040F30) with a MWCO of 5 kDa (pore size of ~2.9 nm) is used as a control in this study.

5.2.5.2 Separation capability

To evaluate membrane separation capability, BSA is used as a feed solution solute. Then 1 mg/mL BSA solutions in water are prepared and passed through membranes in a dead-end filtration mode. Concentration of solute in the feed and permeate are measured using a UV-Vis spectrophotometer (UV-1800, Shimadzu). Solute rejection (r) is calculated based on the following equation:

$$r = \left(1 - \frac{C_p}{C_f}\right) \times 100\% \quad (5-2)$$

where C_p and C_f are the concentrations of permeate and feed, respectively.

5.2.5.3 Fouling resistance

A Sterlitech high pressure stirred cell filtration apparatus is used to determine the fouling resistance of synthesized membranes. Solutions of 1 mg/mL BSA and 1 mg/mL poly(ethylene glycol) with a molecular weight of 300 g/mol (PEG300) are used as the feed. Fouling tests are performed over a period of 12 hours in a dead-end flow configuration with permeate volume collected in 10-30 min intervals. Permeate flux is calculated and plotted against collection time to assess the flux decline over time due to fouling.

5.2.5.4 MWCO measurements

To determine the MWCO of membranes, 1 g/L aqueous solutions of PEG with different molecular weights (200-6000 g/mol) are passed through them. A total organic carbon (TOC) analyzer (Shimadzu, TOC-L series) is used to determine the PEG concentration in the permeates, and the rejection values are calculated from Equation (5-2). Each TOC measurement is performed five times and average values are reported. MWCO is defined as the molecular weight of the PEG molecule that gives a 90% rejection [152].

5.3 Results and discussion

5.3.1 Mesophase characterization

Shown in Figure 5-2 are the cross-polarized micrographs obtained for mesophases before and after polymerization. The streaky oil texture highlighted in Figure 5-2 for both samples I and II before polymerization are indicative of a lamellar structure [29], while the fan texture of samples

III and IV are characteristic of hexagonal liquid crystals [30]. Following polymerization, the absence of extinction (a dark image) indicates that the structure remains anisotropic. As such, these results suggest that all mesophases retain a liquid crystal structure after curing. SAXS measurements further validate this finding and shed light on the exact structure of each sample.

SAXS data obtained for lamellar and hexagonal mesophases before and after polymerization are shown in Figure 5-3, where the left columns show the SAXS patterns before polymerization and the right columns show the SAXS data of the polymerized samples.

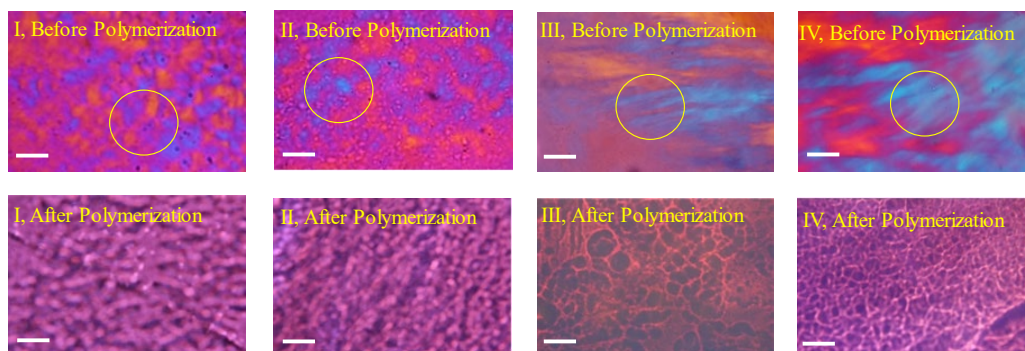


Figure 5-2. Cross-polarized light micrographs obtained for mesophases before and after polymerization with compositions I, II, III, and IV, as listed in Table 5-1. Scale bar: 50 μm .

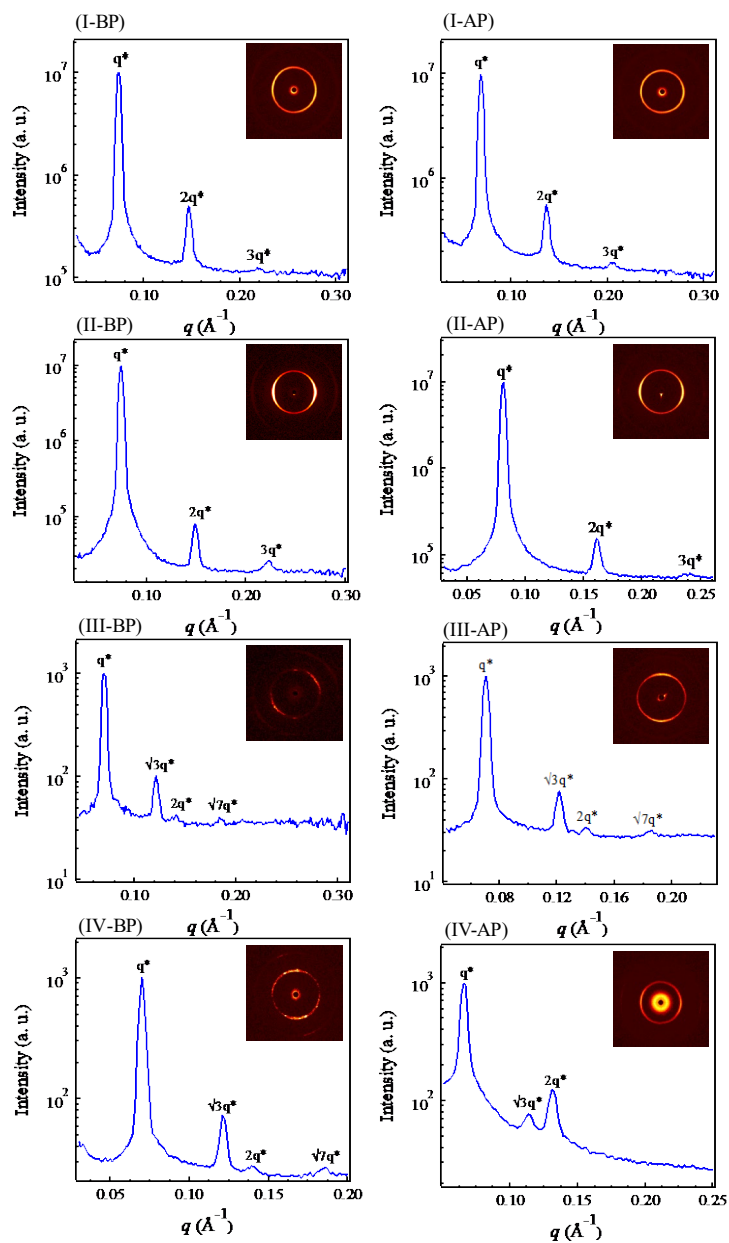


Figure 5-3. 1D and 2D scattering profiles for mesophases before (left column, BP) and after (right column, AP) polymerization for compositions I, II, III, and IV, listed in Table 5-1.

Mesophase structures are determined using the relative peak positions (q/q^*) as discussed in Chapter 2. It should be noted that the anisotropy evident in the 2D scattering pattern displayed in the inset of Figure 5-3 (III-BP) could indicate the presence of a hexagonal modulated or perforated lamellae (HM/HPL) phase, often found in close proximity to a purely hexagonal phase [153]. This is further confirmed by the presence of pre- and post-primary shoulders in the 1D scattering profile, indexed in Figure I-3 in Appendix I, which provide further evidence that the pre-polymerized mesophase observed for sample III is an HM/HPL structure. Despite this, as can be seen in Figure 5-3 (III-AP), upon polymerization sample III adopts a purely hexagonal morphology.

Lattice parameters and apolar domain sizes for lamellar and hexagonal mesophases both before and after polymerization are calculated according to Chapter 2 and are presented in Table 5-2. It can be seen that lattice parameter increases upon polymerization. From the scattering profiles, the pore size of the mesophase-templated polymers can be determined using Bragg's law.

To calculate membrane pore size, we assume that the pores constitute the space left vacant by the removal of the water. The volume fraction of water, φ_{water} , in the polar domain of lamellar and hexagonal mesophases are reported in Table 5-2. Similar to the SAXS parameter calculations provided in Chapter 2, the height of the rectangular pores in the lamellar samples, $H_{P,lam}$, and the diameter of cylindrical pores in the hexagonal samples, $D_{P,hex}$, can thus be calculated as follows:

$$H_{P,lam} = \varphi_{water}d \quad (5-3)$$

$$D_{P,hex} = a \left(\frac{\sqrt{3}}{2\pi} \varphi_{water} \right)^{1/2} \quad (5-4)$$

As shown in Table 5-2, all samples were found to have a pore size of less than 5 nm.

Table 5-2. Calculated parameters for lamellar and hexagonal mesophases before polymerization (BP) and after polymerization (AP).

Sample	Structure	ϕ	d or a (nm)		δ or α (nm)		φ_{water}	φ_m	Pore size (nm)
			BP	AP	BP	AP			
I	Lamellar	0.48	0.5	0.2	0.1	0.4	0.3	0.11	2.8
II	Lamellar	0.46	0.4	0.8	0.4	0.6	0.36	0.16	2.8
III	Hexagonal	0.68	0.4	0.7	0.2	0.3	0.13	0.38	4.0
IV	Hexagonal	0.64	0.2	0.4	0.8	0.9	0.15	0.31	4.2

As listed in Table 5-2, polymerization results in a modest increase in both the lattice parameter and apolar domain size. Both decrease and increase in the domain spacing upon polymerization have been reported in the literature. The former has been explained in terms of a density change

within the polymerized region [118], whereas the latter is attributed to changes in the original LLC structure [154]. We attribute the observed increase in the domain size to a competition between thermodynamics and kinetics. On one hand, as the polymerization proceeds, the molecular weight of the oil phase and consequently, χN , a measure of the enthalpic penalty of mixing, approach infinity. This dramatic increase in the enthalpic penalty can overcome the entropic contribution to free energy, driving the system toward phase separation, leading to an increase in the domain size. Changes in the surface energy of the polymerizing phase can also lead to a phase transition or inversion in the self-assembled structure. On the other hand, in our system, the polymerization results in a density increase (shrinkage with $\Delta\rho\sim 10\%$). Since crosslinking arrests molecular rearrangement, trapping the structure in a non-equilibrium morphology can be achieved if the ordering kinetics are slower than the reaction kinetics [155]. As such, the reaction kinetics and crosslinker content are of critical importance for limiting polymerization induced phase inversion/transition. Additionally, this explains the observed transition from an HM/HPL morphology to a hexagonal one. As shown in Table 5-2, expansion of the lattice parameter and apolar domain size is less significant when the monomer volume fraction increases. We attribute this to a higher shrinkage of the oil phase upon polymerization since the volume reduction is directly proportional to the overall concentration of the oil phase.

In contrast to the above discussion, a slight decrease or increase in the domain size with increasing temperature has been observed for the unpolymerized mesophases [156]. It should be noted that this behavior is representative of the equilibrium self-assembly and not the morphology induced by the polymerization described above. Despite this, it is evident from Figure I-4 (see Appendix I), which displays 1D SAXS profiles as a function of temperature for sample I, that the mesostructure appears stable during the temperature sweep and does not exhibit thermally induced phase separation (the measurement duration is shorter than time required for polymerization). The observed decrease in the principal scattering vector with increasing temperature suggests that the increase in domain size can be attributed to a change in the surface energy of the polymerizing phase. Additionally, this result provides evidence that the employed thermal initiation process should not have a significant effect on the nanoscale structure of the membrane. The limited morphological changes observed by SAXS and polarized light microscopy suggest that the wide stability window of the studied mesophases and rapid arrestment of morphological changes through crosslinking make this process fairly robust. This is a significant finding as, for many of the systems described in the literature, elimination of polymerization induced phase separation generally requires the use of polymerizable surfactants [19]. The method presented in this paper is both scalable and flexible, utilizing a commercially available surfactant. Additionally, monomer chemistry and surfactant are easily adaptable, enabling production of membranes tailored in terms of surface chemistry and pore size.

5.3.2 Membrane performance

The permeabilities and flow rates through each membrane are tabulated in Table 5-3. Both the lamellar and hexagonal membranes are found to have higher permeabilities than the commercial membrane, with the lamellar membranes displaying the highest permeabilities despite a smaller characteristic pore size. We believe that the geometry of the nanostructure plays a critical role in the flow properties of the membranes. While lamellar mesophases impose 1D flow confinement (slit shaped channel), the flow in hexagonal structures is confined in 2D (cylindrical channels). Because 1D confinement provides more degrees of freedom for the fluid flow than 2D confinement, the higher permeability of lamellar membranes is expected.

Tortuosity, T , is defined as the ratio of effective path for water flow, l_e , to the thickness of the membrane, l :

$$T = l_e/l \quad (5-5)$$

For randomly oriented lamellar and hexagonal channels, the tortuosity has been calculated as 1.5 and 3, respectively [157, 158]; whereas it is equal to 1 for perfectly aligned channels.

Table 5-3. Flow rate, normalized permeability, BSA rejection, and tortuosity of as-synthesized lamellar and hexagonal membranes compared to a commercial one.

Parameter	Unit	Commercial membrane ^a	Membrane I	Membrane II	Membrane III	Membrane IV
Q	L/hr	0.12±0.01	0.25±0.01	0.24±0.02	0.21±0.03	0.22±0.01
κ/l	10 ⁻¹⁰ L/m ²	1.47±0.01	3.05±0.01	2.97±0.01	2.60±0.01	2.69±0.01
BSA rejection	%	<68%	>95%	>95%	>95%	>95%
Direct Red 23 rejection	%	90%	>99%	>99%	>99%	>99%
Tortuous (effective) path length	10 ⁻⁷ m	N/A	6.3 ± 0.30	7.70 ± 0.7	(7.6 ± 1.2)×10 ⁻¹	1.1 ± 0.1

^a The commercial membrane was a GE, PT8040F30.

We can determine the tortuosity of membranes and shed light on the flux differences observed between lamellar and hexagonal mesophases. The permeation of water through lamellar and hexagonal channels is considered as water flow through a slit and a tube, respectively. Their corresponding volumetric flow rates are defined as follows:

$$Q_{e,lam} = \frac{\Delta P H_{P,lam}^3 W}{12 \mu l_e} \quad (5-6)$$

$$Q_{e,hex} = \frac{\pi \Delta P D_{P,hex}^4}{128 \mu l_e} \quad (5-7)$$

where $Q_{e,lam}$ and $Q_{e,hex}$ are the volumetric flow rates for one channel in lamellar and hexagonal membranes with pore sizes of $H_{P,lam}$ and $D_{P,hex}$, respectively. ΔP , μ , and W are the pressure difference along the membrane thickness, water viscosity, and lamellar(hexagonal) grain size ($\sim 0.1 \mu m$, this estimate will be discussed later), respectively. $Q_{e,lam}$ and $Q_{e,hex}$ are calculated by dividing the total measured volumetric flow rates from Table 5-3 by the number of channels per membrane surface, N_m . For the lamellar and hexagonal structures, the number of channels per membrane surface area are calculated as follows:

$$N_{lam} = \frac{A_m}{wd} \quad (5-8)$$

$$N_{hex} = \frac{2A_m}{\sqrt{3}a^2} \quad (5-9)$$

Note that this calculation assumes all channels are oriented, whereas in reality some channels may be laying perpendicular to the surface. Effective path values for each membrane has been calculated in Table 5-3. At the same membrane thickness, the higher the effective path, the higher the tortuosity value. It can be seen that, despite exhibiting higher flow rates than their hexagonal counterparts (III & IV), the lamellar membranes (I& II) displayed a more tortuous path. This observation can be attributed to the difference in flow geometry.

Using the measured membrane thickness ($\sim 210 \mu m$), the tortuosity of the lamellar and hexagonal membranes can be calculated. Our results are listed in Table 5-3. Mesophase orientations for samples III and IV were found to be approximately random with a tortuosity close to 3. However, for samples I and II, the orientation is not random.

Grain boundaries in ordered phases can lead to dead-end pores and restrict flow, affecting the tortuosity, as shown schematically in Figure 5-4. In fact, single units of each mesophase stack and may orient in different directions to form the ultimate structure. Using the Scherrer relation, $grain\ size = \frac{5.56}{\Delta q}$ [159, 160], we estimate the grain size across samples to be $\sim 0.1 \mu m$ based on the full-width at half-maximum (FWHM) of the principal scattering peak (q^*). It should be noted that this calculation neglects the effects of polycrystallinity, temperature, and strain on the FWHM. Therefore, the grain size is likely underestimated in our calculation. Nonetheless, this calculation allows us to estimate that the membranes have on the order of 100 grains across the thickness of the membrane. In polymer blends containing ion-conducting domains, Irwin and others [157] showed that two out of three grain boundary orientations in lamellar structures are effective for ion diffusion, while just one out of three cylinder orientations in hexagonal structures is efficient. As such, the lower fluxes observed for the hexagonal mesophases over their lamellar counterparts can be rationalized by the higher probability of dead-ends at grain boundaries in hexagonal mesophases. Further, these results suggest that increasing the grain size

relative to the membrane thickness, which can be accomplished via shear, thermal annealing, or mere reduction of the membrane thickness, could improve the permeability of our membranes even further.

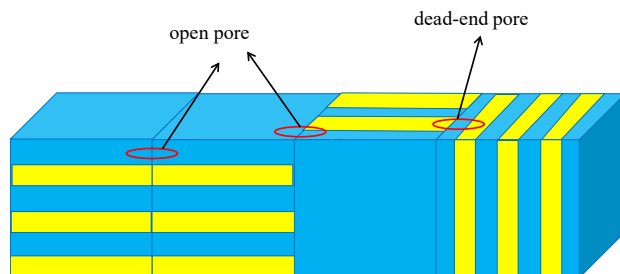


Figure 5-4. Schematic representation of grain boundaries that can lead to open or dead-end pores.

To evaluate membrane separation performance, dead-end stirred cell filtration is performed with a 1 mg/mL BSA and direct red 23 (DR23) dye as feed solutions. UV-Vis results for the feed and permeate of commercial, lamellar (I), and hexagonal (III) membranes with a BSA feed solution are shown in Figure I-5a (Appendix I). A calibration curve for absorbance as a function of BSA concentration, shown in Figure I-5b (Appendix I) is determined and used to calculate the concentration of BSA in each stream [161]. The minimum detectable concentration of BSA through this method is 0.05 mg/mL. It can be seen that neither I or III permeates display a noticeable peak at 280 nm. As a result, it can be concluded that BSA concentration in the permeates of these two membranes is less than 0.05 mg/mL. Therefore, BSA rejection for both lamellar and hexagonal membranes is greater than 95%. In contrast, the commercial NIPS membrane only displayed 68% BSA rejection.

DR23 has a characteristic peak at 507 nm and UV-Vis is a good method to measure its concentration in solvents. Results show our membranes reject more than 99% of dye, while commercial membrane's rejection was only 90%. Figure I-6 in Appendix I, shows the photographs of feed and permeates, where superior performance of as-synthesized membranes is obvious.

Additionally, the fouling resistance of lamellar (I) and hexagonal (III) membranes is measured and compared with the commercial membrane. Macromolecules and proteins are two of the primary foulants encountered in water filtration. As such, we used 1 mg/mL BSA and 1 mg/mL PEG300 solutions in DI water as foulants. Flux decline curves are shown in Figure 5-5. Our results show that the flux declines slightly (only 6%) over 12 h for lamellar and hexagonal membranes, while there is a significant flux decline (89%) observed for the commercial membrane. These results indicate that, despite their small pore size (< 5 nm), our membranes

display a superior fouling resistance (even in a dead-end configuration) when compared to a conventional NIPS UF membrane. We attribute this improvement to the consistent pore structure throughout our membranes as well as the hydrophilicity of the Pluronic PEO blocks decorating them, which is in stark contrast to the anisotropic structure of NIPS membranes. This anisotropy as well as the low surface porosity of NIPS membranes results in reduced fouling resistance. The fouling resistance of our membranes is further enhanced by the hydrophilicity of the pore surfaces, due to retained Pluronic chains. Additionally, the similarity between the flux decay profiles for both BSA and PEG300 is striking considering BSA was found to be completely rejected, while the PEG300 was found to pass through the membrane (as will be discussed). This can be attributed in part to the high stirring rate used during these experiments, which prevented a substantial over-layer of BSA from forming. However, the stark contrast between our membranes and the commercial membrane suggests, as noted above, that the high fouling resistance of our membrane also contributed. As can be seen in Figure 5-5, the flux for BSA is higher than that of PEG300. This is due to the size and shape of the solute molecules.

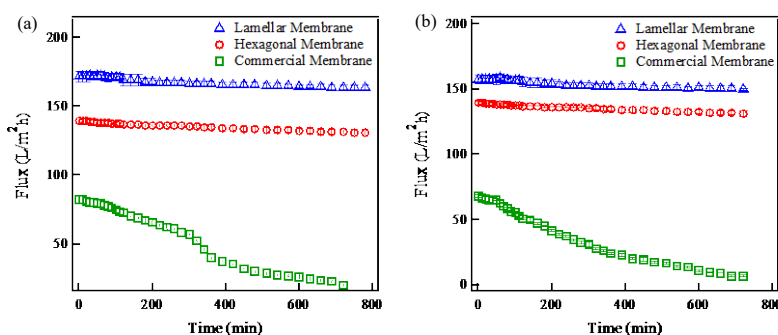


Figure 5-5. Filtration of (a) 1 mg/mL BSA and (b) 1 mg/mL PEG300 solutions through lamellar (I), hexagonal (III), and commercial membranes. Error bars indicate the standard deviation of three measurements.

Figure 5-6 shows the MWCO graphs for lamellar and hexagonal membranes. In both cases, the rejection values for $M_w=1500$ g/mol are greater than 89.5%, thus, the MWCO is ~ 1500 g/mol. PEG Stokes radius, a_{Stokes} (nm), can be calculated as follows [162]:

$$a_{\text{Stokes}} = 16.73 \times 10^{-10} M_w^{0.557} \quad (5-10)$$

where M_w is the molecular weight of PEG. For $M_w=1500$ g/mol, PEG diameter is 1.96 nm, which is close to the pore size of the membranes calculated in Table 5-2. This suggests that, as we assumed in our calculations, the block copolymer is retained in the pores. The modest

difference between the calculated pore size and the separable solute size can be attributed in part to the assumption in our calculations that the phases were completely segregated.

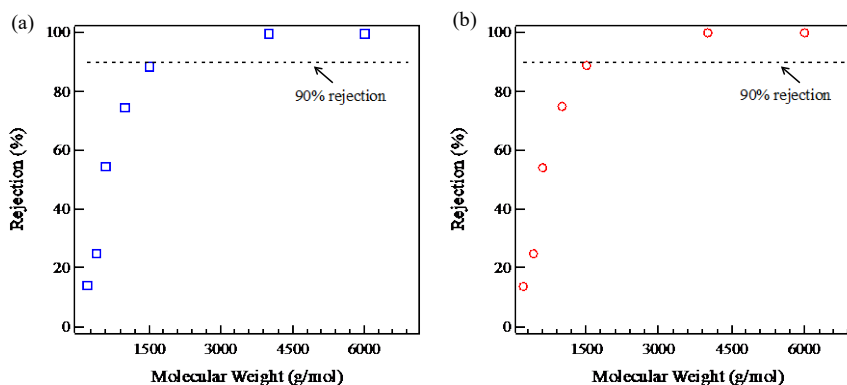


Figure 5-6. MWCO curve for as-synthesized membranes using TOC method, (a) lamellar membrane (sample I), (b) hexagonal membrane (sample III).

5.4 Using functional monomers for making antibacterial membranes

In the previous sections, we have shown that self-assembled block copolymers can be used as templates to produce UF membranes with improved permeability over conventional ones [42]. In addition, the methodology provides a more eco-friendly alternative to current membrane fabrication methods, which require organic solvents [10]. Concentration polarization and bio-fouling are two critical problems found in membrane filtration systems [163]. Bio-fouling is a consequence of the presence of proteins, bacteria, and viruses in water and wastewater sources [163]. Currently, chlorination is utilized in municipal water systems to remove tiny microorganisms and bacteria [163]. However, harmful disinfection byproducts produced during the chlorination process have raised concerns and motivated exploration of other disinfection agents [164]. Therefore, if combined with disinfection, ultrafiltration and microfiltration can transform not only the municipal water treatment, but also the treatment of wastewater containing harmful microorganisms and bacteria due to their high flux rate and efficiency. In recent years, antibacterial membranes have made their way to industry for the removal of bacteria and microorganisms from water [165, 166]. Conventionally, antibacterial membranes are prepared through surface modification, but most surface modification routes are limited to specific types of membranes. Furthermore, these routes require the use of complex and often expensive chemical reactions to graft antibacterial groups onto the surface, making the final

product costly. We are proposing in-situ synthesis of antibacterial UF and MF membranes from functionalized monomers via templates of self-assembled block copolymers.

Different studies have shown that quaternary ammonium groups, like trimethylammonium chloride, are successful in killing bacteria such as *Escherichia coli* (*E. coli*) [167]. Presence of quaternary ammonium groups on the surface and in the bulk has been shown to make final membranes antibacterial [168]. Figure 5-7 schematically shows the antibacterial membranes produced through the templating approach. Self-assembly of Pluronic block copolymers with different block ratios in the presence of [2-(acryloyloxy) ethyl] trimethylammonium chloride or (3-acrylamidopropyl) trimethylammonium chloride (APAC) and a crosslinker will yield different mesostructures with different channel sizes, which will then be cast as thin films on a support and polymerized (as discussed in Section 5.2.4) to produce antibacterial membranes.

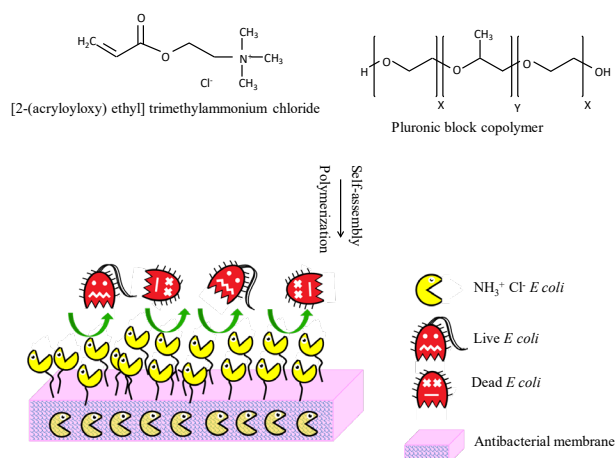


Figure 5-7. Schematic illustration of antibacterial membranes made through self-assembly using a functional monomer.

5.4.1 Materials and formulation design

Pluronic L64 is used as the surfactant. DI water is used as the aqueous phase. [2-(acryloyloxy) ethyl] trimethylammonium chloride (AEAC, 80 wt.% solution in water, Sigma-Aldrich) is used as a hydrophilic monomer. Diallylamine (DMA, 99%, Sigma-Aldrich), ethylene glycol dimethacrylate (EGDMA, purified, Electron Microscopy Sciences), and poly(ethylene glycol)-diacrylate (PEGDA, $M_n=250$ g/mol, Sigma-Aldrich) are used as three potential crosslinkers. Potassium persulfate (KPS, Fisher Scientific) is used as the thermal initiator. In some samples, an oil phase is added to increase the mechanical properties of the

membranes. Specifically, butyl acrylate (99%, Sigma-Aldrich) is used as the hydrophobic monomer and EGDMA is used as a crosslinker in the oil phase.

Six different compositions, shown in Table 5-4, are chosen based on the lamellar regions of a similar phase diagram developed by Alexandridis and others [116].

Table 5-4. Composition of the samples used for the synthesis of antibacterial membranes.

Membrane	Composition (wt%) ^{a,b}	Aqueous phase crosslinker ^c	Oil phase ^d
HD1	L64/Water (50/50)	DMA	NA
HD2	L64/Water (50/50)	PEGDA	NA
HD3	L64/Water (50/50)	EGDMA	NA
HD4	L64/Water/Oil (50/35/15)	DMA	BA+EGDMA
HD5	L64/Water/Oil (50/35/15)	PEGDA	BA+EGDMA
HD6	L64/Water/Oil (50/35/15)	EGDMA	BA+EGDMA

^a 50wt% AEAC is used as the monomer in the aqueous phase.

^b KPS (5 wt% of the AEAC) is used as the initiator in all samples.

^c 50 wt% of the aqueous phase monomer.

^d Oil phase consist of BA and EGDMA (33wt% of the BA) in all samples.

After making the mesophases, we keep them in a refrigerator for a few days to make sure they are in equilibrium. We realized that membranes HD2 and HD5 are polymerized without applying any heat. Apparently, the presence of PEGDA in both samples stimulates the polymerization reaction to occur even at very low temperatures (~5 °C). We use a microfiltration membrane (Millipore, EIMF22205) as the support for membranes.

5.4.2 SAXS analysis

SAXS results for samples HD1, HD3, and HD4 are presented in Appendix I. Table 5-5 shows the calculated SAXS parameters and estimated pore sizes for membranes made with samples HD1, HD3, and HD4.

Table 5-5. Calculated parameters for lamellar and hexagonal mesophases before polymerization (BP) and after polymerization (AP).

Sample	Structure	ϕ	d or a (nm)		δ or R (nm)		φ_{water}	Pore size (nm)
			BP	AP	BP	AP		
HD1	Lamellar	0.55	6.9	7.3	3.8	4.0	0.26	1.9
HD3	Lamellar	0.54	7.4	7.5	4.0	4.1	0.26	2.0
HD4	Hexagonal	0.45	9.3	9.5	3.2	3.3	0.36	3.0

5.4.3 Membrane performance

Membranes are made by coating the mesophases on a support layer as explained in Section 5.2.4. Permeability of the membranes is shown in Table 5-6. It can be seen that all as-synthesized membranes have a lower flow rate compared to the support, which was expected. The permeability has a direct relationship with the pore size and also the shape of the pores as explained in the previous sections.

Table 5-6. Flow rate, normalized permeability, and BSA rejection of as-synthesized lamellar membranes compared to commercial one.

Parameter	Support	Membrane HD1	Membrane HD3	Membrane HD4	Membrane HD5
Q_m (L/h)	0.31±0.01	0.24±0.01	0.27±0.02	0.25±0.03	0.26±0.01
κ/l (10^{-13} L/m ²)	3.93±0.01	3.0±0.01	3.42±0.01	3.17±0.01	3.30±0.01
BSA rejection (%)	<60%	>95%	>95%	>95%	>95%

BSA is used as solute for the rejection test. As shown in Table 5-5, rejection values for the as-synthesized membranes are exceptional and higher than that of the support.

5.4.4 Antibacterial properties of the membranes

To test the antibacterial properties of the samples, we use the *E. coli* Count test using 3M PetriFilm *E. coli* counter. To prepare the samples, as-synthesized membranes are kept in contact with the water sample (containing *E. coli*) for one hour. Then, a drop of water sample is transferred to the middle of Petrifilms. The control sample is the water sample without any

contact with membranes. Different dilutions of water are used as shown in Figure I-10 (see Appendix I).

All Petrifilm samples are kept in an incubator at 35°C for 48 hours. In order to inoculate the Petrifilms, several steps are followed precisely: (1) the Petrifilm plate is placed on a level surface; (2) the top film is lifted; (3) the sample is measured using a micropipette, and with the pipette perpendicular to Petrifilm plate, 1 or 0.1 ml of sample is placed onto the center of the bottom film; (4) the top film is carefully rolled down to avoid trapping air bubbles; (5) with flat side down, a spreader is placed on the top film over inoculum; (6) pressure is applied gently on the spreader to distribute it over circular area; (7) the spreader is lifted and the gel is given at least one minute to solidify; and (8) plates are incubated with clear side up.

After 48 h of incubation, we need to count the number of colonies in each Petrifilm using a standard colony counter. Table 5-6 shows the number of colonies in each sample.

Table 5-7. Number of the colonies in each sample after 48 h of incubation.

Sample	# of colonies
1:1 (control)	560
1:10 (control)	310
1:1000 (control)	100
1:10,000 (control)	30
1:100,000 (control)	2
1:1 (membrane HD1)	2
1:10 (membrane HD1)	0
1:100 (membrane HD1)	0
1:1000 (membrane HD1)	0
1:10,000 (membrane HD1)	0
1:100,000 (membrane HD1)	0

Typical digital images of the Petrifilms after incubation are shown in Figure 5-8, where we can see almost no growth of bacteria colonies on the samples that were in contact with as-synthesized membranes.

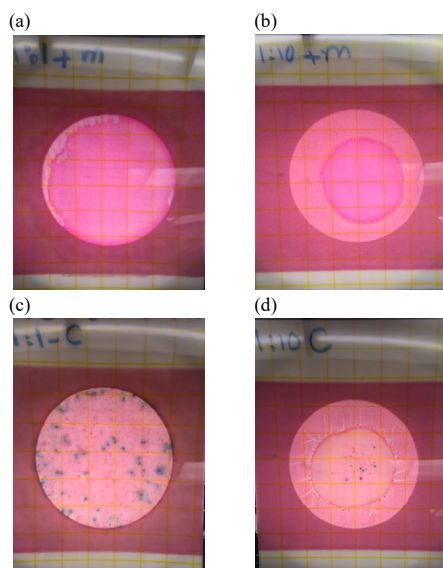


Figure 5-8. Typical digital images of the Petrifilms after 48 hr of incubation. (a) 1:1 dilution and in contact with membrane, (b) 1:10 dilution and in contact with membrane, (c) 1:1 dilution of control sample, (d) 1:10 dilution of control sample.

These preliminary results show that the *E. coli* bacteria do not survive in the water sample next to as-synthesized membranes, and no colony growth is observed.

5.5 Conclusion

Self-assembled mesostructures of a surfactant in the presence of water and oil have been used as templates for the production of UF membranes without the need for organic solvent. Cross-polarized light microscopy and SAXS confirm the retention of hexagonal and lamellar mesophases after polymerization for most samples, with only a modest transition from a HM/HPL to a hexagonal morphology observed for samples with Pluronic/water/oil 60/15/25 composition. As-synthesized membranes were found to have excellent permeability with operational permeabilities double that of a commercial NIPS UF membrane. Additionally, the membranes exhibited MWCO of 1500 g/mol with exceptional rejection performance, namely >95% of BSA and >99% of DR23 in a 1 mg/mL feed. Notably, the flux decline observed for both lamellar and hexagonal membranes with 1 mg/mL BSA and PEG300 solutions over 12 h is minimal, indicating substantial fouling resistance. Consequently, it can be concluded that membranes produced via our approach significantly outperform the commercial NIPS UF

membrane used in this study. As such, these results confirm that mesophase-templated membranes could provide an eco-friendly and more effective alternative to conventional NIPS UF membranes.

A series of antibacterial membranes have been made using AEAC as a functional monomer. Our preliminary results show that as-synthesized membranes have an exceptional BSA rejection of >95%. Antibacterial properties of the membranes were evaluated using the *E. coli* Count test, and our results prove that no bacterial colony can grow in the presence of quaternary ammonium groups. More tests are expected to be done on flux retention and antibacterial performance of the membranes as part of planned future work (see below in the concluding section).

Chapter 6: Conclusions and Future Work

6.1 Summary

Self-assembly of amphiphilic block copolymers in oil/water mixture provides a flexible system to design different types of structures at a constant temperature and even at a constant block copolymer ratio. Self-assembled structures of interest for this specific research are micellar cubic, lamellar, normal, and reverse hexagonal systems, also known as mesophases.

This report provides a comprehensive study on the rheological behavior of such systems. Flow behavior of lamellar and hexagonal mesophases indicates that they have yield stress. Oscillatory shear experiments show that mesophases have solid-like behavior and exhibit type III non-linear behavior. The elastic moduli of mesophases is controlled by the van der Waals interaction between micelles. We suggest that at relatively low frequencies, defects control the rheological behavior of LLCs, while at high frequencies the contributions in micellar scale are dominant. Applying high strains on the LLCs induces two relaxation times after cessation of flow, decreases the elastic modulus in the whole frequency range, and decreases the loss modulus in the low frequency regime with negligible effect at high frequencies. The decrease in moduli is reversible and the system relaxes back to its original elastic modulus at rest. The observed behavior can be attributed to the elimination of defects under high strains and their re-formation during long enough rest times.

Chemorheology is used to describe the kinetics of thermal polymerization in nanoconfined domains of LLC templates at different temperatures. We investigated lamellar and reverse hexagonal LLC phases with the same concentration of monomeric phase. Results showed that the mesophase structures remain intact during thermal polymerization with very slight changes in the domain size. The polymerization rate decreases in the nanoconfined structure compared to the bulk state due to the segregation effect that increases the local monomer concentration and enhances the termination rate. Additionally, the polymerization rate is faster in the studied reverse hexagonal systems compared to the lamellar ones due to their lower degree of confinement. A higher degree of confinement also induces a lower monomer conversion. Differential scanning calorimetry confirms the obtained results from chemorheology.

We present the self-assembly of Pluronic block copolymers in the presence of water and a monomeric phase as a new technique for the preparation of UF membranes without the need for organic solvent or post-modification. Different compositions of block copolymer, water, and monomer were polymerized to obtain both hexagonal and lamellar mesostructures, as indicated by SAXS and cross-polarized light microscopy. As-synthesized membranes were found to have molecular weight cutoff of 1500 g/mol, pore sizes in the range of 3-4 nm, and to exhibit both excellent fouling resistance and high permeance of water, vastly outperforming a conventional

NIPS UF membrane. Further, in contrast to NIPS, the proposed method provides flexibility in terms of both the final membrane chemistry and pore size. As such, it is a versatile approach that can be easily tailored to produce membranes for a wide range of applications including wastewater treatment and food processing. Antibacterial membranes are made using a functional monomer containing quaternary ammonium. The results show that as-synthesized membrane has an exceptional BSA rejection of >95%. Antibacterial properties of the membranes are evaluated using the *E. coli* Count test. Our result proves that no bacterial colony can grow in the presence of quaternary ammonium groups.

6.2 Future work

While significant progress was made in this study toward understanding the viscoelastic properties of mesophases, flow curve behavior of mesophases, the effect of confinement on the polymerization kinetics, and the design criteria for incorporating a templating approach for making a mesoporous polymer without changing the structure of the initial template, some questions remain unanswered.

Specifically, the impact of shear and oscillation flow fields on the structure of lamellar and micellar cubic phases could provide helpful information for designing the unit operation and processability of mesophases for making mesoporous polymers for different applications. Additionally, velocimetry techniques for confirming the observed probable shear banding in mesophases would be beneficial.

Different types of polymerization reactions such as reversible addition-fragmentation chain-transfer (RAFT) in mesophases can be used to synthesize polymers or block copolymers with controllable chain length and molecular weight in the nanoconfinement scale for advanced functional materials.

Finally, additional experiments should be done on antibacterial membranes to characterize them in term of flux retention, antifouling properties, and antibacterial performance.

Detailed procedures suggested as future works are presented in Appendix J.

References

- [1] Progress on Drinking Water, Sanitation and Hygiene: 2017 Update and MDG Assessment, Geneva:, 2017.
- [2] A.D. Khawaji, I.K. Kutubkhanah, J.-M. Wie, Advances in Seawater Desalination Technologies, Desalination. 221 (2008) 47–69. doi:10.1016/J.DESAL.2007.01.067.
- [3] J. Andrianne, F. Alardin, Thermal and Membrane Processes Economics: Optimized Selection for Seawater Desalination, Desalination. 153 (2003) 305–311. doi:10.1016/S0011-9164(02)01128-1.
- [4] A.B. Hinchliffe, K.E. Porter, A Comparison of Membrane Separation and Distillation, Chem. Eng. Res. Des. 78 (2000) 255–268. doi:10.1205/026387600527121.
- [5] I. Sadeghi, P. Kaner, A. Asatekin, Controlling and Expanding the Selectivity of Filtration Membranes, Chem. Mater. 30 (2018) 7328–7354. doi:10.1021/acs.chemmater.8b03334.
- [6] R.W. Baker, Membrane technology and applications, 2nd ed., John Wiley & Sons, Ltd, Chichester, UK, 2004. doi:10.1002/9781118359686.
- [7] J.T. Jung, J.F. Kim, H.H. Wang, E. di Nicolo, E. Drioli, Y.M. Lee, Understanding the Non-Solvent Induced Phase Separation (NIPS) Effect During the Fabrication of Microporous PVDF Membranes via Thermally Induced Phase Separation (TIPS), J. Memb. Sci. 514 (2016) 250–263. doi:10.1016/J.MEMSCI.2016.04.069.
- [8] A. Basile, A. Cassano, N.K. Rastogi, Advances in Membrane Technologies for Water Treatment : Materials, Processes and Applications, Woodhead Publishing, 2015. doi:10.1016/C2013-0-16469-0.
- [9] H.H. Wang, J.T. Jung, J.F. Kim, S. Kim, E. Drioli, Y.M. Lee, A Novel Green Solvent Alternative for Polymeric Membrane Preparation via Nonsolvent-Induced Phase Separation (NIPS), J. Memb. Sci. 574 (2019) 44–54. doi:10.1016/J.MEMSCI.2018.12.051.
- [10] G.R. Guillen, Y. Pan, M. Li, E.M. V Hoek, Preparation and Characterization of Membranes Formed by Nonsolvent Induced Phase Separation: A Review, Ind. Eng. Chem. Res. 50 (2011) 3798–3817. doi:10.1021/ie101928r.
- [11] N. Nady, M.C.R. Franssen, H. Zuilhof, M.S.M. Eldin, R. Boom, K. Schroën, Modification Methods for Poly(Arylsulfone) Membranes: A Mini-Review Focusing on Surface Modification, Desalination. 275 (2011) 1–9. doi:10.1016/j.desal.2011.03.010.
- [12] A. Asatekin, S. Kang, M. Elimelech, A.M. Mayes, Anti-Fouling Ultrafiltration Membranes Containing Polyacrylonitrile-graft-Poly(Ethylene Oxide) Comb Copolymer Additives, J. Memb. Sci. 298 (2007) 136–146. doi:10.1016/J.MEMSCI.2007.04.011.
- [13] A.D. Marshall, P.A. Munro, G. Tragardh, The Effect of Protein Fouling in Microfiltration and Ultrafiltration on Permeate Flux, Protein Retention and Selectivity: A Literature Review, Desalination. 91 (1993) 65–108. doi:10.1016/0011-9164(93)80047-Q.

- [14] C.-C. Ho, A.L. Zydney, Effect of Membrane Morphology on the Initial Rate of Protein Fouling during Microfiltration, *J. Memb. Sci.* 155 (1999) 261–275. doi:10.1016/S0376-7388(98)00324-X.
- [15] A. Figoli, T. Marino, S. Simone, E. Di Nicolò, X.-M. Li, T. He, S. Tornaghi, E. Drioli, Towards Non-Toxic Solvents for Membrane Preparation: a Review, *Green Chem.* 16 (2014) 4034. doi:10.1039/C4GC00613E.
- [16] M.S. Reisch, Solvent Users Look To Replace NMP, *Chem. Eng. News.* (2008) 32.
- [17] Z. Cui, N.T. Hassankiadeh, S.Y. Lee, K.T. Woo, J.M. Lee, A. Sanguineti, V. Arcella, Y.M. Lee, E. Drioli, Tailoring Novel Fibrillar Morphologies in Poly(Vinylidene Fluoride) Membranes Using a Low Toxic Triethylene Glycol Diacetate (TEGDA) Diluent, *J. Memb. Sci.* 473 (2015) 128–136. doi:10.1016/J.MEMSCI.2014.09.019.
- [18] B.J. Cha, J.M. Yang, Preparation of Poly(Vinylidene Fluoride) Hollow Fiber Membranes for Microfiltration Using Modified TIPS Process, *J. Memb. Sci.* 291 (2007) 191–198. doi:10.1016/J.MEMSCI.2007.01.008.
- [19] M. Zhang, B. Liao, X. Zhou, Y. He, H. Hong, H. Lin, J. Chen, Effects of Hydrophilicity/Hydrophobicity of Membrane on Membrane Fouling in a Submerged Membrane Bioreactor, *Bioresour. Technol.* 175 (2015) 59–67. doi:10.1016/J.BIORTECH.2014.10.058.
- [20] W. Sun, J. Liu, H. Chu, B. Dong, Pretreatment and Membrane Hydrophilic Modification to Reduce Membrane Fouling., *Membranes (Basel).* 3 (2013) 226–241. doi:10.3390/membranes3030226.
- [21] E.M. Vrijenhoek, S. Hong, M. Elimelech, Influence of Membrane Surface Properties on Initial Rate of Colloidal Fouling of Reverse Osmosis and Nanofiltration Membranes, *J. Memb. Sci.* 188 (2001) 115–128. doi:10.1016/S0376-7388(01)00376-3.
- [22] D. Rana, T. Matsuura, Surface Modifications for Antifouling Membranes, *Chem. Rev.* 110 (2010) 2448–2471. doi:10.1021/cr800208y.
- [23] H. Ma, C.N. Bowman, R.H. Davis, Membrane Fouling Reduction by Backpulsing and Surface Modification, *J. Memb. Sci.* 173 (2000) 191–200. doi:10.1016/S0376-7388(00)00360-4.
- [24] H. Lee, G. Amy, J. Cho, Y. Yoon, S.-H. Moon, I.S. Kim, Cleaning Strategies for Flux Recovery of an Ultrafiltration Membrane Fouled by Natural Organic Matter, *Water Res.* 35 (2001) 3301–3308. doi:10.1016/S0043-1354(01)00063-X.
- [25] S. Akhtar, C. Hawes, L. Dudley, I. Reed, P. Stratford, Coatings Reduce the Fouling of Microfiltration Membranes, *J. Memb. Sci.* 107 (1995) 209–218. doi:10.1016/0376-7388(95)00118-9.
- [26] W. Dai, T.. Barbari, Hydrogel Membranes with Mesh Size Asymmetry Based on the Gradient Crosslinking of Poly(Vinyl Alcohol), *J. Memb. Sci.* 156 (1999) 67–79. doi:10.1016/S0376-7388(98)00330-5.
- [27] H.-Y. Yu, Y.-J. Xie, M.-X. Hu, J.-L. Wang, S.-Y. Wang, Z.-K. Xu, Surface Modification of

- Polypropylene Microporous Membrane to Improve its Antifouling Property in MBR: CO₂ Plasma Treatment, *J. Memb. Sci.* 254 (2005) 219–227. doi:10.1016/J.MEMSCI.2005.01.010.
- [28] J. Pieracci, J. V. Crivello, G. Belfort, UV-Assisted Graft Polymerization of N-Vinyl-2-pyrrolidinone onto Poly(ether sulfone) Ultrafiltration Membranes Using Selective UV Wavelengths, *Chem. Mater.* 14 (2001) 256–265. doi:10.1021/CM010565+.
- [29] Y. Li, S. Huang, S. Zhou, A.G. Fane, Y. Zhang, S. Zhao, Enhancing Water Permeability and Fouling Resistance of Polyvinylidene Fluoride Membranes with Carboxylated Nanodiamonds, *J. Memb. Sci.* 556 (2018) 154–163. doi:10.1016/J.MEMSCI.2018.04.004.
- [30] P. Bengani, Y. Kou, A. Asatekin, Zwitterionic copolymer self-assembly for fouling resistant, high flux membranes with size-based small molecule selectivity, *J. Memb. Sci.* 493 (2015) 755–765. doi:10.1016/j.memsci.2015.07.025.
- [31] Y. Zhang, J.L. Sargent, B.W. Boudouris, W.A. Phillip, Nanoporous Membranes Generated from Self-Assembled Block Polymer Precursors: Quo Vadis ?, *J. Appl. Polym. Sci.* 132 (2015) 41683(1–17). doi:10.1002/app.41683.
- [32] E.S. Hatakeyama, C.J. Gabriel, B.R. Wiesenauer, J.L. Lohr, M. Zhou, R.D. Noble, D.L. Gin, Water filtration performance of a lyotropic liquid crystal polymer membrane with uniform, sub-1-nm pores, *J. Memb. Sci.* 366 (2011) 62–72. doi:10.1016/j.memsci.2010.09.028.
- [33] E.S. Hatakeyama, B.R. Wiesenauer, C.J. Gabriel, R.D. Noble, D.L. Gin, Nanoporous, Bicontinuous Cubic Lyotropic Liquid Crystal Networks via Polymerizable Gemini Ammonium Surfactants, *Chem. Mater.* 22 (2010) 4525–4527. doi:10.1021/cm1013027.
- [34] B.M. Carter, B.R. Wiesenauer, E.S. Hatakeyama, J.L. Barton, R.D. Noble, D.L. Gin, Glycerol-Based Bicontinuous Cubic Lyotropic Liquid Crystal Monomer System for the Fabrication of Thin-Film Membranes with Uniform Nanopores, *Chem. Mater.* 24 (2012) 4005–4007. doi:10.1021/cm302027s.
- [35] M. Zhou, T.J. Kidd, R.D. Noble, D.L. Gin, Supported Lyotropic Liquid-Crystal Polymer Membranes: Promising Materials for Molecular-Size-Selective Aqueous Nanofiltration, *Adv. Mater.* 17 (2005) 1850–1853. doi:10.1002/adma.200500444.
- [36] M. Zhou, P.R. Nemade, X. Lu, X. Zeng, E.S. Hatakeyama, R.D. Noble, D.L. Gin, New type of membrane material for water desalination based on a cross-linked bicontinuous cubic lyotropic liquid crystal assembly, *J. Am. Chem. Soc.* 129 (2007) 9574–9575. doi:10.1021/ja073067w.
- [37] G. Odian, *Principles of polymerization*, 2004.
- [38] T.P. Lodge, Block copolymers: Past successes and future challenges, *Macromol. Chem. Phys.* 204 (2003) 265–273. doi:10.1002/macp.200290073.
- [39] G.H. Fredrickson, F.S. Bates, Dynamics of Block Copolymers: Theory and Experiment, *Annu. Rev. Mater. Sci.* 26 (1996) 501–550. doi:10.1146/annurev.ms.26.080196.002441.
- [40] E.W. Cochran, C.J. Garcia-Cervera, G.H. Fredrickson, Stability of the Gyroid Phase in Diblock

- Copolymers at Strong Segregation, *Macromolecules*. 39 (2449) 2449–2451.
doi:10.1021/ma0527707.
- [41] Z. Chen, T.L. Greaves, C. Fong, R.A. Caruso, C.J. Drummond, Lyotropic Liquid Crystalline Phase Behaviour in Amphiphile–Protic Ionic Liquid Systems, *Phys. Chem. Chem. Phys.* 14 (2012) 3825–3836. doi:10.1039/c2cp23698b.
- [42] S. Qavi, A. Lindsay, M. Firestone, R. Foudazi, Ultrafiltration membranes from polymerization of self-assembled Pluronic block copolymer mesophases, *J. Memb. Sci.* 580 (2019) 125–133. doi:10.1016/j.memsci.2019.02.060.
- [43] P. Alexandridis, U. Olsson, B. Lindman, A Record Nine Different Phases (Four Cubic, Two Hexagonal, and One Lamellar Lyotropic Liquid Crystalline and Two Micellar Solutions) in a Ternary Isothermal System of an Amphiphilic Block Copolymer and Selective Solvents (Water and Oil), *Langmuir*. 14 (1998) 2627–2638. doi:10.1021/la971117c.
- [44] P. Holmqvist, P. Alexandridis, B. Lindman, Modification of the Microstructure in Block Copolymer–Water–“Oil” Systems by Varying the Copolymer Composition and the “Oil” Type: Small-Angle X-ray Scattering and Deuterium-NMR Investigation, *J. Phys. Chem. B*. 102 (1998) 1149–1158. doi:10.1021/jp9730297.
- [45] P. Holmqvist, P. Alexandridis, B. Lindman, Phase Behavior and Structure of Ternary Amphiphilic Block Copolymer–Alkanol–Water Systems: Comparison of Poly(ethylene oxide)/Poly(propylene oxide) to Poly(ethylene oxide)/Poly(tetrahydrofuran) Copolymers, *Langmuir*. 13 (1997) 2471–2479. doi:10.1021/la960819j.
- [46] L. Sievens-Figueroa, C.A. Guymon, Cross-Linking of Reactive Lyotropic Liquid Crystals for Nanostructure Retention, *Chem. Mater.* 21 (2009) 1060–1068. doi:10.1021/cm803383d.
- [47] D.T. McCormick, K.D. Stovall, C.A. Guymon, Photopolymerization in pluronic lyotropic liquid crystals: Induced mesophase thermal stability, *Macromolecules*. 36 (2003) 6549–6558. doi:10.1021/ma030037e.
- [48] M.A. DePierro, K.G. Carpenter, C.A. Guymon, Influence of Polymerization Conditions on Nanostructure and Properties of Polyacrylamide Hydrogels Templated from Lyotropic Liquid Crystals, *Chem. Mater.* 18 (2006) 5609–5617. doi:10.1021/cm061969a.
- [49] S.A. Jenekhe, X.L. Chen, Self-assembled aggregates of rod-coil block copolymers and their solubilization and encapsulation of fullerenes, *Science*. 279 (1998) 1903–1907. doi:10.1126/SCIENCE.279.5358.1903.
- [50] S.C. Warren, L.C. Messina, L.S. Slaughter, M. Kamperman, Q. Zhou, S.M. Gruner, F.J. DiSalvo, U. Wiesner, Ordered mesoporous materials from metal nanoparticle-block copolymer self-assembly., *Science*. 320 (2008) 1748–52. doi:10.1126/science.1159950.
- [51] Z. Nie, D. Fava, E. Kumacheva, S. Zou, G.C. Walker, M. Rubinstein, Self-assembly of metal–polymer analogues of amphiphilic triblock copolymers, *Nat. Mater.* 6 (2007) 609–614. doi:10.1038/nmat1954.

- [52] X. Feng, M.E. Tousley, M.G. Cowan, B.R. Wiesenauer, S. Nejati, Y. Choo, R.D. Noble, M. Elimelech, D.L. Gin, C.O. Osuji, Scalable fabrication of polymer membranes with vertically aligned 1 nm pores by magnetic field directed self-Assembly, *ACS Nano*. 8 (2014) 11977–11986. doi:10.1021/nn505037b.
- [53] H.-P. Hentze, E.W. Kaler, Polymerization of and within self-organized media, *Curr. Opin. Colloid Interface Sci.* 8 (2003) 164–178. doi:10.1016/S1359-0294(03)00018-9.
- [54] F. Kleitz, T. Czuryzkiewicz, A. Leonid A. Solovyov, M. Lindén, X-ray Structural Modeling and Gas Adsorption Analysis of Cagelike SBA-16 Silica Mesophases Prepared in a F127/Butanol/H₂O System, *Chem. Mater.* 18 (2006) 5070–5079. doi:10.1021/CM061534N.
- [55] F. Kleitz, A. Tae-Wan Kim, R. Ryoo, Phase Domain of the Cubic Im $\bar{3}m$ Mesoporous Silica in the EO106PO70EO106–Butanol–H₂O System, *Langmuir*. 22 (2005) 440–445. doi:10.1021/LA052047+.
- [56] L. Yang, P. Alexandridis, Physicochemical aspects of drug delivery and release from polymer-based colloids, *Curr. Opin. Colloid Interface Sci.* 5 (2000) 132–143. doi:10.1016/S1359-0294(00)00046-7.
- [57] O. Parisi, L. Scrivano, S. Candamano, M. Ruffo, A. Vattimo, M. Spanedda, F. Puoci, Molecularly Imprinted Microrods via Mesophase Polymerization, *Molecules*. 23 (2017) 63. doi:10.3390/molecules23010063.
- [58] N.A. Gujarathi, B.R. Rane, R.K. Keservani, Liquid Crystal Systems in Drug Delivery, in: *Nov. Approaches Drug Deliv.*, Medicin Information Science Reference, 2017: pp. 190–216.
- [59] S. Hocine, M.-H. Li, Thermoresponsive self-assembled polymer colloids in water, *Soft Matter*. 9 (2013) 5839–5861. doi:10.1039/c3sm50428j.
- [60] P. Alexandridis, B. Lindman, *Amphiphilic block copolymers: self-assembly and applications*, Elsevier, 2000.
- [61] R. Jiaxiang, S.S. Adriana, R. Krishnamoorti, Linear Viscoelasticity of Disordered Polystyrene–Polyisoprene Block Copolymer Based Layered-Silicate Nanocomposites, *Macromolecules*. 33 (2000) 3739–3746. doi:10.1021/ma992091u.
- [62] J.M. Sebastian, C. Lai, W.G. William, A.R. Richard, Steady-Shear Rheology of Block Copolymer Melts and Concentrated Solutions: Disordering Stress in Body-Centered-Cubic Systems, *Macromolecules*. 35 (2002) 2707–2713. doi:10.1021/ma011523+.
- [63] M.B. Kossuth, D.C. Morse, F.S. Bates, Viscoelastic behavior of cubic phases in block copolymer melts, *J. Rheol.* 43 (1998) 167–196. doi:10.1122/1.550981.
- [64] A.K. Gupta, S.N. Purwar, Melt rheological properties of polypropylene/SEBS (styrene–ethylene butylene–styrene block copolymer) blends, *J. Appl. Polym. Sci.* 29 (1984) 1079–1093. doi:10.1002/app.1984.070290406.
- [65] C.I. Chung, J.C. Gale, Newtonian behavior of a styrene–butadiene–styrene block copolymer, *J.*

- Polym. Sci. Polym. Phys. Ed. 14 (1976) 1149–1156. doi:10.1002/pol.1976.180140616.
- [66] C.I. Chung, M.I. Lin, Nature of melt rheological transition in a styrene–butadiene–styrene block copolymer, *J. Polym. Sci. Polym. Phys. Ed.* 16 (1978) 545–553. doi:10.1002/pol.1978.180160316.
- [67] K. Almdal, K.A. Koppi, F.S. Bates, K. Mortensen, Multiple Ordered Phases in a Block Copolymer Melt, *Macromolecules*. 25 (1992) 1743–1751. doi:10.1021/ma00032a019.
- [68] R.G. Larson, *The Structure and Rheology of Complex Fluids*, Oxford University Press: New York, 1999.
- [69] R.H. Colby, Block copolymer dynamics, *Curr. Opin. Colloid Interface Sci.* 1 (1996) 454–465. doi:10.1016/S1359-0294(96)80113-0.
- [70] J. Brassinne, F. Zhuge, C.-A. Fustin, J.-F. Gohy, J. Brassinne, F. Zhuge, C.-A. Fustin, J.-F. Gohy, Precise Control over the Rheological Behavior of Associating Stimuli-Responsive Block Copolymer Gels, *Gels*. 1 (2015) 235–255. doi:10.3390/gels1020235.
- [71] S. V. Ahir, P. G. Petrov, E.M. Terentjev, Rheology at the Phase Transition Boundary: 2. Hexagonal Phase of Triton X100 Surfactant Solution, *Langmuir*. 18 (2002) 9140–9148. doi:10.1021/LA025793C.
- [72] L. Coppola, R. Gianferri, I. Nicotera, C. Oliviero, G.A. Ranieri, Structural changes in CTAB/H₂O mixtures using a rheological approach, *Phys. Chem. Chem. Phys.* 6 (2004) 2364–2372. doi:10.1039/B316621J.
- [73] X. Li, E. Park, K. Hyun, L. Oktavia, M. Kwak, Rheological analysis of core-stabilized Pluronic F127 by semi-interpenetrating network (sIPN) in aqueous solution, *J. Rheol.* 62 (2018) 107–120. doi:10.1122/1.5009202.
- [74] I.W. Hamley, The effect of shear on ordered block copolymer solutions, *Curr. Opin. Colloid Interface Sci.* 5 (2000) 341–349. doi:10.1016/S1359-0294(00)00072-8.
- [75] I.W. Hamley, V. Castelletto, Small-angle scattering of block copolymers: in the melt, solution and crystal states, *Prog. Polym. Sci.* 29 (2004) 909–948. doi:10.1016/j.progpolymsci.2004.06.001.
- [76] N.P. Balsara, B. Hammouda, Shear effects on solvated block copolymer lamellae: Polystyrene-polyisoprene in dioctyl phthalate, *Phys. Rev. Lett.* 72 (1994) 360. doi:10.1103/PhysRevLett.72.360.
- [77] I. Hamley, Concentrated Solutions, in: *Block Copolym. Solut. Fundam. Appl.*, Wiley Online Library, 2012: pp. 105–172.
- [78] S. Liu, L. Li, Multiple phase transition and scaling law for poly(ethylene oxide)-poly(propylene oxide)-poly(ethylene oxide) triblock copolymer in aqueous solution, *ACS Appl. Mater. Interfaces*. 7 (2015) 2688–2697. doi:10.1021/am507749w.
- [79] G. Montalvo, M. Valiente, E. Rodenas, Rheological properties of the L phase and the hexagonal, lamellar, and cubic liquid crystals of the CTAB/benzyl alcohol/water system, *Langmuir*. 12 (1996)

- 5202–5208. doi:10.1021/la9515682.
- [80] C. Rodriguez-Abreu, D.P. Acharya, K. Aramaki, H. Kunieda, Structure and rheology of direct and reverse liquid-crystal phases in a block copolymer/water/oil system, *Colloids Surfaces A Physicochem. Eng. Asp.* 269 (2005) 59–66. doi:10.1016/j.colsurfa.2005.06.061.
- [81] R. Foudazi, S. Qavi, I. Masalova, A.Y. Malkin, Physical chemistry of highly concentrated emulsions, *Adv. Colloid Interface Sci.* 220 (2015) 78–91. doi:10.1016/j.cis.2015.03.002.
- [82] K. Hyun, S.H. Kim, K.H. Ahn, S.J. Lee, Large amplitude oscillatory shear as a way to classify the complex fluids, *J. Nonnewton. Fluid Mech.* 107 (2002) 51–65. doi:10.1016/S0377-0257(02)00141-6.
- [83] M. Mendozza, L. Caselli, C. Montis, S. Orazzini, E. Carretti, P. Baglioni, D. Berti, Inorganic Nanoparticles Modify the Phase Behavior and Viscoelastic Properties of Non-Lamellar Lipid Mesophases, *J. Colloid Interface Sci.* 541 (2019) 329–338. doi:10.1016/J.JCIS.2019.01.091.
- [84] J.-P. Habas, E. Pavie, A. Lapp, J. Peyrelasse, Non-linear viscoelastic properties of ordered phases of a poly(ethylene oxide)-poly(propylene oxide) triblock copolymer, *Rheol. Acta.* 47 (2008) 765–776. doi:10.1007/s00397-008-0293-0.
- [85] J. Zipfel, J. Berghausen, G. Schmidt, P. Lindner, P. Alexandridis, M. Tsianou, W. Richtering, Shear induced structures in lamellar phases of amphiphilic block copolymers, *Phys. Chem. Chem. Phys.* 1 (1999) 3905–3910. doi:10.1039/A904014E.
- [86] J. Zipfel, J. Berghausen, G. Schmidt, P. Lindner, P. Alexandridis, W. Richtering, Influence of shear on solvated amphiphilic block copolymers with lamellar morphology, *Macromolecules.* 35 (2002) 4064–4074. doi:10.1021/ma0116912.
- [87] Y.R. Sliozberg, J.W. Andzelm, J.K. Brennan, M.R. Vanlandingham, V. Pryamitsyn, V. Ganesan, Modeling Viscoelastic Properties of Triblock Copolymers: A DPD Simulation Study, *J. Polym. Sci. Part B Polym. Phys.* 48 (2010) 15–25. doi:10.1002/polb.21839.
- [88] K. Van Workum, J.J. de Pablo, Local elastic constants in thin films of an fcc crystal, *Phys. Rev. E.* 67 (2003) 031601. doi:10.1103/PhysRevE.67.031601.
- [89] K. Van Workum, J.J. de Pablo, Improved simulation method for the calculation of the elastic constants of crystalline and amorphous systems using strain fluctuations, *Phys. Rev. E.* 67 (2003) 011505. doi:10.1103/PhysRevE.67.011505.
- [90] F.S. Bates, G.H. Fredrickson, *Block Copolymer Thermodynamics: Theory and Experiment*, *Annu. Rev. Phys. Chem.* 41 (1990) 525–557. doi:10.1146/annurev.pc.41.100190.002521.
- [91] R.J. Hunter, *Foundations of Colloid Science*, Oxford University Press, 2001.
- [92] P.S. Pershan, *Structure of Liquid Crystal Phases*, World Scientific, 1988. doi:10.1142/0661.
- [93] J.M. Seddon, Structure of the Inverted Hexagonal (HII) Phase, and Non-Lamellar Phase Transitions of Lipids, *Biochim. Biophys. Acta.* 1031 (1990) 1–69. doi:10.1016/0304-

4157(90)90002-t.

- [94] K.A. Koppi, M. Tirrell, F.S. Bates, Shear-Induced Isotropic-to-Lamellar Transition, *Phys. Rev. Lett.* 70 (1993) 1449–1452. doi:10.1103/PhysRevLett.70.1449.
- [95] K.A. Koppi, M. Tirrell, F.S. Bates, K. Almdal, K. Mortensen, Epitaxial Growth and Shearing of the Body Centered Cubic Phase in Diblock Copolymer Melts, *J. Rheol.* 38 (1994) 999–1027. doi:10.1122/1.550600.
- [96] T. Tepe, M.F. Schulz, J. Zhao, M. Tirrell, F.S. Bates, K. Mortensen, K. Almdal, Variable Shear-Induced Orientation of a Diblock Copolymer Hexagonal Phase, *Macromolecules.* 28 (1995) 3008–3011. doi:10.1021/ma00112a061.
- [97] M.M. Dao, M.M. Domach, L.M. Walker, Impact of dispersed particles on the structure and shear alignment of block copolymer soft solids, *J. Rheol.* 61 (2017) 237–252. doi:10.1122/1.4974486.
- [98] M. Lukaschek, D.A. Grabowski, C. Schmidt, Shear-Induced Alignment of a Hexagonal Lyotropic Liquid Crystal as Studied by Rheo-NMR, *Langmuir.* 11 (1995) 3590–3594. doi:10.1021/la00009a050.
- [99] J. Berghausen, J. Zipfel, P. Lindner, W. Richtering, Shear-Induced Orientations in a Lyotropic Defective Lamellar Phase, *Europhys. Lett.* 43 (1998) 683–689. doi:10.1209/epl/i1998-00417-3.
- [100] Hyeok Hahn, A. Joon H. Lee, N.P. Balsara, B.A. Garetz, H. Watanabe, Viscoelastic Properties of Aligned Block Copolymer Lamellae, *Macromolecules.* 34 (2001) 8701–8709. doi:10.1021/MA0109929.
- [101] H. Wang, P.K. Kesani, N.P. Balsara, B. Hammouda, Undulations and disorder in block copolymer lamellae under shear flow, *Macromolecules.* 30 (1997) 982–992.
- [102] S. Qavi, M.A. Firestone, R. Foudazi, Elasticity and Yielding of Mesophases of Block Copolymers in Water-Oil Mixtures, *Soft Matter.* 15 (2019) 5626–5637. doi:10.1039/C8SM02336K.
- [103] S. Qavi, R. Foudazi, Rheological Characteristics of Block Copolymer/Water/Oil Mesophases, *Rheol. Acta.* 58 (2019) 483–498.
- [104] S. Qavi, A. Bandegi, M. Firestone, R. Foudazi, Polymerization in soft nanoconfinement of lamellar and reverse hexagonal mesophases, *Soft Matter.* 15 (2019) 8238–8250. doi:10.1039/C9SM01565E.
- [105] B. Svensson, U. Olsson, P. Alexandridis, Self-Assembly of Block Copolymers in Selective Solvents: Influence of Relative Block Size on Phase Behavior, *Langmuir.* 16 (2000) 6839–6846. doi:10.1021/la9916629.
- [106] Gudrun Schmidt, Stefan Müller, P. Lindner, C. Schmidt, W. Richtering, Shear Orientation of Lyotropic Hexagonal Phases, *J. Phys. Chem. B.* 102 (1998) 507–513. doi:10.1021/JP9725745.
- [107] L. Ramos, François Molino, G. Porte, Shear Melting in Lyotropic Hexagonal Phases, *Langmuir.* 16 (2000) 5846–5848. doi:10.1021/LA000276K.

- [108] K. Luo, Y. Yang, Lamellar Orientation and Corresponding Rheological Properties of Symmetric Diblock Copolymers under Steady Shear Flow, *Macromolecules*. 35 (2002) 3722–3730. doi:10.1021/ma010889j.
- [109] S. Müller, P. Fischer, C. Schmidt, Solid-Like Director Reorientation in Sheared Hexagonal Lyotropic Liquid Crystals as Studied by Nuclear Magnetic Resonance, *J. Phys. II*. 7 (1997) 421–432. doi:10.1051/jp2:1997135.
- [110] R. Linemann, J. Läger, G. Schmidt, K. Kratzat, W. Richtering, Linear and nonlinear rheology of micellar solutions in the isotropic, cubic and hexagonal phase probed by rheo-small-angle light scattering, *Rheol. Acta*. 34 (1995) 440–449. doi:10.1007/BF00396557.
- [111] W. Richtering, J. Laeuger, R. Linemann, Shear Orientation of a Micellar Hexagonal Liquid Crystalline Phase: A Rheo and Small Angle Light Scattering Study, *Langmuir*. 10 (1994) 4374–4379. doi:10.1021/la00023a073.
- [112] K. Mortensen, E. Theunissen, R. Kleppinger, K. Almdal, H. Reynaers, Shear-Induced Morphologies of Cubic Ordered Block Copolymer Micellar Networks Studied by In Situ Small-Angle Neutron Scattering and Rheology, *Macromolecules*. 35 (2002) 7773–7781. doi:10.1021/ma0121013.
- [113] J.F. Berret, F. Molino, G. Porte, O. Diat, P. Lindner, The shear-induced transition between oriented textures and layer-sliding-mediated flows in a micellar cubic crystal, *J. Phys. Condens. Matter*. 8 (1996) 9513–9517. doi:10.1088/0953-8984/8/47/054.
- [114] W.F. Brinkman, P.E. Cladis, Defects in Liquid Crystals, *Phys. Today*. 35 (1982) 48–54. doi:10.1063/1.2915094.
- [115] M. Doi, J.L. Harden, T. Ohta, Anomalous Rheological Behavior of Ordered Phases of Block Copolymers. 2, *Macromolecules*. 26 (1993) 4935–4944. doi:10.1021/ma00070a030.
- [116] P. Alexandridis, U. Olsson, B. Lindman, Self-Assembly of Amphiphilic Block Copolymers: The (EO)₁₃(PO)₃₀(EO)₁₃-Water-p-Xylene System, *Macromolecules*. 28 (1995) 7700–7710. doi:10.1021/ma00127a016.
- [117] B.S. Forney, C.A. Guymon, Nanostructure evolution during photopolymerization in lyotropic liquid crystal templates, *Macromolecules*. 43 (2010) 8502–8510. doi:10.1021/ma101418e.
- [118] C.L. Lester, C.D. Colson, C.A. Guymon, Photopolymerization Kinetics and Structure Development of Templated Lyotropic Liquid Crystalline Systems, *Macromolecules*. 34 (2001) 4430–4438. doi:10.1021/ma001853e.
- [119] C.T. Kresge, M.E. Leonowicz, W.J. Roth, J.C. Vartuli, J.S. Beck, Ordered mesoporous molecular sieves synthesized by a liquid-crystal template mechanism, *Nature*. 359 (1992) 710–712. <http://dx.doi.org/10.1038/359710a0>.
- [120] J.S. Beck, J.C. Vartuli, W.J. Roth, M.E. Leonowicz, C.T. Kresge, K.D. Schmitt, C.T.W. Chu, D.H. Olson, E.W. Sheppard, A new family of mesoporous molecular sieves prepared with liquid crystal

- templates, *J. Am. Chem. Soc.* 114 (1992) 10834–10843. doi:10.1021/ja00053a020.
- [121] P. Feng, X. Bu, D.J. Pine, Control of Pore Sizes in Mesoporous Silica Templated by Liquid Crystals in Block Copolymer–Cosurfactant–Water Systems, *Langmuir*. 16 (2000) 5304–5310. doi:10.1021/la991444f.
- [122] W. Srisiri, T.M. Sisson, D.F. O’Brien, K.M. McGrath, Y. Han, S.M. Gruner, Polymerization of the Inverted Hexagonal Phase, *J. Am. Chem. Soc.* 119 (1997) 4866–4873. doi:10.1021/ja970052x.
- [123] B. Sanz, N. Ballard, J.M. Asua, C. Mijangos, Effect of Confinement on the Synthesis of PMMA in AAO Templates and Modeling of Free Radical Polymerization, *Macromolecules*. 50 (2017) 811–821. doi:10.1021/acs.macromol.6b02282.
- [124] P.J. Flory, *Principles of Polymer Chemistry*, Cornell University Press, 1953.
- [125] H.H. Winter, F. Chambon, Analysis of Linear Viscoelasticity of a Crosslinking Polymer at the Gel Point, *J. Rheol.* 30 (1986) 367–382.
- [126] A.Y. Malkin, S.G. Kulichikhin, *Polymer Compositions Stabilizers/Curing SE-5*, Springer-Verlag, Berlin/Heidelberg, 1991. doi:10.1007/BFb0017998.
- [127] R. Foudazi, P. Gokun, D.L. Feke, S.J. Rowan, I. Manas-Zloczower, Chemorheology of Poly(high internal phase emulsions), *Macromolecules*. 46 (2013) 5393–5396. doi:10.1021/ma401157b.
- [128] P.J. Halley, M.E. Mackay, Chemorheology of thermosets-an overview, *Polym. Eng. Sci.* 36 (1996) 593–609. doi:10.1002/pen.10447.
- [129] M.A. DePierro, C.A. Guymon, Polymer Structure Development in Lyotropic Liquid Crystalline Solutions, *Macromolecules*. 47 (2014) 5728–5738. doi:10.1021/ma500823q.
- [130] I. Koltover, T. Salditt, J.O. Rädler, C.R. Safinya, An Inverted Hexagonal Phase of Cationic Liposome-DNA Complexes Related to DNA Release and Delivery., *Sci.* 281 (1998) 5373:78–81. doi:10.1126/SCIENCE.281.5373.78.
- [131] V. Allain, C. Bourgaux, P. Couvreur, Self-Assembled Nucleolipids: From Supramolecular Structure to Soft Nucleic Acid and Drug Delivery Devices, *Nucleic Acids Res.* 40 (2012) 1891–1903. doi:10.1093/nar/gkr681.
- [132] Y. Li, O.S. Sariyer, A. Ramachandran, S. Panyukov, M. Rubinstein, E. Kumacheva, Universal behavior of hydrogels confined to narrow capillaries, *Sci. Rep.* 5 (2015) 17017. doi:10.1038/srep17017.
- [133] B. Yu, P. Sun, T. Chen, Q. Jin, D. Ding, B. Li, A.-C. Shi, Confinement-Induced Novel Morphologies of Block Copolymers, *Phys. Rev. Lett.* 96 (2006) 138306. doi:10.1103/PhysRevLett.96.138306.
- [134] C. Autran, J.C. de la Cal, J.M. Asua, (Mini)emulsion Polymerization Kinetics Using Oil-Soluble Initiators, *Macromolecules*. 40 (2007) 6233–6238. doi:10.1021/ma070916r.
- [135] T.G.T. Jansen, J. Meuldijk, P.A. Lovell, A.M. van Herk, On the miniemulsion polymerization of

- very hydrophobic monomers initiated by a completely water-insoluble initiator: thermodynamics, kinetics, and mechanism, *J. Polym. Sci. Part A Polym. Chem.* 54 (2016) 2731–2745. doi:10.1002/pola.28155.
- [136] M. Salsamendi, N. Ballard, B. Sanz, J.M. Asua, C. Mijangos, Polymerization kinetics of a fluorinated monomer under confinement in AAO nanocavities, *RSC Adv.* 5 (2015) 19220–19228. doi:10.1039/C4RA16728G.
- [137] J. Dvorkin, R. Nolen-Hoeksema, A. Nur, The squirt-flow mechanism: Macroscopic description, *Geophysics.* 59 (1994) 428–438.
- [138] E. Detournay, A.H. Cheng, *Fundamentals of Poroelasticity 1, II* (1993) 113–171.
- [139] A.L.Z. Leos J. Zeman, *Microfiltration and Ultrafiltration: Principles and Applications*, CRC Press, New York, 1996.
- [140] Q. Li, Q. Bi, H.-H. Lin, L.-X. Bian, X.-L. Wang, A novel ultrafiltration (UF) membrane with controllable selectivity for protein separation, *J. Memb. Sci.* 427 (2013) 155–167. doi:10.1016/j.memsci.2012.09.010.
- [141] A. Rektor, G. Vatai, Membrane filtration of Mozzarella whey, *Desalination.* 162 (2004) 279–286. doi:10.1016/S0011-9164(04)00052-9.
- [142] A. Cassano, M. Marchio, E. Drioli, Clarification of blood orange juice by ultrafiltration: analyses of operating parameters, membrane fouling and juice quality, *Desalination.* 212 (2007) 15–27. doi:10.1016/j.desal.2006.08.013.
- [143] J. Lin, W. Ye, M.-C. Baltaru, Y.P. Tang, N.J. Bernstein, P. Gao, S. Balta, M. Vlad, A. Volodin, A. Sotto, P. Luis, A.L. Zydney, B. Van der Bruggen, Tight ultrafiltration membranes for enhanced separation of dyes and Na₂SO₄ during textile wastewater treatment, *J. Memb. Sci.* 514 (2016) 217–228. doi:10.1016/j.memsci.2016.04.057.
- [144] J. Zhou, D. Wandera, S.M. Husson, Mechanisms and control of fouling during ultrafiltration of high strength wastewater without pretreatment, *J. Memb. Sci.* 488 (2015) 103–110. doi:10.1016/j.memsci.2015.04.018.
- [145] S.Y. Park, S.H. Choi, J.W. Chung, S.-Y. Kwak, Anti-scaling ultrafiltration/microfiltration (UF/MF) polyvinylidene fluoride (PVDF) membranes with positive surface charges for Ca²⁺/silica-rich wastewater treatment, *J. Memb. Sci.* 480 (2015) 122–128. doi:10.1016/j.memsci.2015.01.041.
- [146] A. Hucknall, S. Rangarajan, A. Chilkoti, In Pursuit of Zero: Polymer Brushes that Resist the Adsorption of Proteins, *Adv. Mater.* 21 (2009) 2441–2446. doi:10.1002/adma.200900383.
- [147] S.I. Jeon, J.H. Lee, J.D. Andrade, P.G. De Gennes, Protein—surface interactions in the presence of polyethylene oxide, *J. Colloid Interface Sci.* 142 (1991) 149–158. doi:10.1016/0021-9797(91)90043-8.
- [148] R.M. Dorin, W.A. Phillip, H. Sai, J. Werner, M. Elimelech, U. Wiesner, Designing block

- copolymer architectures for targeted membrane performance, *Polymer (Guildf)*. 55 (2014) 347–353. doi:10.1016/j.polymer.2013.09.038.
- [149] D.-M. Wang, J.-Y. Lai, Recent advances in preparation and morphology control of polymeric membranes formed by nonsolvent induced phase separation, *Curr. Opin. Chem. Eng.* 2 (2013) 229–237. doi:10.1016/j.coche.2013.04.003.
- [150] C.D. Colson, C.L. Lester, C.A. Guymon, Photopolymerization of Lyotropic Liquid Crystalline Systems: A New Route to Nanostructured Materials, *MRS Proc.* 709 (2001) CC9.5.1.
- [151] C.A. Guymon, C.N. Bowman, Kinetic Analysis of Polymerization Rate Acceleration During the Formation of Polymer/Smectic Liquid Crystal Composites, *Macromolecules*. 30 (1997) 5271–5278. doi:10.1021/ma9703970.
- [152] C.J. Davey, Z.-X. Low, R.H. Wirawan, D.A. Patterson, Molecular weight cut-off determination of organic solvent nanofiltration membranes using poly(propylene glycol), *J. Memb. Sci.* 526 (2017) 221–228. doi:10.1016/J.MEMSCI.2016.12.038.
- [153] D. Batra, S. Seifert, M.A. Firestone, The Effect of Cation Structure on the Mesophase Architecture of Self-Assembled and Polymerized Imidazolium-Based Ionic Liquids, *Macromol. Chem. Phys.* 208 (2007) 1416–1427. doi:10.1002/macp.200700174.
- [154] C.L. Lester, S.M. Smith, C.D. Colson, C.A. Guymon, Physical properties of hydrogels synthesized from lyotropic liquid crystalline templates, *Chem. Mater.* 15 (2003) 3376–3384.
- [155] M. Seo, M.A. Hillmyer, Reticulated nanoporous polymers by controlled polymerization-induced microphase separation, *Science* (80-.). 336 (2012) 1422–1425.
- [156] Z. Wang, F. Liu, Y. Gao, W. Zhuang, L. Xu, B. Han, A. Ganzuo Li, G. Zhang, Hexagonal Liquid Crystalline Phases Formed in Ternary Systems of Brij 97–Water–Ionic Liquids, *Langmuir*. 21 (2005) 4931–4937. doi:10.1021/LA050266P.
- [157] M.T. Irwin, R.J. Hickey, S. Xie, S. So, F.S. Bates, T.P. Lodge, Structure–Conductivity Relationships in Ordered and Disordered Salt-Doped Diblock Copolymer/Homopolymer Blends, *Macromolecules*. 49 (2016) 6928–6939. doi:10.1021/acs.macromol.6b01553.
- [158] J. Sax, J.M. Ottino, Modeling of transport of small molecules in polymer blends: Application of effective medium theory, *Polym. Eng. Sci.* 23 (1983) 165–176. doi:10.1002/pen.760230310.
- [159] P. Scherrer, Bestimmung der inneren Struktur und der Größe von Kolloidteilchen mittels Röntgenstrahlen, in: *Kolloidchem. Ein Lehrb.*, Springer Berlin Heidelberg, Berlin, Heidelberg, 1912: pp. 387–409. doi:10.1007/978-3-662-33915-2_7.
- [160] J.I. Langford, A.J.C. Wilson, Scherrer after sixty years: A survey and some new results in the determination of crystallite size, *J. Appl. Crystallogr.* 11 (1978) 102–113. doi:10.1107/S0021889878012844.
- [161] J. Pieracci, J. V Crivello, G. Belfort, H.P. Isermann, Photochemical modification of 10kDa polyethersulfone ultrafiltration membranes for reduction of biofouling, *J. Memb. Sci.* 156 (1999)

- 223–240. doi:10.1016/S0376-7388(98)00347-0.
- [162] J. Garcia-Ivars, M.-I. Iborra-Clar, M.-I. Alcaina-Miranda, B. Van der Bruggen, Comparison between hydrophilic and hydrophobic metal nanoparticles on the phase separation phenomena during formation of asymmetric polyethersulphone membranes, *J. Memb. Sci.* 493 (2015) 709–722. doi:10.1016/J.MEMSCI.2015.07.009.
- [163] J.S. Baker, L.Y. Dudley, Biofouling in Membrane Systems — A Review, *Desalination*. 118 (1998) 81–89. doi:10.1016/S0011-9164(98)00091-5.
- [164] R.E. Cantwell, R. Hofmann, M.R. Templeton, Interactions between Humic Matter and Bacteria when Disinfecting Water with UV Light, *J. Appl. Microbiol.* 105 (2008) 25–35. doi:10.1111/j.1365-2672.2007.03714.x.
- [165] R.A. Damodar, S.-J. You, H.-H. Chou, Study the Self Cleaning, Antibacterial and Photocatalytic Properties of TiO₂ Entrapped PVDF Membranes, *J. Hazard. Mater.* 172 (2009) 1321–8. doi:10.1016/j.jhazmat.2009.07.139.
- [166] N. Daels, S. De Vrieze, I. Sampers, B. Decostere, P. Westbroek, A. Dumoulin, P. Dejjans, K. De Clerck, S.W.H. Van Hulle, Potential of a Functionalised Nanofibre Microfiltration Membrane as an Antibacterial Water Filter, *Desalination*. 275 (2011) 285–290. doi:10.1016/j.desal.2011.03.012.
- [167] H. Ma, Factors affecting membrane fouling reduction by surface modification and backpulsing, *J. Memb. Sci.* 189 (2001) 255–270. doi:10.1016/S0376-7388(01)00422-7.
- [168] F. Yao, G. Fu, J. Zhao, E. Kang, K. Neoh, Antibacterial Effect of Surface-Functionalized Polypropylene Hollow Fiber Membrane from Surface-Initiated Atom Transfer Radical Polymerization, *J. Memb. Sci.* 319 (2008) 149–157. doi:10.1016/j.memsci.2008.03.049.
- [169] P. Alexandridis, T. Alan Hatton, Poly(ethylene oxide)poly(propylene oxide)poly(ethylene oxide) block copolymer surfactants in aqueous solutions and at interfaces: thermodynamics, structure, dynamics, and modeling, *Colloids Surfaces A Physicochem. Eng. Asp.* 96 (1995) 1–46. doi:10.1016/0927-7757(94)03028-X.
- [170] H.-P. Hentze, E. Krämer, B. Berton, S. Förster, M. Antonietti, M. Dreja, Lyotropic Mesophases of Poly(ethylene oxide)-*b*-poly(butadiene) Diblock Copolymers and Their Cross-Linking To Generate Ordered Gels, *Macromolecules*. 32 (1999) 5803–5809. doi:10.1021/ma9904058.
- [171] A. Pitto-Barry, N.P.E. Barry, Pluronic® block-copolymers in medicine: from chemical and biological versatility to rationalisation and clinical advances, *Polym. Chem.* 5 (2014) 3291–3297. doi:10.1039/C4PY00039K.
- [172] P. Alexandridis, Amphiphilic copolymers and their applications, *Curr. Opin. Colloid Interface Sci.* 1 (1996) 490–501. doi:10.1016/S1359-0294(96)80118-X.
- [173] K. Mortensen, W. Brown, B. Nordén, Inverse melting transition and evidence of three-dimensional cubatic structure in a block-copolymer micellar system, *Phys. Rev. Lett.* 68 (1992) 2340–2343. doi:10.1103/PhysRevLett.68.2340.

- [174] P. Alexandridis, U. Olsson, B. Lindman, Phase Behavior of Amphiphilic Block Copolymers in Water–Oil Mixtures: The Pluronic 25R4–Water–p-Xylene System, *J. Phys. Chem.* 100 (1996) 280–288. doi:10.1021/jp951626s.
- [175] P. Alexandridis, U. Olsson, B. Lindman, Structural Polymorphism of Amphiphilic Copolymers: Six Lyotropic Liquid Crystalline and Two Solution Phases in a Poly(oxybutylene)-b-poly(oxyethylene)–Water–Xylene System, *Langmuir*. 13 (1997) 23–34. doi:10.1021/la960733q.
- [176] A. Silberberg, Basic Rheological Concepts, in: Springer, Boston, MA, 1977: pp. 181–190. doi:10.1007/978-1-4613-4172-7_13.
- [177] F. Del Giudice, S.J. Haward, A.Q. Shen, Relaxation Time of Dilute Polymer Solutions: A Microfluidic Approach, *J. Rheol.* 61 (2017) 327–337. doi:10.1122/1.4975933.
- [178] W. Callister, D. Rethwisch, *Materials Science and Engineering, an Introduction*, 8th editio, John Wiley & Sons, 2014.
- [179] A. May, K. Aramaki, J.M. Gutiérrez, Phase Behavior and Rheological Analysis of Reverse Liquid Crystals and W/I₂ and W/H₂ Gel Emulsions Using an Amphiphilic Block Copolymer, *Langmuir*. 27 (2011) 2286–2298. doi:10.1021/la104539q.
- [180] J.L. Harden, M. Doi, The effect of added triblock copolymer on the nonlinear rheology of ordered diblock copolymer mesophases, *J. Rheol.* 40 (1996) 187. doi:10.1122/1.550734.
- [181] S.P. Meeker, R.T. Bonnecaze, M. Cloitre, Slip and flow in pastes of soft particles: Direct observation and rheology, *J. Rheol.* 48 (2004) 1295–1320. doi:10.1122/1.1795171.
- [182] S. Meeker, R. Bonnecaze, M. Cloitre, Slip and Flow in Soft Particle Pastes, *Phys. Rev. Lett.* 92 (2004) 198302. doi:10.1103/PhysRevLett.92.198302.
- [183] I. Masalova, A.Y. Malkin, R. Foudazi, Yield Stress as Measured in Steady Shearing and in Oscillations, *Appl. Rheol.* 18 (2008) 44790. doi:10.3933/ApplRheol-18-44790.
- [184] K.F. Wissbrun, Rheology of Rod-Like Polymers in the Liquid Crystalline State, *J. Rheol.* 25 (1981) 619–662. doi:10.1122/1.549634.
- [185] W. Mingvanish, A. Kellarakis, S.-M. Mai, C. Daniel, Z. Yang, V. Havredaki, I.W. Hamley, A.J. Ryan, C. Booth, Rheology and Structures of Aqueous Gels of Diblock(Oxyethylene/Oxybutylene) Copolymer E 22 B 7, (2000). doi:10.1021/jp001398o.
- [186] H.A. Barnes, The yield stress—a review or ‘παντα ρει’—everything flows?, *J. Nonnewton. Fluid Mech.* 81 (1999) 133–178. doi:10.1016/S0377-0257(98)00094-9.
- [187] J.-B. Salmon, S. Manneville, A. Colin, Shear banding in a lyotropic lamellar phase. II. Temporal fluctuations, *Phys. Rev. E.* 68 (2003) 51504. doi:10.1103/PhysRevE.68.051504.
- [188] S.M. Fielding, Shear banding in soft glassy materials, *Reports Prog. Phys.* 77 (2014) 102601. doi:10.1088/0034-4885/77/10/102601.
- [189] P. Schall, M. van Hecke, Shear Bands in Matter with Granularity, *Annu. Rev. Fluid Mech.* 42

- (2009) 67–88. doi:10.1146/annurev-fluid-121108-145544.
- [190] P.D. Olmsted, Perspectives on shear banding in complex fluids, *Rheol. Acta.* 47 (2008) 283–300. doi:10.1007/s00397-008-0260-9.
- [191] S.M. Fielding, Triggers and signatures of shear banding in steady and time-dependent flows, *J. Rheol.* 60 (2016) 821–834. doi:10.1122/1.4961480.
- [192] I. Masalova, A.Y. Malkin, R. Foudazi, Yield stress of emulsions and suspensions as measured in steady shearing and in oscillations, *Appl. Rheol.* 18 (2008) 44790. doi:10.1515/arh-2008-0013.
- [193] T.G.G. Mason, J. Bibette, D.A. Weitz, Yielding and Flow of Monodisperse Emulsions, *J. Colloid Interface Sci.* 179 (1996) 439–448. doi:10.1006/jcis.1996.0235.
- [194] R. Foudazi, I. Masalova, A.Y. Malkin, The rheology of binary mixtures of highly concentrated emulsions: Effect of droplet size ratio, *J. Rheol.* 56 (2012) 1299–1314. doi:10.1122/1.4736556.
- [195] C. Daniel, I.W. Hamley, M. Wilhelm, W. Mingvanish, Non-linear rheology of a face-centred cubic phase in a diblock copolymer gel, *Rheol. Acta.* 40 (2001) 39–48. doi:10.1007/s003970000124.
- [196] N. Phan-Thien, M. Safari-Ardi, A. Morales-Patino, Oscillatory and simple shear flows of a flour-water dough: a constitutive model, *Rheol. Acta.* 36 (1997) 38–48. doi:10.1007/BF00366722.
- [197] T. Mason, J. Bibette, D. Weitz, Elasticity of Compressed Emulsions, *Phys. Rev. Lett.* 75 (1995) 2051–2054. doi:10.1103/PhysRevLett.75.2051.
- [198] Z. Daneshfar, F. Goharpey, H. Nazockdast, R. Foudazi, Rheology of concentrated bimodal suspensions of nanosilica in PEG, *J. Rheol.* 61 (2017) 955–966. doi:10.1122/1.4995604.
- [199] R.J. Ketz, R.K. Prud'homme, W.W. Graessley, Rheology of concentrated microgel solutions, *Rheol. Acta.* 27 (1988) 531–539. doi:10.1007/BF01329353.
- [200] M. Laurati, G. Petekidis, N. Koumakis, F. Cardinaux, A.B. Schofield, J.M. Brader, M. Fuchs, S.U. Egelhaaf, Structure, dynamics, and rheology of colloid-polymer mixtures: From liquids to gels, *J. Chem. Phys.* 130 (2009) 134907. doi:10.1063/1.3103889.
- [201] P. Sollich, Rheological constitutive equation for a model of soft glassy materials, *Phys. Rev. E.* 58 (1998) 738–759. doi:10.1103/PhysRevE.58.738.
- [202] T. Ohta, Y. Enomoto, J.L. Harden, M. Doi, Anomalous rheological behavior of ordered phases of block copolymers. 1, *Macromolecules.* 26 (1993) 4928–4934. doi:10.1021/ma00070a029.
- [203] R.G. Larson, K.I. Winey, S.S. Patel, H. Watanabe, R. Bruinsma, The rheology of layered liquids: lamellar block copolymers and smectic liquid crystals, *Rheol. Acta.* 32 (1993) 245–253. doi:10.1007/BF00434188.
- [204] B.L. Riise, G.H. Fredrickson, R.G. Larson, D.S. Pearson, Rheology and Shear-Induced Alignment of Lamellar Diblock and Triblock Copolymers, *Macromolecules.* 28 (1995) 7653–7659.
- [205] V.K. Gupta, R. Krishnamoorti, J.A. Komfield, S.D. Smith, Evolution of Microstructure during

- Shear Alignment in a Polystyrene-Polyisoprene Lamellar Diblock Copolymer, *Macromolecules*. 28 (1995) 4464–4474.
- [206] J.D. Clapper, L. Sievens-Figueroa, C.A. Guymon, Photopolymerization in Polymer Templating †, *Chem. Mater.* 20 (2008) 768–781. doi:10.1021/cm702130r.
- [207] M.A. DePierro, C.A. Guymon, Photoinitiation and monomer segregation behavior in polymerization of lyotropic liquid crystalline systems, *Macromolecules*. 39 (2006) 617–626. doi:10.1021/ma0518196.
- [208] B.A. Smith, E.T. Samulski, L.-P. Yu, M.A. Winnik, Tube Renewal versus Reytation: Polymer Diffusion in Molten Poly(ProyyleneOxide), *Phys. Rev. Lett.* 52 (1984) 45–48.
- [209] A.K. Fritzsche, F.P. Price, Crystallization of polyethylene oxide under shear, *Polym. Eng. Sci.* 14 (1974) 401–412. doi:10.1002/pen.760140602.
- [210] N. Ileri Ercan, P. Stroeve, J.W. Tringe, R. Faller, Understanding the Interaction of Pluronics L61 and L64 with a DOPC Lipid Bilayer: An Atomistic Molecular Dynamics Study, *Langmuir*. 32 (2016) 10026–10033. doi:10.1021/acs.langmuir.6b02360.
- [211] K. Bryskhe, K. Schillen, J.-E. Lofroth, U. Olsson, Lipid-block copolymer immiscibility, *Phys. Chem. Chem. Phys.* 3 (2001) 1303–1309. doi:10.1039/b009487k.
- [212] K. Hyun, J.G. Nam, M. Wilhelim, K.H. Ahn, S.J. Lee, Large amplitude oscillatory shear behavior of PEO-PPO-PEO triblock copolymer solutions, *Rheol. Acta.* 45 (2006) 239–249. doi:10.1007/s00397-005-0014-x.
- [213] S.R. Raghavan, S.A. Khan, Shear-Thickening Response of Fumed Silica Suspensions under Steady and Oscillatory Shear, *J. Colloid Interface Sci.* 185 (1997) 57–67. doi:10.1006/JCIS.1996.4581.
- [214] C. Bower, C. Gallegos, M.R. Mackley, J.M. Madiedo, The rheological and microstructural characterisation of the non-linear flow behaviour of concentrated oil-in-water emulsions, *Rheol. Acta.* 38 (1999) 145–159. doi:10.1007/s003970050164.
- [215] D.S. Achilias, A review of modeling of diffusion controlled polymerization reactions, *Macromol. Theory Simulations*. 16 (2007) 319–347.
- [216] P. Sifaka, D.S. Achilias, Polymerization Kinetics and Thermal Degradation of Poly(2-hydroxyethyl methacrylate) / Organo-Modified Montmorillonite Nanocomposites Prepared by *In Situ* Bulk Polymerization, *Macromol. Symp.* 331–332 (2013) 166–172. doi:10.1002/masy.201300065.
- [217] D.S. Achilias, Investigation of the radical polymerization kinetics using DSC and mechanistic or isoconversional methods, *J. Therm. Anal. Calorim.* 116 (2014) 1379–1386. doi:10.1007/s10973-013-3633-y.
- [218] H. Zhao, S.L. Simon, Methyl methacrylate polymerization in nanoporous confinement, *Polymer (Guildf)*. 52 (2011) 4093–4098. doi:10.1016/j.polymer.2011.06.048.

- [219] S. Ravindranath, S.-Q. Wang, M. Olechnowicz, R.P. Quirk, Banding in Simple Steady Shear of Entangled Polymer Solutions, *Macromolecules*. 41 (2008) 2663–2670. doi:10.1021/ma7027352.
- [220] S.-Q. Wang, S. Ravindranath, P.E. Boukany, Homogeneous Shear, Wall Slip, and Shear Banding of Entangled Polymeric Liquids in Simple-Shear Rheometry: A Roadmap of Nonlinear Rheology, *Macromolecules*. 44 (2011) 183–190. doi:10.1021/ma101223q.
- [221] M.A. Calabrese, S.A. Rogers, L. Porcar, N.J. Wagner, Understanding steady and dynamic shear banding in a model wormlike micellar solution, *J. Rheol.* 60 (2016) 1001–1017. doi:10.1122/1.4961035.
- [222] J.-B. Salmon, S. Manneville, A. Colin, Shear banding in a lyotropic lamellar phase. I. Time-averaged velocity profiles, *Phys. Rev. E*. 68 (2003) 51503. doi:10.1103/PhysRevE.68.051503.

Appendix A: Properties of Pluronic Block Copolymers

Figure A-1 shows the chemical structure of a typical Pluronic block copolymer. Variation of copolymer composition (PPO/PEO ratio) and molecular weight (PEO and PPO block length) during synthesis leads to the production of molecules with optimum properties that meet the specific requirements in various areas of technological significance [169].

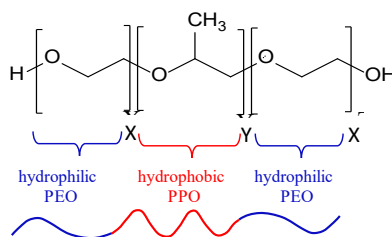


Figure A-1. Chemical structure and schematic representation of a Pluronic block copolymer. X and Y show the degree of polymerization of each blocks.

The Pluronic block copolymers are available in a range of molecular weights and PPO/PEO composition ratios, with a relatively low price (comparable to small molecule surfactants), low toxicity, and stability over a wide pH range [60, 170]. The notation for the Pluronic triblock copolymers starts with the letters L (for liquid), P (for paste), or F (for flakes) followed by a number. The first one or two numbers are codes for the molecular weight of the PPO block, and the last number signifies the weight fraction of the PEO block [169]. For example, Pluronic F127 and Pluronic L121, have the same molecular weight of PPO, but F127 has 70 wt% PEO and L121 has 10 wt% PEO. Figure A-2 shows a diagram of different commercially available Pluronic block copolymers as a function of PPO molecular weight and PEO wt%.

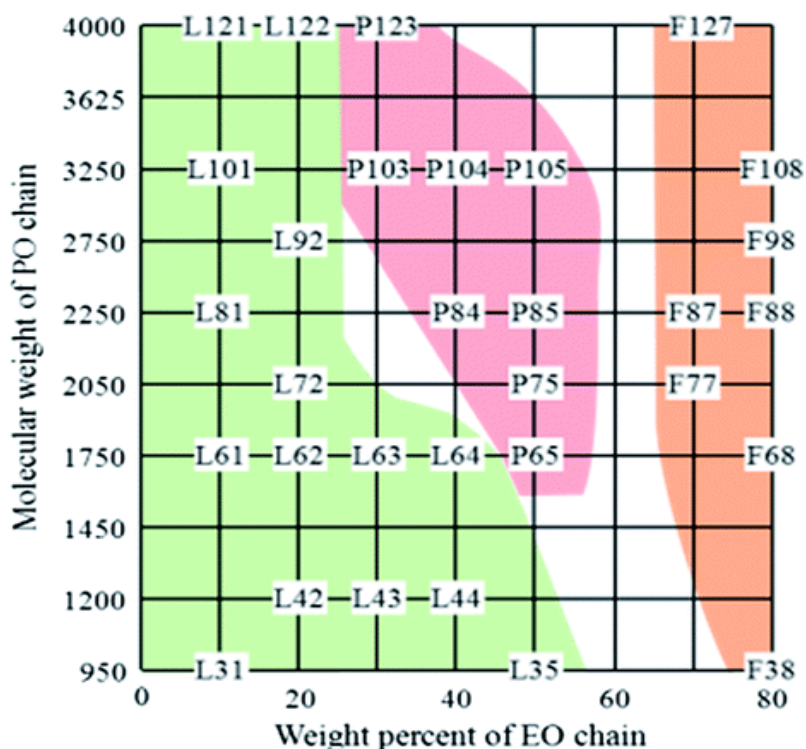


Figure A-2. Pluronic block copolymer grid as a function of PPO molecular weight and PEO wt%, retrieved from [171].

In the presence of water or in ternary systems with water and oil, Pluronic block copolymers can self-assemble into lyotropic liquid crystalline structures, also known as mesophases [172, 173]. Alexandridis and others [105, 169, 174] initiated comprehensive studies on the phase behavior and microstructure of ternary systems consisting of an amphiphilic Pluronic block copolymer and two solvents, one (water) selective for the PEO blocks and another (oil) selective for the PPO block. A rich structural polymorphism has been observed in such ternary copolymer/water/oil systems, with the block copolymer molecules self-assembling to form micro-domains with spherical, cylindrical, or lamellar geometry, discrete or interconnected topology, and liquid-crystalline organization [45, 116, 175]. Figure A-3 shows the phase diagram of Pluronic L64, Pluronic L121, and Pluronic P123 block copolymers in two selective solvents.

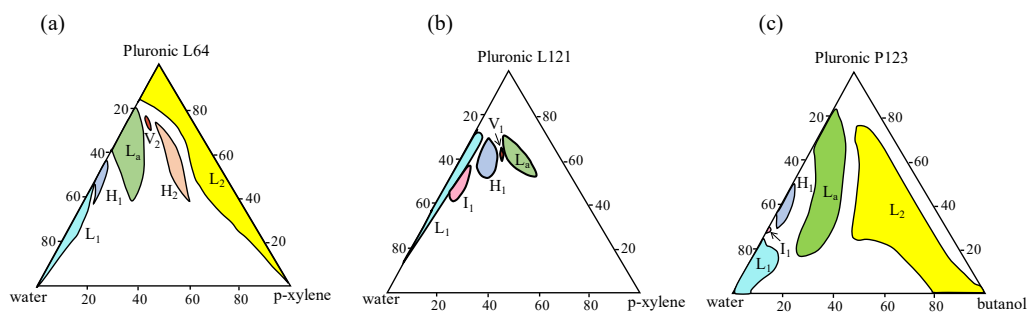


Figure A-3. Phase diagram of (a) Pluronic L64 block copolymer in the presence of water and p-xylene, retrieved from [116]; (b) Pluronic L121 block copolymer in the presence of water and p-xylene, retrieved from [105]; and (c) Pluronic P123 block copolymer in the presence of water and butanol, retrieved from [44]. The concentrations are expressed in wt%.

Appendix B: General Concepts in Rheology

B.1 Hooke's law for shear forces

Rheology is defined as the study of flow behavior. In shear deformation, Hooke's law states that the shear stress (σ) and shear strain (γ) are proportional and the constant of proportionality is the shear elastic modulus (G) as follows:

$$G = \frac{\sigma}{\gamma} \quad (\text{B-1})$$

B.2 Viscosity

When shear stress is applied to a fluid, momentum is transferred, and the shear stress is equivalent to the rate of momentum transferred to the upper layer of the fluid. The coefficient of proportionality between the shear stress and shear rate ($\dot{\gamma}$) is defined as the shear viscosity or dynamic viscosity (η), which is a quantitative measure of the internal fluid friction and is associated with damping or loss of kinetic energy in the system, as follows:

$$\eta = \frac{\sigma}{\dot{\gamma}} \quad (\text{B-2})$$

B.3 Shear thinning and shear thickening fluids

In Newtonian fluids, the shear stress is linearly related to the shear rate, and the viscosity is independent of shear rate. In contrast, the viscosity of non-Newtonian fluids is a function of shear rate. The most common type of non-Newtonian behavior is shear thinning or pseudoplastic flow, in which the fluid viscosity decreases with increasing shear. Ketchup, mayonnaise, lotions, and creams are examples of shear thinning materials. In shear thickening materials, the viscosity increases with shear rate. Heavy whipping cream and cornstarch are examples of shear thickening materials. Figure B-1 shows the Newtonian, shear thinning, and shear thickening behavior of fluids.

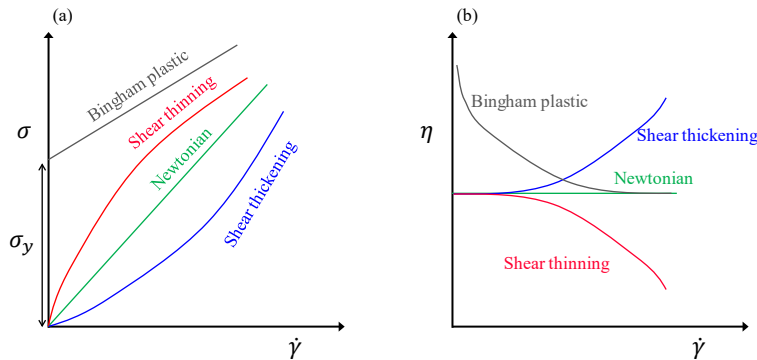


Figure B-1. Schematic illustration of Newtonian, Bingham plastic, shear thinning, and shear thickening fluids in (a) stress versus shear rate and (b) viscosity versus shear rate graphs.

B.4 Yield stress

Many shear thinning fluids can be considered to have both liquid- and solid-like properties and show a property similar to Bingham plastic shown in Figure B-1. At rest, these fluids are able to form intermolecular or interparticle networks. The presence of a network structure gives the material predominantly solid-like characteristics associated with elasticity, which is associated with the yield stress denoted by σ_y [176]. If an external stress is applied that is less than the yield stress, the material will deform elastically. However, when the external stress exceeds the yield stress, the network structure will collapse, and the material will begin to flow like a liquid.

B.5 Viscoelasticity

As the name implies, viscoelasticity describes materials that show a behavior between a liquid (viscous) and a solid (elastic). In purely elastic materials (Hookean solids), the response to a sinusoidal deformation is purely elastic, where the applied stress and response strain are in one phase (with the phase angle of 0° , see Figure B-2a). Newtonian liquids are purely viscous, where the applied stress and response strain are out of phase (with the phase angle of 90°) as shown in Figure B-2b. Viscoelastic materials show a viscoelastic response, where the phase angle is between 0° and 90° as shown in Figure B-2c.

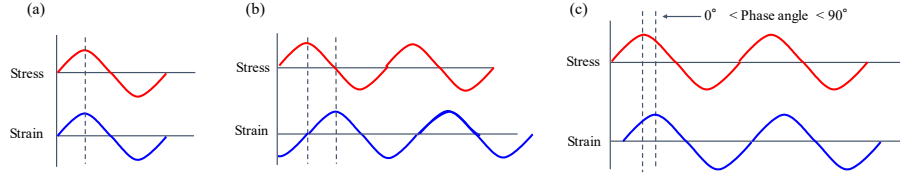


Figure B-2. Response of (a) purely elastic, (b) purely viscous, and (c) viscoelastic materials to deformation.

Applying an oscillatory shear strain, the strain and strain rate can be calculated as follows:

$$\gamma(t) = \gamma_0 \sin \omega t \quad (\text{B-3})$$

$$\dot{\gamma}(t) = \omega \gamma_0 \cos \omega t \quad (\text{B-4})$$

where γ_0 is the maximum deformation, ω is the angular frequency, and t is the time. Given viscoelastic materials with phase angle of δ , the shear stress would be:

$$\sigma(t) = \sigma_0 \sin[\omega t + \delta] \quad (\text{B-5})$$

We may rewrite the Equation (B-5) as follows:

$$\sigma(t) = \sigma_0 \sin \omega t + \sigma_0 \cos \omega t \sin \delta \quad (\text{B-6})$$

Equation (B-6) shows that shear stress consists of two parts, one which is in-phase with the strain, and the other one which is 90° out-of-phase with the strain. Therefore, the ratio of shear stress to shear strain is specified by a modulus G' , in-phase with the shear strain and a modulus G'' , 90° out-of-phase with the shear strain, as follows:

$$\sigma(t) = \gamma_0 G' \sin \omega t + \gamma_0 G'' \cos \omega t \quad (\text{B-7})$$

where,

$$G' = \left(\frac{\sigma_0}{\gamma_0}\right) \cos \delta, \quad G'' = \left(\frac{\sigma_0}{\gamma_0}\right) \sin \delta \quad (\text{B-8})$$

Based on the Euler's formulas, we have:

$$e^{ix} = \cos x + i \sin x, \quad e^{-ix} = \cos x - i \sin x \quad (\text{B-9})$$

An input shear strain and the response shear stress can therefore be written as follows:

$$\gamma(t) = \gamma_0 e^{i\omega t} \quad (\text{B-10})$$

$$\sigma(t) = \sigma_0 e^{i(\omega t + \delta)} \quad (\text{B-11})$$

where, $i = \sqrt{-1}$.

Equation (B-11) can be expanded as follows:

$$\sigma(t) = \sigma_0(\cos \delta + i \sin \delta)e^{i\omega t} \quad (\text{B-12})$$

Comparing equations (B-8) and (B-12) we have:

$$\sigma(t) = \frac{e^{i\omega t}}{\gamma_0}(G' + i G'') \quad (\text{B-13})$$

We can define a complex modulus, G^* as follows:

$$G^* = G' + iG'' \quad (\text{B-14})$$

The elastic (storage) modulus (G') is a measure of the elasticity of material or the ability of the material to store energy. The viscous (loss) modulus (G'') is a measure of the material's ability to dissipate energy.

The viscosity measured in an oscillatory experiment is a complex viscosity (η^*) similar to the way the modulus can be expressed as the complex modulus. η^* is correlated to G^* as follows:

$$\eta^* = \frac{G^*}{\omega} \quad (\text{B-15})$$

where ω is the angular frequency of deformation.

Relaxation time is the characteristic time associated with large-scale motion in the structure of materials, denoted by τ , and is defined by the ratio of viscosity to elastic modulus (G) as follows:

$$\tau = \frac{\eta}{G} \quad (\text{B-16})$$

Polymer solutions can possess a spectrum of relaxation times, related to relaxation processes occurring within and outside the chain itself [177]. Thus, polymers usually have a relaxation time spectra where different relaxation times arise from the multiple relaxation processes occurring on the single subchains, as well as those related to the entire chain, are present [177].

Figure B-3 shows the general response of materials in a frequency sweep test. Four different regions (behaviors) can be distinguished. In the terminal (or viscous) region, the period of oscillation is too long and materials behave like a liquid, $G'' > G'$. In the rubbery plateau region, the contribution of elasticity is higher and $G' > G''$. The crossover point indicates the transition from the terminal to the rubbery plateau region and corresponds to the longest relaxation time of the system [83]. In the transition region, the period of the oscillation is too short to allow for complete rearrangement of the polymer chains and $G'' > G'$. In the glassy region, material is trapped in a glass state and no configurational rearrangement occurs. In this region, stress response to a given strain is very high.

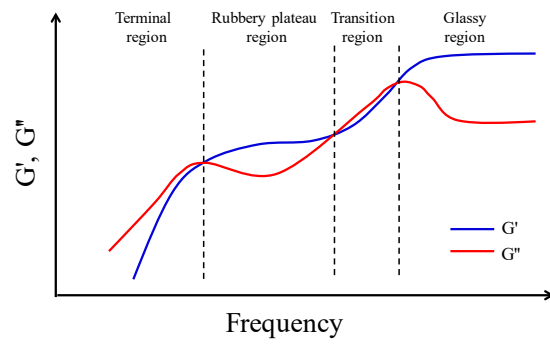


Figure B-3. Schematic illustration of the general material response in a frequency sweep test.

Appendix C: Physical Properties of Pluronic Block Used in This Study

The physical properties of the Pluronics provided by the manufacturer are summarized in Table C-1.

Table C-1. Physical properties of the Pluronics provided by the manufacturer.

Pluronic	L64	P84	L121	P123
EO repeating unit	13	19	5	20
PO repeating unit	30	43	68	70
M _w (g/mol)	2900	4200	4400	5750
PEO fraction (wt%)	40	40	10	30
Density (g/cm ³)	1.05	1.045	1.03	1.05

The above stated densities are used in calculating volume fractions from weight fractions.

Appendix D: Calculating lattice parameters from SAXS data

Figure D-1 shows the typical SAXS patterns for different mesophase structures.

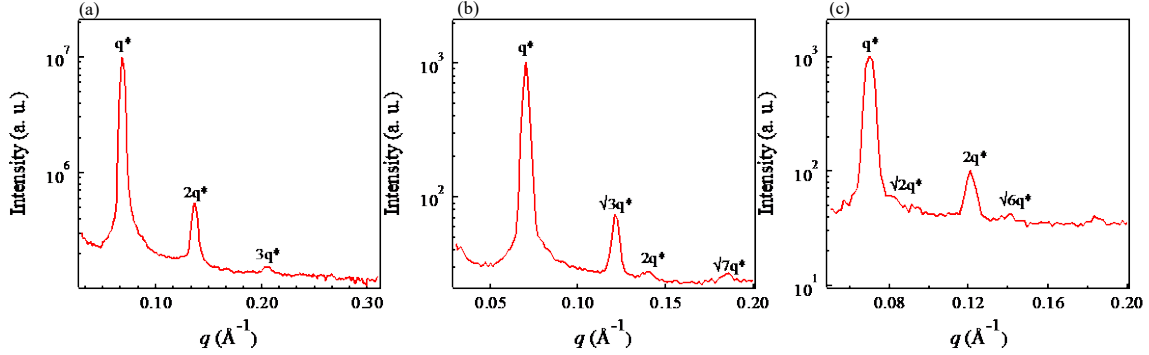


Figure D-1. Typical SAXS patterns for different mesophase structures. (a) lamellar mesophases show 1:2:3:4... relative peak positions, (b) hexagonal mesophases show 1: $\sqrt{3}$:2: $\sqrt{7}$: relative peak positions, (c) BCC mesophases show 1: $\sqrt{2}$:2: $\sqrt{6}$... relative peak positions.

From the scattering profiles, the lattice parameters of the mesophases polymers can be determined using Bragg's law. Bragg's law is as follows:

$$2d \sin \theta = n\lambda \quad (\text{D-1})$$

where λ is the X-ray wavelength, θ is the scattering angle, n is the order of reflection (taken as 1 for the principal scattering vector, q^*), and d is the lattice parameter [44]. The magnitude of the scattering vector, q , is:

$$q = \frac{4\pi \sin \theta}{\lambda} \quad (\text{D-2})$$

For a lamellar structure, the lattice parameter, d , also known as the lamellar periodicity, can thus be defined as follows:

$$d = \frac{2\pi}{q^*} \quad (\text{D-3})$$

For hexagonal mesophases, the lattice parameter, a , which is equal to the distance between the centers of adjacent cylinders, can be calculated as [43]:

$$a = \frac{4\pi}{\sqrt{3}q^*} \quad (\text{D-4})$$

In the case of the micellar cubic mesophase, the first four Bragg peaks identified from SAXS data in Figure D-1a are indexed as 110, 200, 211, and 220 [178]. The slope of the line passing through the origin of the $\frac{1}{d_{hkl}}$ versus $(h^2 + l^2 + k^2)^{1/2}$, is equal to the reciprocal of the lattice parameter, $\frac{1}{d_c}$ [43, 179].

We can define the apolar domain volume fraction, ϕ , as the volume fraction of the oil phase and the PPO block, and the polar domain volume fraction, $1 - \phi$, as the volume fraction of water and the PEO block. Knowing the lattice parameter and volume fractions, the thickness of the apolar domain in the lamellar mesophases (δ) would be [43]:

$$\delta = d\phi \quad (\text{D-5})$$

For the normal hexagonal mesophases, apolar domain size (α) is calculated as follows [43]:

$$\alpha = a \left(\frac{\sqrt{3}}{2\pi} \phi \right)^{1/2} \quad (\text{D-6a})$$

For reverse hexagonal system, we simply substitute ϕ by $1 - \phi$ in the Equation (D-6a). Derivation of Equation (D-6a) is simple. In fact, in a hexagonal micelle with lattice parameter of a , there are three full cylinders with the radius of α present. The ratio between cylinders volume to the hexagon volume is equal to the volume fraction of cylinders (apolar domains in the case of normal hexagonal mesophases). Therefore:

$$\phi = \frac{3\pi\alpha^2}{3\frac{\sqrt{3}}{2}a^2} \quad (\text{D-6b})$$

Solving Equation (D-6b) for α provides Equation (D-6a).

For the micellar cubic mesophase, there are two full spheres with the radius R_c present in a cube with lattice parameter d_c . The ratio between spheres volume to the cube volume is equal to the volume fraction of spheres (apolar domains in the case of normal micellar cubic mesophases). Therefore,

$$\phi = 2 \frac{\frac{4}{3}\pi R_c^3}{d_c^3} \quad (\text{D-7a})$$

Thus, solving Equation (D-7a) for R_c and knowing that the apolar domain size is $\alpha_c = 2R_c$, provides the apolar domain size as follows:

$$\alpha_c = 2d_c \left(\frac{3\phi}{8\pi} \right)^{1/3} \quad (\text{D-7b})$$

For the reverse micellar cubic system, we simply substitute ϕ by $1 - \phi$ in Equation (D-7b). Figure D-2 schematically shows the lattice parameter, polar and apolar domains in micellar cubic, lamellar, normal hexagonal, and reverse hexagonal mesophases.

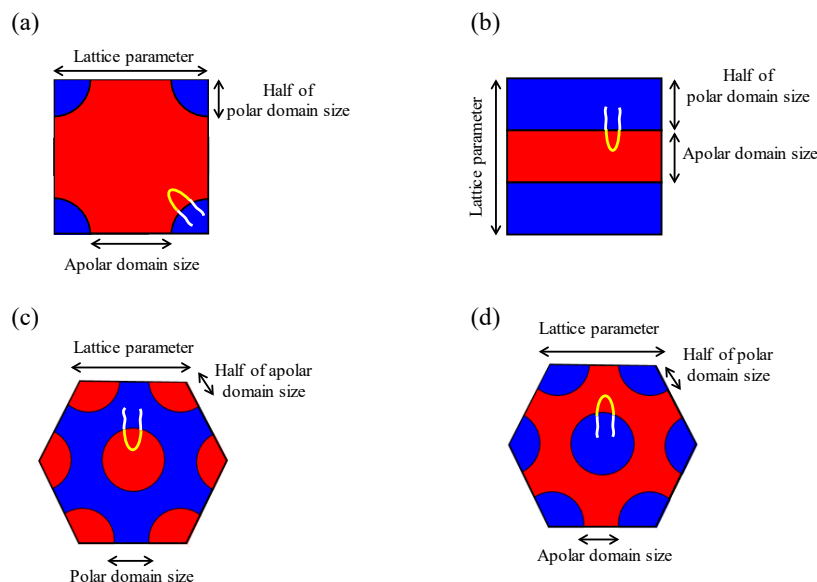


Figure D-2. Schematic illustration of lattice parameter, polar and apolar domain sizes in (a) micellar cubic, (b) lamellar, (c) normal hexagonal, and (d) reverse hexagonal mesophases.

To calculate the volume fraction of each phase, it is assumed that the system is completely segregated with no partitioning of water in the PEO block or oil in the PPO block, and that each component is characterized by its bulk density [116]. Note that this is not rigorously accurate, as the PEO and PPO will partition into the water and oil phases, respectively. However, these assumptions greatly simplify our calculations without losing a great deal of information [102].

For Pluronic L64, the PPO block constitutes 60% of the block copolymer weight. Assuming PPO and PEO to be at bulk density ($\text{PPO}_{M_w \sim 2000} \sim 1.005 \text{ g/cm}^3$ and $\text{PEO}_{M_w \sim 1000} \sim 1.11 \text{ g/cm}^3$), we can conclude that approximately 62% of polymer volume is the PPO block, while PEO makes up the other 38% of Pluronic L64 volume. We can use this method to calculate the volume fraction of PEO and PPO in other Pluronics as summarized in Table D-1.

Table D-1. Volume fraction of PEO and PPO in different Pluronics using the bulk density of their PEO and PPO blocks.

Pluronic	L64	P84	L121	P123
PPO density (g/cm ³)	1.005	1.004	1.0	1.0
PEO density (g/cm ³)	1.11	1.12	1.13	1.12
PPO volume fraction	62	62	91	72
PEO volume fraction	38	38	9	28

Appendix E: Rheological Measurements Performed on Mesophases for Chapter 3 Data

E.1 Rheological measurements

Rheological tests are carried out with the Discovery Hybrid Rheometer DHR-3. A 40 mm parallel plate geometry with 1 mm gap is used for the measurements, unless otherwise noted. The temperature during the tests is controlled at 25 °C by a peltier plate system. Flow curves are obtained from simple shear measurements at different shear rates. Dynamic oscillatory shear tests are done as follows: (i) an isothermal dynamic amplitude sweep is carried out at fixed frequency of 10 rad/s, and (ii) an isothermal dynamic frequency sweep is done by measuring elastic and loss moduli at a fixed strain of 0.5%, which is in the linear viscoelastic regime as verified by amplitude sweep tests. Stress relaxation behavior is obtained by flow cessation (stopping the flow) after applying step-strains of 1% and 50%, where the mesophases are in the linear and nonlinear viscoelastic regions (according to amplitude sweep experiments), respectively. A flow protocol, schematically shown in Figure E-2, is used to study the alignment of mesophases under shear and their relaxation. In particular, a strain of 5% (non-linear viscoelastic region) with angular frequency of 10 rad/s is applied to the samples over a total of 600 min, during which the test is stopped at specific times, and a frequency sweep experiment is performed to measure the evolution of the dynamic moduli of the system (Figure E-2). After 600 min, the flow is stopped (zero shear rate) over 1000 min, during which the dynamic moduli of samples are measured at specific times with the frequency sweep experiment.

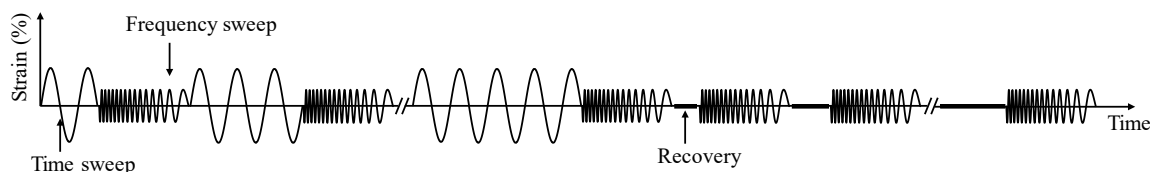


Figure E-2. Schematic representation of flow protocol used for shear-induced alignment and relaxation.

E.2 Rheo-small angle neutron scattering (Rheo-SANS) measurements

Rheo-SANS experiments were performed at the National Institute for Standard and Technology Center for Neutron Research (NCNR) in Gaithersburg, MD. The procedures used were as follows: Data are collected using NG7 30 m SANS instrument, where a neutron beam with wavelength of 6 Å and spread of Dk/k of 0.15 is used to collect scattering at sample-to-detector distance of 2.5 m. Shear fields are applied using a Couette shear cell controlled by an Anton Paar Physica MCR 501 Rheometer (Anton Paar, Graz Austria). The Couette shear cell consists of a titanium cup with 28 mm diameter and 2 mm gap size. Deuterated water is used in formulations to induce the contrast for SANS studies. The radial scattering pattern is collected.

Appendix F: SAXS Graphs for Mesophase Samples in Chapter 3

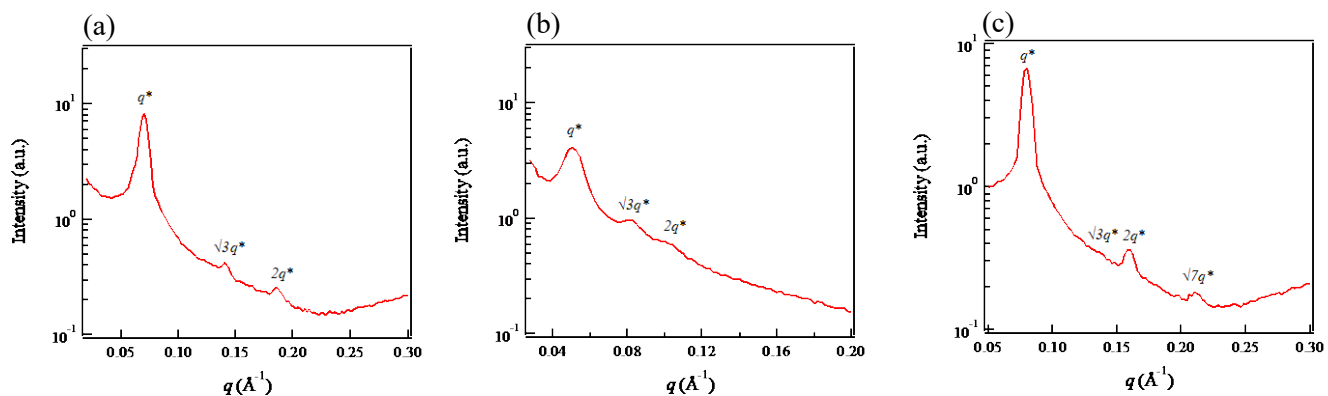


Figure F-1. SAXS graphs for hexagonal samples. (a) P84_40/15/45_H₂, (b) L121_60/25/15_H₂, and (c) P84_50/45/5_H₁.

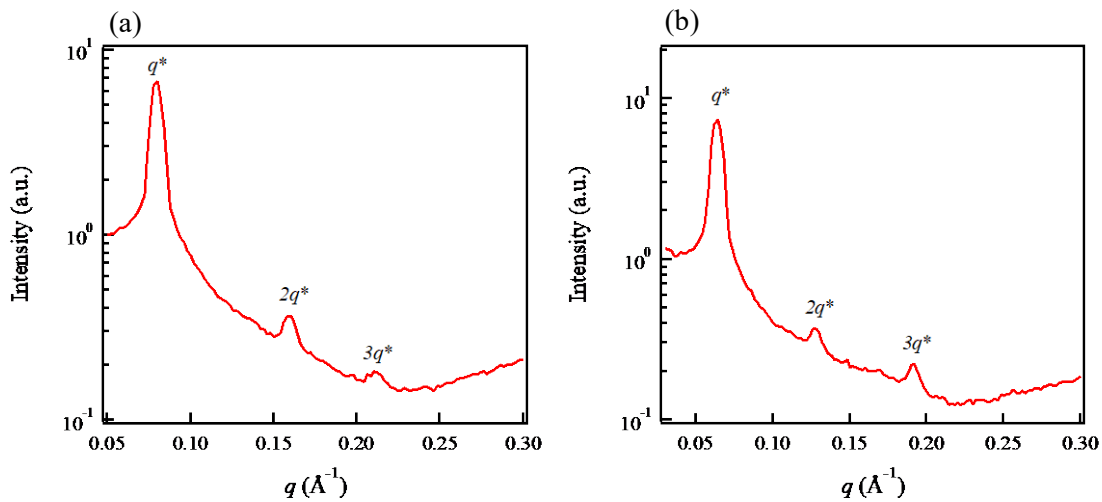


Figure F-2. SAXS graphs for hexagonal samples. (a) P84_60/35/5_L and (b) L121_40/35/25_L.

Appendix G: Rheological Characteristics of Mesophases

G.1 Wall-slip

Mesophases look like a transparent paste, where their flow is dependent on rearrangement of micelles and grains. In some mesophase systems, the sliding on a very smooth surface is observed rather than flowing [180]. Wall-slip in complex fluids makes the flow behavior dependent on the type of geometry and the domain size of the flow field [181–183]. To study the slippage behavior of mesophases, a set of flow-sweep experiments were performed on four typical samples (two lamellar and two hexagonal samples, presented in Chapter 3) using the parallel plate geometry with three different gap sizes of 0.8, 1, and 1.2 mm of smooth parallel plate (PP) surface and with gap size of 0.8 mm of cross-hatched (C/H) surface, as shown in Figure G-1. It can be seen that the flow curve does not change with gap size and surface roughness. Therefore, we conclude that mesophase samples do not have slippage during flow measurements.

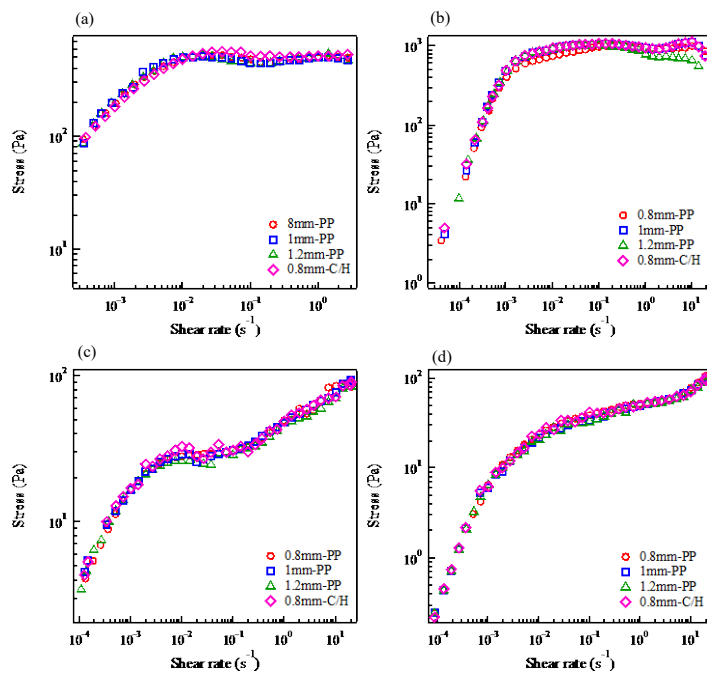


Figure G-1. Flow behavior of typical mesophases with different gap sizes and surfaces: (a) Pluronic P84_50/45/5_H₁, (b) Pluronic L121_60/25/15_H₂, (c) Pluronic P84_60/35/5_L, and (d) Pluronic P123_60/35/5_L.

G.2 Flow behavior

Flow curves of studied samples are shown in Figure G-2. The measured values of the stress at low shear rates are extrapolated to zero shear rate and considered as the yield stress point denoted by $\sigma_{y, shear}$ in Table G-1. All flow curves are practically similar and show the viscoplastic behavior with yield stress as also reported by other researchers [79, 80, 184, 185]. However, the yield stress values for a few lamellar samples are fairly low (<1 Pa) – an artifact due to the limited attainable low shear rates – which may be considered as zero [186]. The lamellar samples overall show lower yield stresses than hexagonal ones, which is attributed to the easier sliding of planes than cylinders. Yield strain values from shear experiment, shown in Table G-1, are calculated as:

$$\gamma_{y, shear} = \frac{\sigma_{y, shear}}{G'} \quad (G-1)$$

where G' is the elastic modulus of the sample in the linear viscoelastic region.

The presence of the stress plateau in the flow curves may be an indicator of shear banding in the mesophases as discussed previously [187–191]. However, velocimetry techniques are needed for direct detection of shear banding in complex fluids.

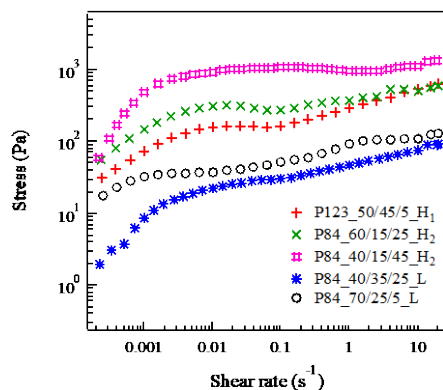


Figure G-2. Flow curves of typical lamellar and hexagonal mesophases.

G.3 Amplitude sweep

Amplitude sweep tests are done to determine the linear viscoelastic region of each mesophase, as shown in Figure G-3. The point where the storage modulus (G') starts to decrease with strain is the threshold of the non-linear viscoelastic region, γ_{LVE} , and can be considered as a yield point [192, 193]. All mesophases show the same trend in the amplitude sweep curves. This trend is known as type III non-linear behavior, which is made evident by a weak strain overshoot and a local maximum in loss modulus (G''). Polymer solutions and highly concentrated emulsions (HCEs) have the same behavior [81, 82, 194, 195]. In emulsions and colloidal systems, type III behavior is attributed to structural rearrangement in the large scale and/or flow of the droplets above the yield strain point [196, 197]. An alternative definition for yield strain is that it occurs at the crossover of G' and G'' , $\gamma_{y,G'=G''}$, beyond which the loss modulus (as a measure of energy dissipation) is dominant.

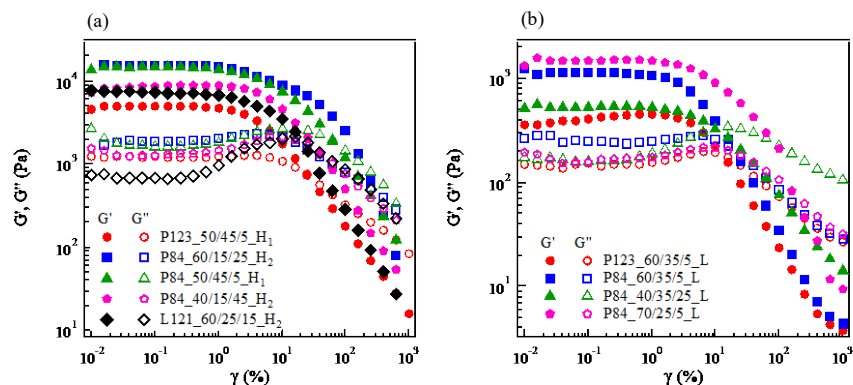


Figure G-3. Amplitude sweep experiments, at fixed frequency of 10 rad/s for (a) hexagonal and (b) lamellar samples.

Table G-1 shows the values of yield stress and strain from oscillatory tests, based on the two definitions mentioned above. Additionally, the values from flow curves (simple shear experiment) are listed. Yield stress obtained from the simple shear experiment is much lower than that from the oscillatory shear. Such discrepancies between yield stresses obtained from oscillatory and simple shear measurements are reported in the literature [192]. A similar trend is observed by Daneshfar and others for concentrated suspensions. They suggest that the yield stress obtained from flow curves could be due to the bulk flow (the point below at which the grains cannot move), while the γ_{LVE} is related to the yielding within grains or domains [198]. Similarly for mesophases, $\sigma_{y,LVE}$ can be attributed to the rearrangement in the level of micelles, while the $\sigma_{y,shear}$ is related to the rearrangement of the crystalline domains.

Table G-1. Calculated values of yield stress and yield strain for different mesophase systems from simple shear and oscillatory shear experiments.

Sample	γ_{LVE}	$\gamma_{y,G'=G''}$	$\gamma_{y,shear}$	σ_{LVE}	$\sigma_{y,G'=G''}$	$\sigma_{y,shear}$
Unit	(%)	(%)	(%)	(Pa)	(Pa)	(Pa)
P84_40/35/25_L	2.51	63.11	0.46	34.26	75.26	2.58
P84_70/25/5_L	1.00	15.85	0.16	7.14	164.51	2.28
P84_60/35/5_L	1.59	15.85	0.04	16.49	54.26	0.42
P123_60/35/5_L	2.51	15.85	0.05	11.40	37.06	0.21
P123_50/45/5_H1	1.59	25.15	0.21	73.75	266.36	10.20
P84_60/15/25_H2	1.00	25.18	0.5	149.77	903.73	8.21
P84_50/45/35_H1	1.59	63.30	8.85×10^{-3}	211.48	1746.77	1.32
P84_40/15/45_H2	2.52	39.91	0.01	211.89	758.45	1.21
L121_60/25/15_H2	1.59	15.90	5.54×10^{-3}	103.33	517.32	4.21

Our recently proposed model [102], predicts the average elastic modulus of polycrystalline mesophases from the single crystal unit. The van der Waals interaction between nearest neighbor micelles is assumed to be the dominant force responsible for the elasticity of the mesophases. The model suggests that the shear modulus is highly dependent on the distance between micelles and a power-law model can be fitted to the zero-shear modulus (G_0) versus the reciprocal intermicellar distance ($\frac{1}{D}$) curve at a constant micelle size, where the power-law index for the lamellar and hexagonal systems are approximately 3 and 4, respectively [102]:

$$G_0 \sim \frac{1}{D^n} \quad (G-2)$$

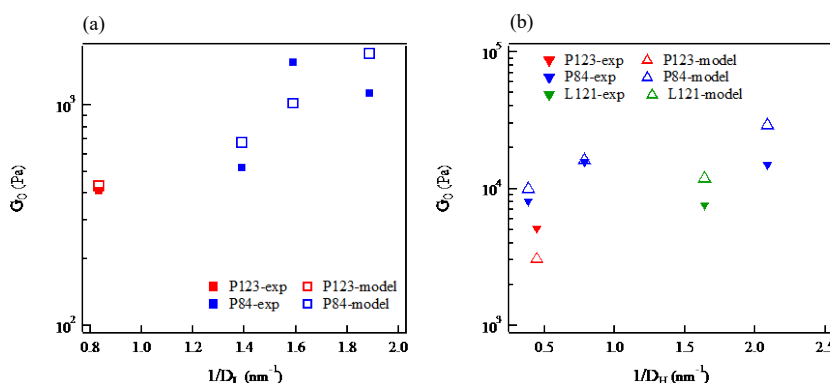


Figure G-4. The zero-shear modulus versus the reciprocal of intermicellar distance for (a) lamellar and (b) hexagonal samples.

The experimental data in this work along with the values from the developed model are compared in Figure G-4. The model can predict the experimental data fairly well for both hexagonal and lamellar sample sets with the same order of magnitude of zero-shear elastic moduli. The deviation observed could be due to the assumptions made for simplicity of the model, namely only considering the interaction of the nearest neighbors and obtaining micellar size and intermicellar distance by assuming complete segregation of the PEO and PPO domains.

G.4 Frequency sweep

Dynamic frequency sweep experiments are done on samples in the linear regime to measure the linear viscoelastic properties of the mesophases. As seen in Figure G-5, G' is higher than G'' in the whole frequency range (0.06-600 rad/s) for all mesophases that imply the solid-like behavior of the samples. G' is nearly frequency-independent with a subtle increase with frequency. All samples are in the rubbery-plateau region of the universal frequency sweep curve of viscoelastic materials, where G' is higher than G'' and no G' - G'' crossover is seen in frequency sweep data, indicating high structural relaxation times of mesophases.

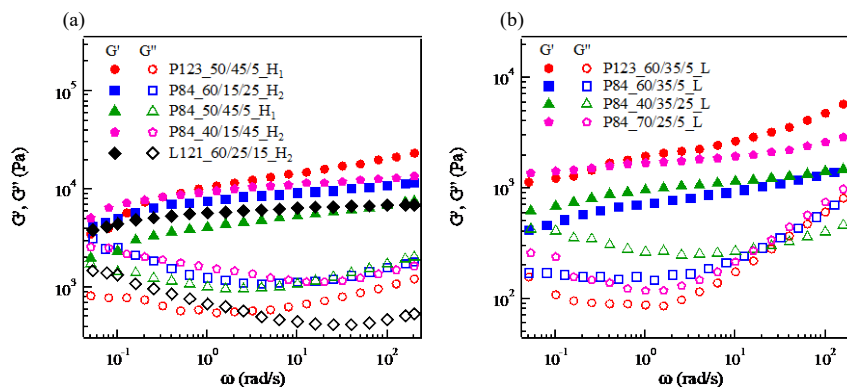


Figure G-5. Frequency sweep experiment data for (a) hexagonal and (b) lamellar samples.

A shallow minimum in G'' of mesophases is a characteristic of polymeric gels and has been observed for emulsions and soft-glassy materials as well [194, 197, 199–201]. The minimum in loss modulus shows the presence of two relaxation behaviors in the system and the transition from α -relaxation (long time, related to low frequency, attributed to grain-size scale) to β -relaxation (short time, high frequency, attributed to the micelle size scale). Angular frequency at the G''_{\min} is plotted against the ratio of normalized lattice parameter to grain size of each mesophase sample in Figure G-6. Data suggest that there is a linear relationship between the angular frequency at the minimum of the loss modulus and the normalized lattice parameter

versus grain size. The ratio of lattice parameter to grain size is used to consider the contributions of both defects (low frequency relaxation) and micelles (high frequency relaxation) in the location of G''_{\min} . The results suggest that the higher the probability of finding defects in the system, the higher the angular frequency where the minimum in G'' takes place. The slope of the linear correlation is about eight times higher for hexagonal mesophases than for the lamellar one. Therefore, the crossover of α - to β -relaxation is more sensitive to the ratio of lattice parameter to grain size in hexagonal samples than in lamellar systems.

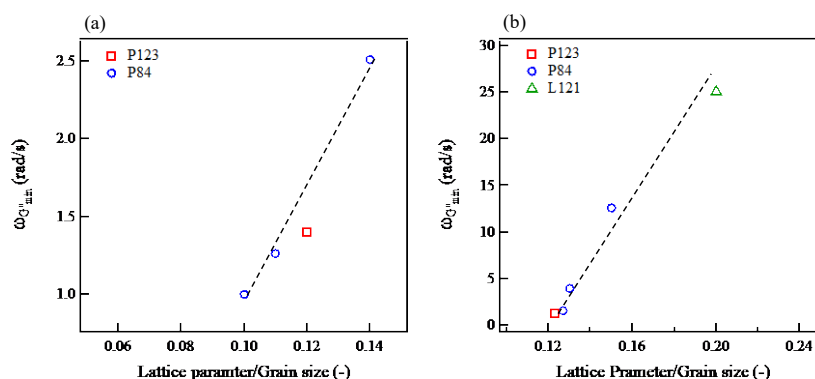


Figure G-6. Angular frequency at the minimum of loss modulus versus the ratio of lattice parameter to grain size for (a) lamellar and (b) hexagonal samples.

G.5 Stress relaxation

A step-strain of γ is applied to the mesophases, and then the stress relaxation behavior is recorded with time. The stress versus time graphs for four typical samples are shown in Figure G-7. At relatively small strains in the linear viscoelastic (LVE) regime (1%), the samples relax to a finite value of stress with a unimodal relaxation time distribution with average time of τ_1 associated with linear viscoelasticity [115]. However, at high strains (50%), the systems relax in two steps, showing a second average relaxation time of τ_2 . Such behavior is due to the instability of the system at high strains and has been predicted for ordered mesophases of block copolymer melts [115, 202]. The two relaxation times after applying high strains should not be confused with the two relaxations from the frequency sweep experiments in LVE regime discussed in Section G.4, for which at least the slow one is associated with nonlinear deformation.

Lamellar and hexagonal LLCs have a mesoscopic nature, wherein intermicellar interactions and grain size are the key players in their rheological properties [102]. At high strains, the mesophases behave non-linearly (see Figure G-3), and the disruption of intermicellar interactions and slippage take place [115]. Additionally, the nonlinear strain eliminates defects in LLCs, whereas they spontaneously re-form when the deformation is stopped [100, 203].

Doi and others [115] proposed a critical value for the strain, $\gamma_c = \frac{\pi}{2}$, for which the instability in the flow occurs. Study results show that the critical value for ternary systems of block copolymer/water/oil is much lower than the proposed value for block copolymer melts. Nonetheless, such phenomena still takes place in mesostructured bock copolymers in solvents.

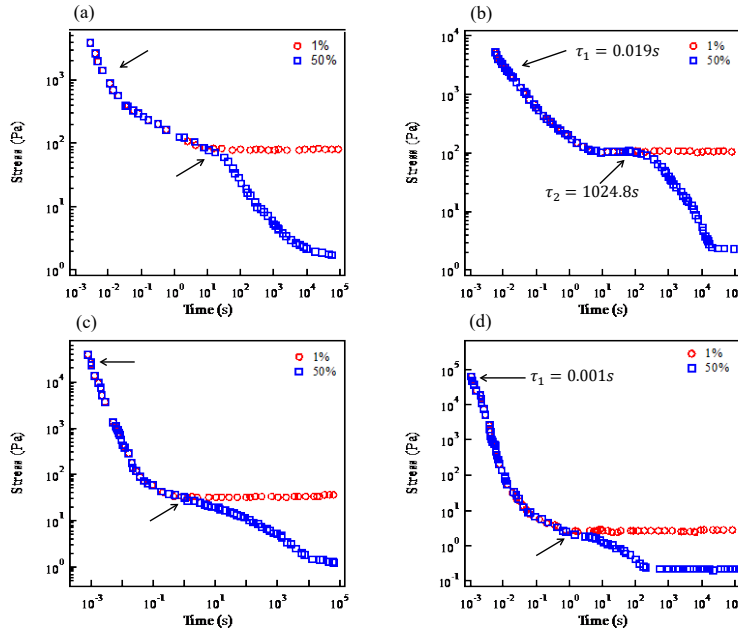


Figure G-7. Stress relaxation with time after applied strains of 1% and 50% for: (a) Pluronic P84_50/45/5_H₁, (b) Pluronic L121_60/25/15_H₂, (c) Pluronic P84_60/35/5_L, and (d) Pluronic P123_60/35/5_L.

To calculate the relaxation times, shown on the figures, we have used the simple Maxwell relaxation model for each step:

$$\sigma = \sigma_0 e^{-t/\tau} \quad (G-3)$$

where τ is the relaxation time, and σ and σ_0 are the stress at time t and initial stress, respectively. When $t = \tau$, the ratio of stress to initial stress σ/σ_0 is $1/e$.

G.6 Shear induced alignment and relaxation behavior

A strain amplitude of 5% with angular frequency of 10 rad/s (which is in the non-linear viscoelastic regime) is applied to two typical samples (one lamellar and one hexagonal) for a

total of 600 min to induce alignment. At different times, the aligning strain is stopped, and the frequency sweep measurement is quickly performed (Figure G-8). It can be seen that G' decreases in the whole range of frequency with time during shear deformation. The observed behavior can be used as evidence for shear alignment [100, 204, 205]. The nonlinear shear deformation eliminates defects in LLCs, and thus enhances the shear-induced alignment [203]. During shear deformation, G'' is constant at high frequencies, $\omega > 10$ rad/s, and decreases in the low frequency region, $\omega < 10$ rad/s, where the contribution of defects (grain boundaries and dislocation) is dominant. Hahn and others [100] have observed a constant G'' in the frequency range of 1-100 rad/s. They mentioned that G'' is dominated by fast relaxation times, and therefore it is not influenced by defects. We believe that G'' is sensitive to defects at very low frequencies (pertaining to large characteristic sizes), and it is influenced by the alignment of domains and/or relaxation defects. In other words, depending on the mesostructure, a wide-enough frequency range can reveal responses from both grain and micellar structures in the low and high frequency regimes, respectively.

We have performed rheo-SANS on a typical lamellar sample, Pluronic P84_60/35/5_L, in a simple shear test. The 2D radial scattering patterns are presented in Figure G-9a. Data in Figure G-9b show the azimuthal intensities about a specific q range. Rheo-SANS results confirm that there is no shear-induced phase transition and the system structure remains intact during deformation (Figure G-9c). However, shear-induced alignment takes place at shear rates higher than approximately 10^{-1} s^{-1} (Figure 4-12b). Two specific peaks are observed in intensity versus ϕ plots, associated with two bright spots in the 2D SANS patterns in Figure G-9a.

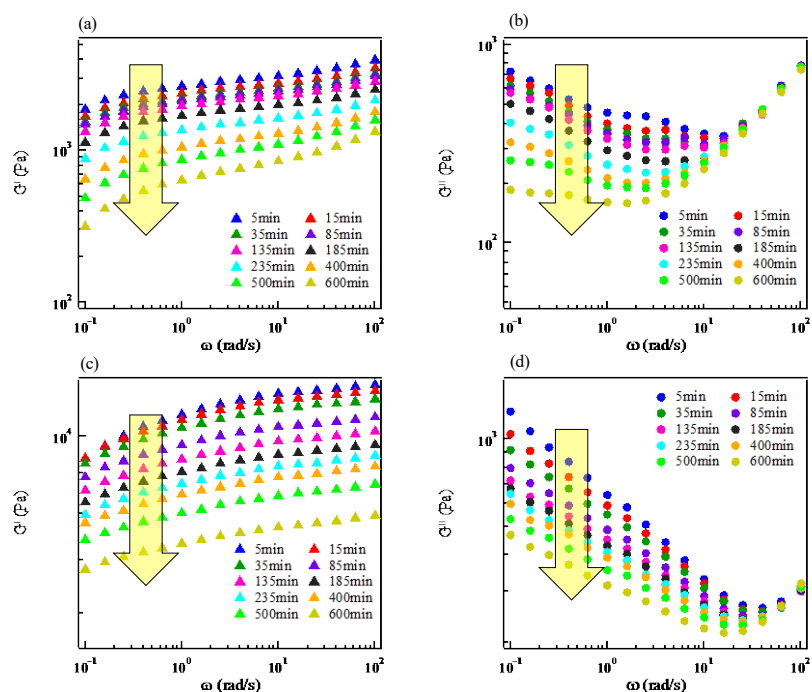


Figure G-8. Evolution of elastic modulus and loss modulus at different times during shear-induced alignments for (a) and (b) P123_60/35/5_L and (c) and (d) L121_60/25/15_H₂ samples. The arrow direction shows the increase in time in all graphs.

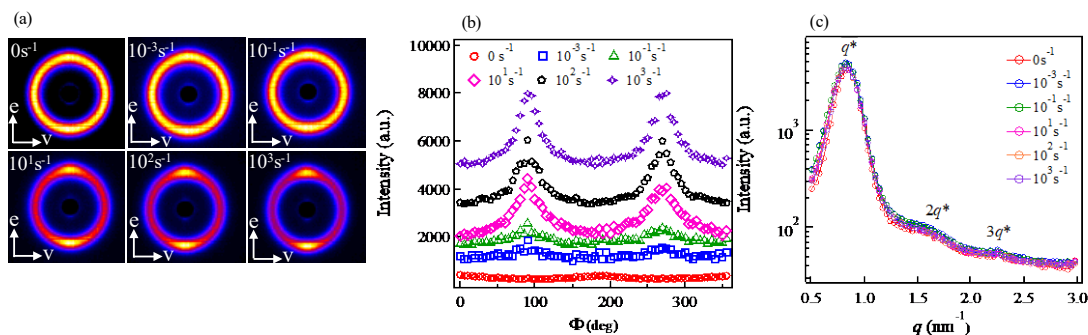


Figure G-9. (a) Two-dimensional radial SANS patterns for a lamellar system at different shear rates, (b) intensity versus azimuthal angle, Φ , of rheo-SANS data at different shear rates, and (c) intensity versus scattering vector, q , at different shear rates.

Figure G-10 shows the relaxation behavior of samples after stopping the shear-alignment step. Moduli of the samples increase to their initial value with time during the relaxation process. In other words, the shear-alignment is a reversible process and if the sample has enough time at rest, it relaxes back to its original state with nearly the same viscoelastic behavior. The relaxation of moduli to their initial values suggests that at rest, defects spontaneously form; thus, the LLC systems move again toward an unaligned state. [100].

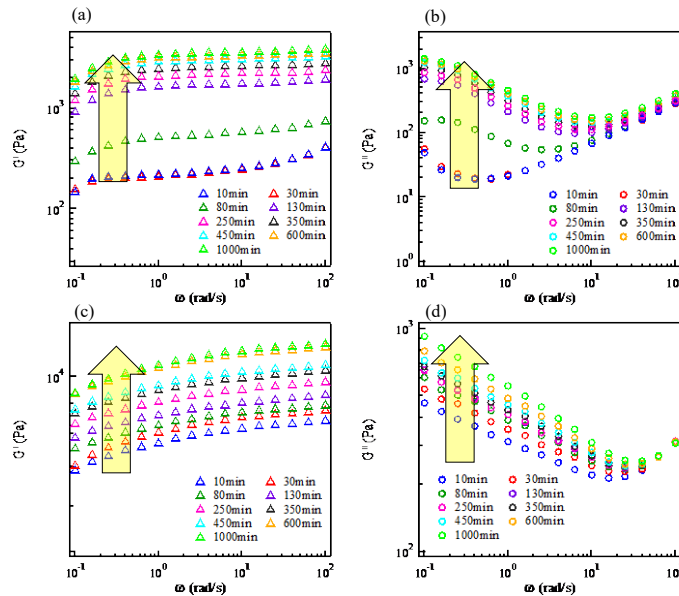


Figure G-10. Evolution of elastic modulus and loss modulus at different times during relaxation for (a) and (b) P123_60/35/5_Lam and (c) and (d) L121_60/25/15_Hex samples. The arrow direction shows the increase in time in all graphs.

Appendix H: Experimental Methodology and Results for Chapter 4 Data

H.1 Experimental Procedures

H.1.1 Materials

Pluronic block copolymers, P84, L121, and L64 are used as surfactants. Butyl acrylate and ethylene glycol dimethacrylate are used as monomer and crosslinker, respectively. Azobisisobutyronitrile is used as the thermal initiator. DI water is used as the aqueous phase. The monomer and crosslinker are purified by passing through a silica column.

H.1.2 Formulation design

The method of mesophase preparation has been explained before [42]. Simply stated, desired amounts of components are mixed using centrifugation at alternative directions until a transparent mesophase is obtained. Table H-1 shows the ratio of materials used in each sample. The monomer to crosslinker weight ratio is held constant at 3:1 and the initiator concentration is 3 wt% of the monomer in all samples. Samples are formulated in a way that the monomer plus crosslinker concentration is constant, but changing water/block copolymer ratios makes different mesostructures. It should be noted that it is almost impossible to have different mesostructures with the same Pluronic at a fixed oil phase (monomer) concentration. Thus, SAXS measurements are used to confirm the mesostructure of each sample before and after polymerization as explained in the Chapter 2.

H.1.3 Rheological measurements

The Discovery Hybrid Rheometer DHR-3 rheometer is used to study the rheological behavior and chemorheology of mesophases. A 40 mm sand-blasted parallel plate geometry with 1 mm gap is used in all experiments. All tests are performed in the linear viscoelastic region (0.5% strain, confirmed from amplitude sweep tests). First, dynamic frequency sweep tests are performed at 25 °C in the frequency range of 0.1 to 600 rad/s. For chemorheology studies, a solvent trap filled with DI water is used. Time tests in small amplitude oscillatory shear mode are done on mesophases at three different temperatures, namely 60, 65, and 70°C to determine the kinetics of polymerization through the evolution of storage and loss moduli [127]. Data are collected in the linear viscoelastic region (strain amplitude of 0.5%) at a constant frequency of 1 Hz. Polymerization of the pure monomer phase is also studied as the control sample to define the kinetics of polymerization in the non-confined state.

H.1.4 DSC measurements

Isothermal DSC is carried out utilizing Q2000 (TA Instruments, New Castle, DE). Approximately 10 mg of mesophase is placed in the aluminum pans and the heat of reaction is recorded with time. All measurements are performed under a nitrogen gas atmosphere at elevated temperatures (60, 65, and 70 °C) to determine the rate of polymerization according to the procedure established by Guymon and coworkers [117, 118, 206, 207]. Having the heat flow, ΔQ , the polymerization rate, R_p , can be calculated as:

$$\frac{R_p}{[M]_0} = \Delta Q \left[\left(\frac{M_w}{n_m \Delta H_p m} \right)_{monomer} + \left(\frac{M_w}{n_m \Delta H_p m} \right)_{crosslinker} \right] \quad (H-1)$$

where M_w , $[M]_0$, ΔH , n , and m are molecular weight, initial concentration, theoretical reaction enthalpy (86,200 J/mol for acrylate and 56,000 J/mol for methacrylate) [37], functionality, and mass, respectively [129]. Polymerization of the pure oil phase is also studied as a control sample to define the kinetics of polymerization in the non-confined state. The polymerization rate is normalized to the total reactive species' concentration in the formulation. The reaction temperature is maintained constant (within ± 0.1 °C) during the measurements. The degree of monomer conversion is calculated by integrating the area between the DSC curves and the baseline established by extrapolation from the trace produced after complete polymerization.

H.1.5 Monomer conversion

The final conversion is experimentally obtained by washing the mesophases with a soxhlet extractor to remove residual monomer, initiator, and crosslinker. There is also a possibility of block copolymer removal during washing. Samples are first washed with water for 12 hr, and then with methanol for another 24 hr. Thermal gravimetric analysis (TGA) is done on the washing solvents after soxhlet extraction to confirm that Pluronic block copolymer has not been washed out, as shown in Figure H-1. After washing, the samples are dried in the vacuum oven at 40 °C for 48 hr. Dried samples are weighed and the conversion is obtained using gravimetric analysis.

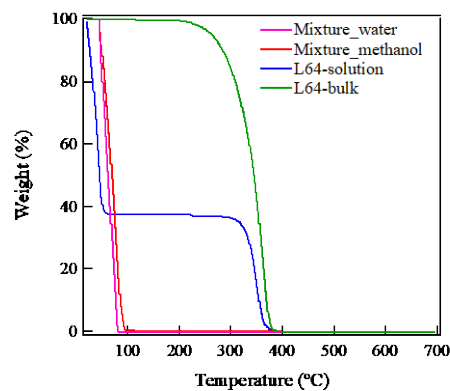


Figure H-1. Typical TGA data for soxhlet mixtures after washing with water and methanol. TGA data of Pluornic L64 block copolymer in the bulk state and its solution in water is also provided.

H.2 Results

H.2.1 SAXS

SAXS results before and after polymerization are shown in Figure H-2. Polymerized samples at elevated temperatures show the same pattern in the peak positions, while there is a slight shift of peaks to the left. The calculated parameters obtained from SAXS experiments on various samples are summarized in Table H-1. Apolar domain size and its change after polymerization are two important factors in the kinetics of polymerization and will be discussed later.

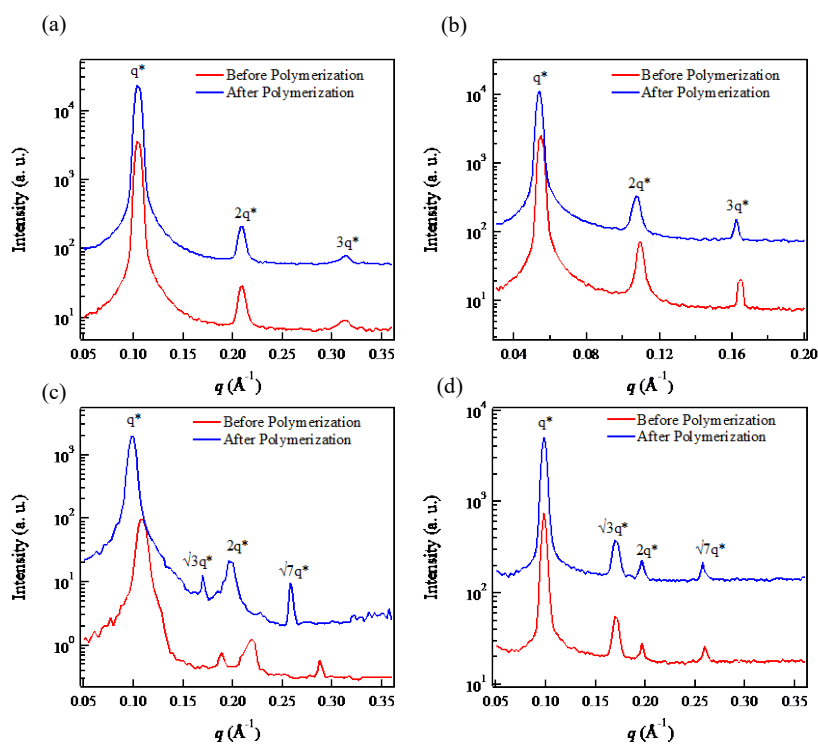


Figure H-2. 1D SAXS graphs of mesophase systems with Pluronic block copolymer/water/oil (wt%) composition before and after polymerization: (a) P84- L_{α} (60/15/25), (b) L121- L_{α} (57/18/25), (c) P84- H_2 (40/35/25), and (d) L64- H_2 (55/20/25). Oil phase consists of butyl acrylate, EGDMA, and AIBN.

Table H-1. Composition of the samples and their calculated SAXS parameters.

Sample	Composition (Pluronic/water/monomer) (wt%)	ϕ	d or a , unpolymerized (nm)	δ or α , unpolymerized (nm)	Intermicellar distance (nm)
P84- L_{α}	(60/15/25)	0.62	6.0	3.7	0.9
L121- L_{α}	(57/18/25)	0.31	10.0	3.1	1.6
P84- H_2	(40/35/25)	0.50	6.6	2.4	0.6
L64- H_2	(55/20/25)	0.60	7.4	3.0	0.8

The polymerized samples show a slight shift in the peaks to smaller scattering vectors, which indicates an increase in the lattice parameter, thus, in the apolar domain size. The change in domain size is attributed to the competition between thermodynamics and kinetics. By progression of polymerization, the molecular weight and degree of polymerization, N , increase;

thus, the enthalpic penalty, χN , outweighs the entropic contribution to the Gibbs free energy. Therefore, the system is driven toward the increase in domain size (and ultimately phase separation). On the other hand, the density of the monomer phase increases upon polymerization ($\Delta\rho\sim 10\%$), which leads to the shrinkage and decrease in the domain size. The presence of Pluronic block copolymers with slow dynamics decreases the rate of phase separation. In addition, crosslinking arrests and preserves the structure during thermal polymerization. Critical molecular weight entanglement (M_c) for PEO and PPO are 10,000 g/mol and 7000 g/mol, respectively [208, 209]. All the Pluronic block copolymers in our study have molecular weight well below M_c . Therefore, block copolymers are not entangled in the system. Additionally, the radius of gyration of Pluronic P84, Pluronic L121, and Pluronic L64 block copolymers are approximately 17 Å [43], 17.8 Å [210], and 19 Å [211], respectively, which are smaller than the domain size of the micelles. Thus, there is no chain crossing the oil phase from one hydrophilic domain to another one.

H.2.2 Rheological measurements

Frequency sweep results for lamellar and reverse hexagonal mesophases in Figure H-3 show that all mesophases have solid-like behavior, where the storage modulus is higher than the loss modulus in the whole range of studied frequencies [81]. Such behavior has been observed for suspensions, block copolymer solutions, and highly concentrated emulsions [212–214]. In the systems under study, the solid-like behavior is due to the high concentration of block copolymer and the compact LLC structures. It has been shown that lamellar structures have one order of magnitude lower storage moduli when compared with hexagonal mesophases [84, 85]. As it is evident from Figure H-3, the storage modulus in (c) and (d) plots (H_2 samples) is higher than that of (a) and (b) ones (L_α samples). Comparing the lamellar samples, P84- L_α (60/15/25) shows higher storage modulus compared to L121- L_α (57/18/25), which is due to the smaller domain size and intermicellar distance in P84- L_α samples. According to the study model developed recently on the basis of van der Waals interactions (which is the main source of intermicellar interactions) [102, 103], the storage modulus is highly dependent on the reciprocal of intermicellar distance. The intermicellar distances in lamellar and reverse hexagonal systems are calculated (see Chapter 2) and summarized in Table H-1. Average intermicellar distance in the P84- L_α sample is smaller than that of the L121- L_α sample and consequently the storage modulus is higher in the P84- L_α sample. Additionally, the intermicellar distance in the P84- H_2 sample is smaller than that of the L64- H_2 sample. Thus, the elastic modulus is higher in the P84- H_2 sample [102, 103].

A shallow minimum is observed in the loss modulus curves of all samples that is characteristic of polymeric gels and has been observed for emulsions and soft-glassy materials as well [194, 197, 199–201]. As discussed in Chapter 3 and Appendix G, the minimum in the loss modulus shows

the presence of two relaxation behaviors in the system and the transition from α -relaxation observed in low frequencies (related to large domain sizes, i.e., grain scale) to β -relaxation observed in high frequencies (related to small domain sizes, i.e., micelle scale).

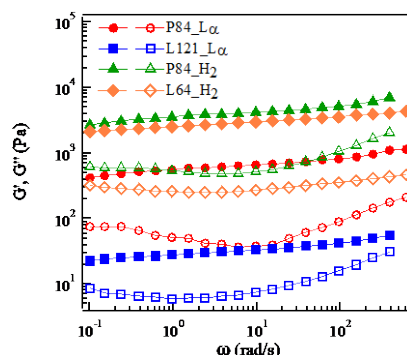


Figure H-3. Frequency sweep curves of mesophase systems with different Pluronic block copolymer/water/oil (wt%) compositions: P84- L_α (60/15/25), L121- L_α (57/18/25), P84- H_2 (40/35/25), and L64- H_2 (55/20/25).

H.2.2.1 Induction activation energy

Having t_{in} at different temperatures, we can calculate the activation energy from the slope of $\ln t_{in}$ versus $\frac{1}{RT}$ graph (Figure H-4). The values are reported in Table 4-1. The activation energies for confined samples are higher than those of the bulk sample, which is due to the higher viscosity of confined mesophases that controls the diffusion-controlled initiation in the systems. The lamellar samples show slightly lower initiation activation energy compared to the reverse hexagonal ones because of their lower viscosity as confirmed from rheology.

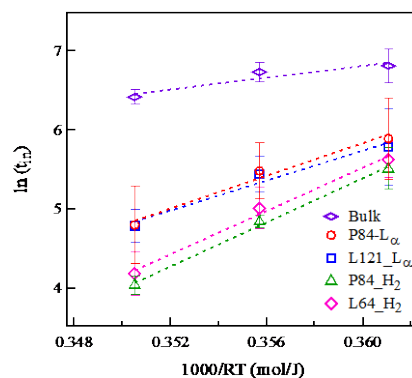


Figure H-4. The effect of temperature on the initiation time of the polymerization in bulk sample and mesophases of P84- L_α , L121- L_α , P84- H_2 , and L64- H_2 samples. The slopes of the lines are used to estimate the initiation activation energy.

H.2.3 DSC measurements

To confirm the kinetic parameters obtained from chemorheological studies, DSC is performed on two typical samples with lamellar and hexagonal structures (P84- L_α and P84- H_2). The polymerization rate versus time (Figure H-5) and conversion versus time plots (Figure H-6) confirm that the radical polymerization in mesophases is influenced by diffusion-controlled phenomena.

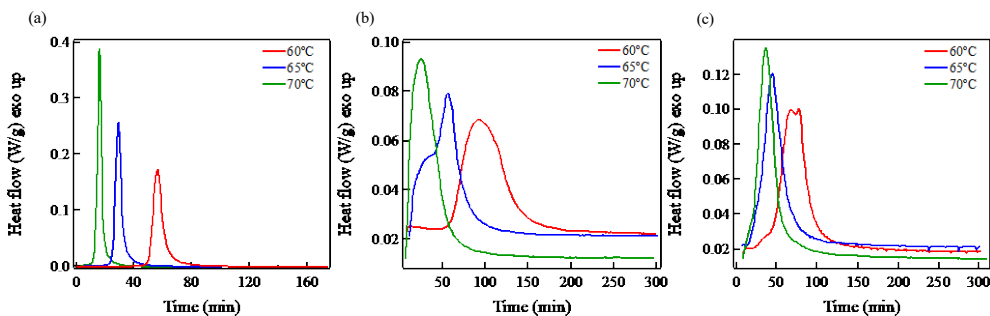


Figure H-5. The effect of temperature on the variation of heat flow with time during isothermal polymerization of (a) bulk, (b) P84- L_α , and (c) P84- H_2 .

In the first stage of polymerization (low conversions), an almost linear dependence of conversion, and an approximately constant R_p appears, indicating the purely chemical-controlled nature of the polymerization [215]. In the region of 10-20 % conversion, a sharp increase in the reaction rate (autoacceleration) takes place, followed by an increase in the conversion values

[216, 217]. The autoacceleration (gel effect) is attributed to the effect of diffusion-controlled phenomena on the termination reaction.

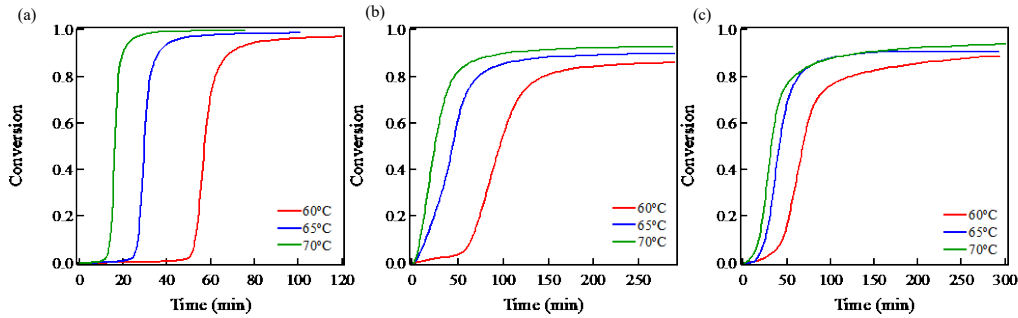


Figure H-6. The effect of temperature on the variation of conversion with time during isothermal polymerization of (a) bulk, (b) P84-L α , and (c) P84-H $_2$.

As discussed in Chapter 1, by considering the steady-state hypothesis for free radical polymerization, the polymerization rate, R_p , is given as a function of conversion, X [217]:

$$\frac{R_p}{[M]} \cong K' (1 - X) \quad (\text{H-2.a})$$

$$K' = k_p \left(\frac{f_i k_d}{k_t} \right)^{1/2} [I]^{1/2} \quad (\text{H-2.b})$$

where k_d represents the kinetic rate constant of initiator decomposition and f is the initiator efficiency. The propagation and termination rate constants are k_p and k_t , respectively.

To investigate the effect of temperature on the reaction kinetics, Equation (H-2.a) can be integrated assuming that all the kinetic rate coefficients, initiator concentration, and efficiency are constant. Therefore, an expression that directly correlates the monomer conversion with an observed overall kinetic rate coefficient, K' , can be obtained:

$$-\ln(1 - X) = K' t \quad (\text{H-3})$$

It should be noted that the described assumptions are valid only for low degrees of monomer conversion [217]. The slope of the initial linear part (between 2 to 10 % where autoacceleration is negligible) of the plot of $-\ln(1 - X)$ versus t , gives the overall kinetic rate constant [217, 218]. Thus, the overall kinetic rate values are measured at different temperatures for the bulk state and for two typical samples with lamellar and hexagonal structures. The overall activation energy of polymerization is obtained by considering an Arrhenius-type dependency of reaction rate on temperature.

As shown in Figure H-6, the maximum conversion obtained upon polymerization increases with increasing reaction temperature in both the bulk and nanoconfined systems, which can be attributed to increased polymerization rate and monomer diffusion coefficients [127]. In addition, a lower limiting conversion is reached for the mesophases with lamellar structure compared to the reverse hexagonal one. This is in agreement with the chemorheology results.

Table H-2 shows the kinetic parameters derived from DSC. It is shown that the polymerization rate in nanoconfined structures is significantly (one order of magnitude) lower than that of the bulk polymerization, which is in agreement with chemorheology results. As mentioned earlier, the DSC results (Figure H-5 and H-6) show that the radical polymerization in mesophases is controlled by diffusion-controlled phenomena. The activation energies obtained from the chemorheology (Table 4-1) and DSC (Table H-2) experiments show that the reverse hexagonal mesophases have higher activation energy compared to the bulk and lamellar mesophases. This is attributed to the higher viscosity of the reverse hexagonal systems compared to the lamellar ones at the early stages of polymerization. On the other hand, it is observed that by increasing the degree of confinement in the system, the gel effect is decreased during the polymerization. It is confirmed that the lamellar mesophase with the highest degree of confinement has the lowest conversion and polymerization rate, which are induced by the increase in the termination rate.

These results show that the confinement effect is competing with the gel effect when the polymerization is proceeding within the mesophase system. The high degree of confinement increases the probability of two radicals to react with each other, and consequently increases the termination rate.

Table H-2. Activation energy and kinetic rate constants of polymerization for bulk and confined structures at different temperatures derived from DSC measurements.

Sample	E	K' (60 °C)	K' (65 °C)	K' (70 °C)
Unit	kJ/mol	$10^{-3}/s$	$10^{-3}/s$	$10^{-3}/s$
P84- H ₂	84	3.6	8.5	9.1
P84- L _α	75	3.4	7.6	8.2
Bulk	52	21.4	25.3	37.3

Appendix I: Experimental Methodology and Results for Chapter 5 Data

I.1 Experimental Methodology

I.1.1 Membrane fabrication

Following removal of the poly(ether sulfone) NIPS membrane, recovered supports are dried under high vacuum for at least 24 hours and found to have an average thickness of 190 μm . A small amount of the unpolymerized mesophase (~ 2 mL) is subsequently placed onto the support such that the mesophase comprised roughly 60 wt. % of the final membrane. The gel mixture on the support is then sandwiched between Mylar sheets and smooth stainless-steel plates. The entire assembly is subsequently pressed using a hot press pre-heated to 40 $^{\circ}\text{C}$ with a force of 105 N for five minutes, allowing the monomer mixture to completely infuse the support film. Following, the film is placed in a UV chamber (Spectroline Corporation, Select XLE-Series) for two hours where it undergoes UV polymerization, after which it is transferred to a drying oven at 70 $^{\circ}\text{C}$ for three hours to ensure the polymerization is complete (Figure I-1). It should be noted that the support material could easily be replaced with more renewable alternatives and is not believed to have a significant effect on the membrane nanostructure as evidenced by SAXS results from polymerized mesophases with and without the support, shown in Figure I-2. It can be seen that the presence of the support does not have any effect on the structure of the mesophase upon polymerization.

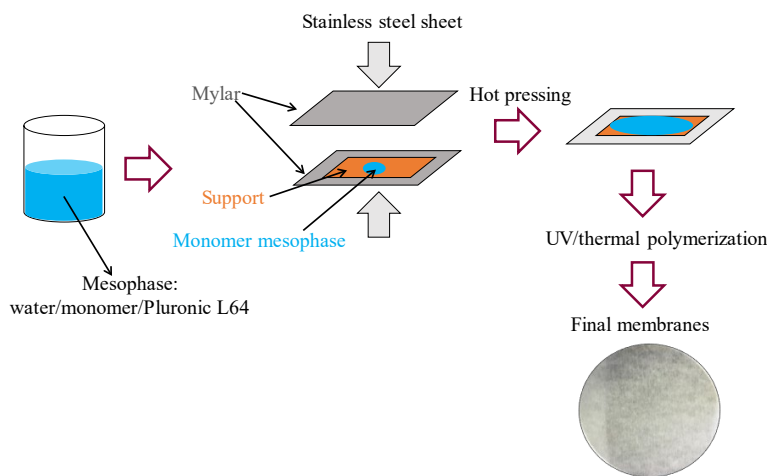


Figure I-1. Schematic illustration of the necessary steps for making UF membranes.

I.2 Results

I.2.1 SAXS data

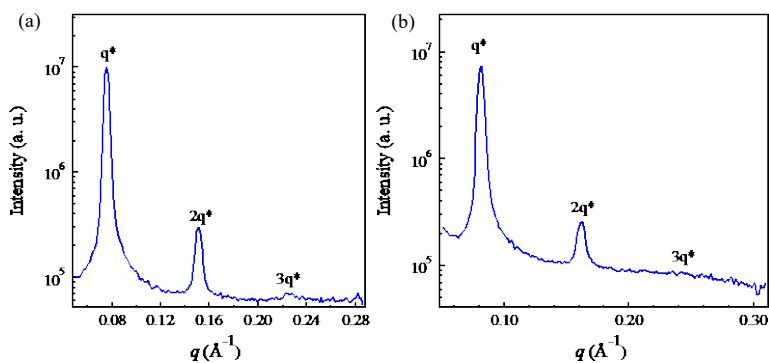


Figure I-2. SAXS graphs of mesophase systems containing monomer (Pluronic L64/water/(butyl acrylate+EGDMA+HCPK+AIBN)), sample I, after polymerization, (a) with and (b) without support.

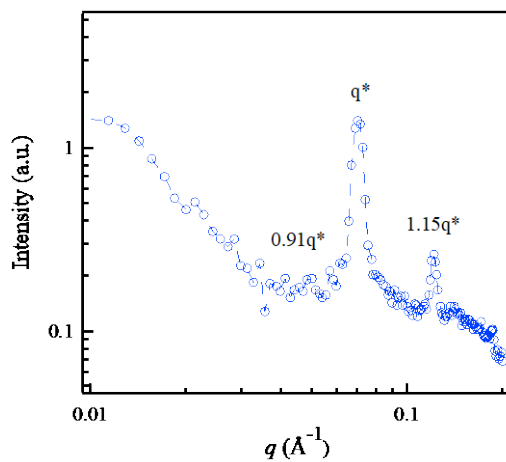


Figure I-3. Log-log scale 1D SAXS graphs of mesophase system containing monomer (Pluronic L64/water/(butyl acrylate+EGDMA+HCPK+AIBN)) with 60/15/25 composition before polymerization. Pre- and post-shoulders in primary peak at $0.91q^*$ and $1.15q^*$ are indicative of HM/HPL structures.

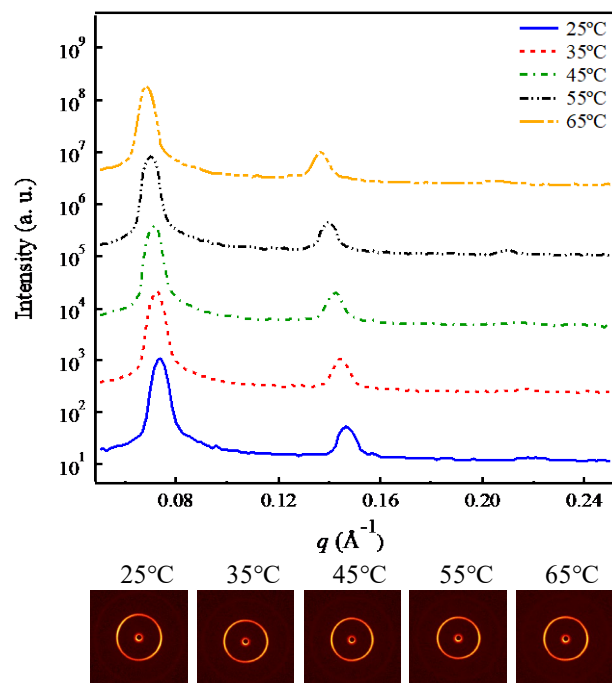


Figure I-4. 1D and 2D SAXS patterns as a function of temperature for sample A with composition of (Pluronic L64/water/(butyl acrylate+EGDMA+HCPK+AIBN) (60/30/10).

I.2.2 Membrane performance

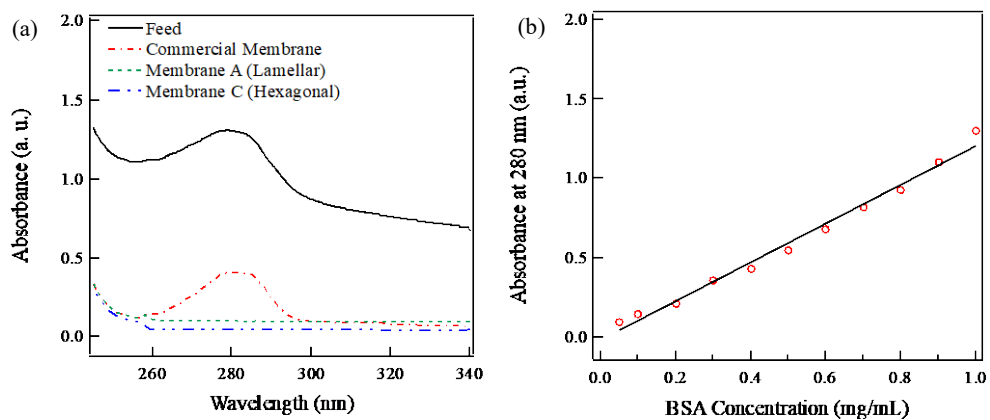


Figure I-5. (a) UV-Vis spectra of feed solution, permeate of membrane I (lamellar), and permeate of membrane III (hexagonal); (b) UV-Vis calibration curve of BSA.

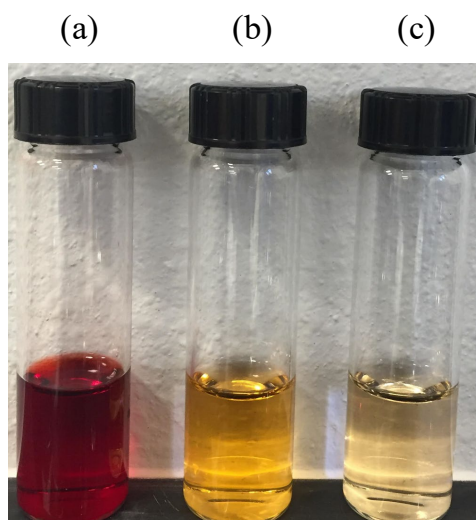


Figure I-6. Digital photographs of (a) 1 g/L of DR23 feed solution, (b) permeate of commercial membrane, and (c) permeate of lamellar membrane.

I.2.3 Antibacterial membranes SAXS results

SAXS data presented in Figures I-7 and I-8 show that samples HD1 and HD3 are lamellar and that their structure remains intact upon polymerization.

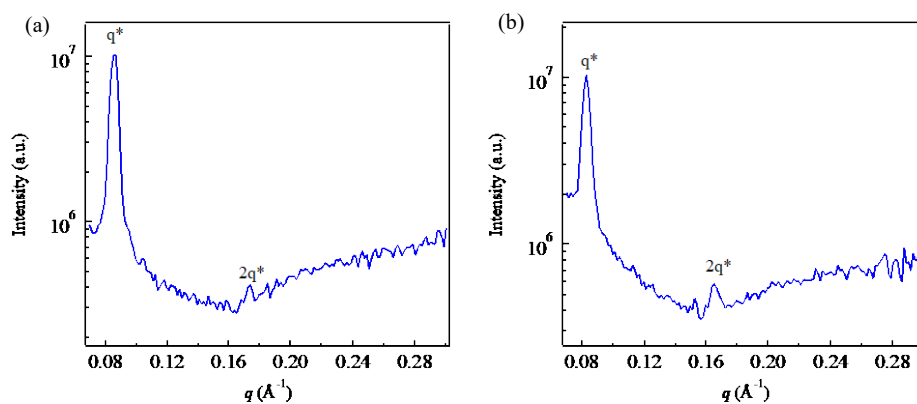


Figure I-7. 1D SAXS data for sample HD1 (a) before and (b) after polymerization.

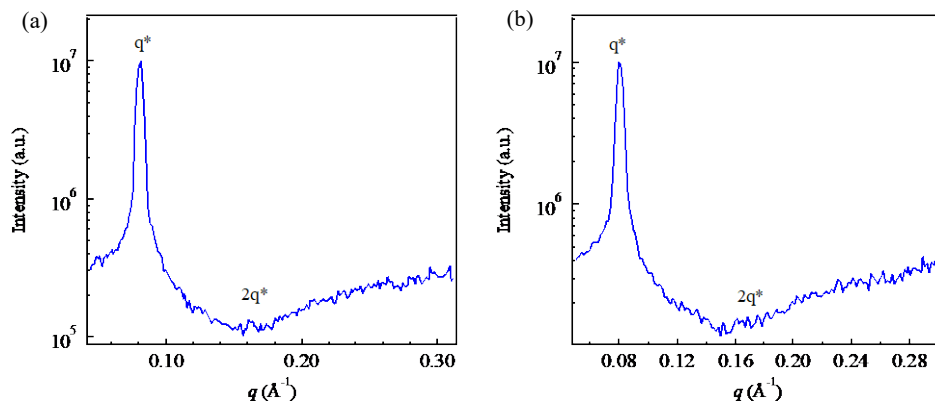


Figure I-8. 1D SAXS data for sample HD3 (a) before and (b) after polymerization.

As shown in Figure I-9, sample HD4 has a hexagonal structure. Results show that sample HD6 did not have any structure.

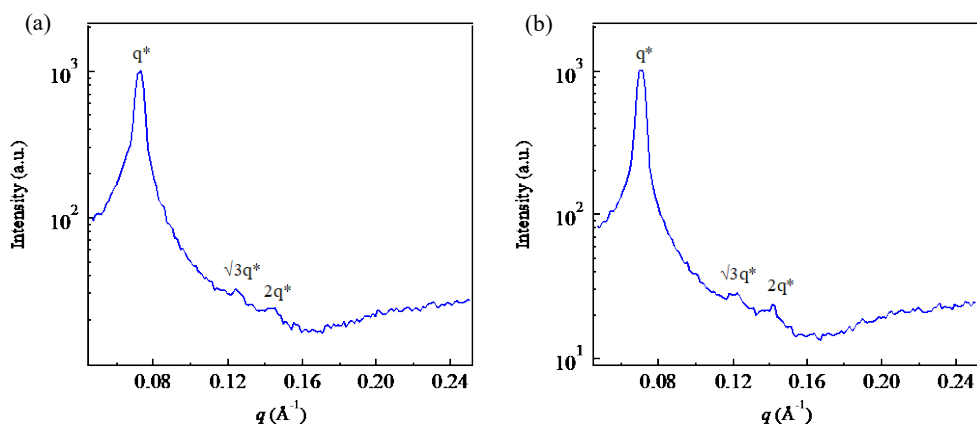


Figure I-9. 1D SAXS data for sample HD4 (a) before and (b) after polymerization.

I.2.4 Antibacterial membrane performance measurements

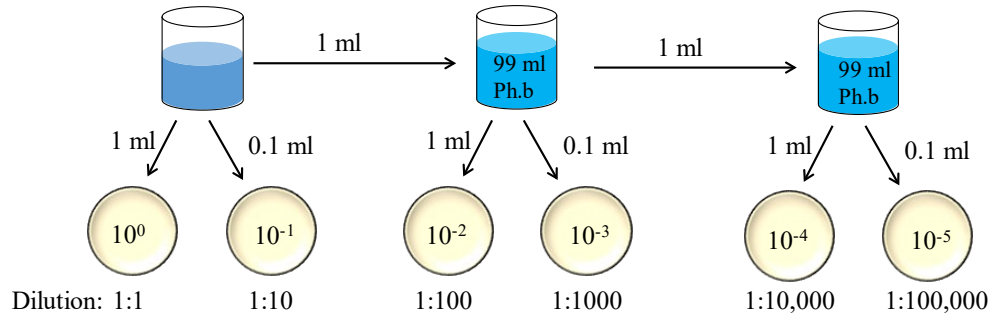


Figure I-10. Dilution steps used for making Petrifilm samples.

Appendix J: Future Work

J.1 Studying the flow-induced behavior of mesophases using rheo-SANS

Our preliminary study on a lamellar sample of a Pluronic P84/water/p-xylene system showed that mesophases align themselves in the direction of flow in a simple shear flow field (refer to Chapter 3). This finding can be utilized for making ordered structures using shear deformations. However, further investigations are required to analyze more samples with different types of structures using different flow fields such as simple shear, small and large amplitude oscillation to reveal how the mesostructure influences the alignment/formation of single crystals upon shear and/or oscillation deformation.

J.2 Studying the shear banding behavior of mesophases using the velocimetry technique

When a fluid is sheared, the strain rate can have large values in narrow areas of the sample. Therefore, shear banding may occur, which is due to a sharp instability (inhomogeneity) in the deformation rate. Shear banding has been reported in several complex fluids such as soft glassy materials [188], polymer solutions and melts [219, 220], worm-like micelles [221], and LLCs [187, 222]. Usually, a stress plateau is observed in the flow curve of the systems because of shear banding. However, to confirm the presence of shear banding and in order to analyze the number of bands and the reasons for shear banding occurrence, direct observation techniques are required. Particle image velocimetry (PIV) and particle tracking velocimetry (PTC) are common methods for evaluating shear bands in complex fluids. Studying the possible shear banding behavior of mesophases provides useful fundamental and practical information.

J.3 RAFT polymerization in nanoconfined mesophases

RAFT is a type of living polymerization that involves a conventional radical polymerization mediated by a RAFT agent. RAFT enables us to synthesize block copolymers with controlled block ratios and molecular weight. RAFT polymerization provides control over molecular weight and polydispersity of the final polymer. Incorporating RAFT polymerization in nanoconfined mesophases provides a platform to make block copolymers with a mesoporous structure.